STATISTICAL ANALYSIS OF THE COSMIC MICROWAVE BACKGROUND

by

Yajing Huang

A dissertation submitted to The Johns Hopkins University

in conformity with the requirements for the degree of

Doctor of Philosophy

Baltimore, Maryland

August, 2020

Abstract

The standard ΛCDM model has successfully described the content and the evolution of the universe with predictions in impressive agreement with observations of the Cosmic Microwave Background (CMB). Yet recently major tension has emerged between results from observations of early and late cosmological time. My research focuses on applying statistical tools to analyze and quantify consistency between different data sets as well as different extension models to ΛCDM. This thesis begins with an overview of the ΛCDM model and the physics of the CMB. In the following chapters, I will present my work on examining the internal consistency of the *Planck* 2015 CMB temperature anisotropy power spectrum. Then I will detail the procedure and results from quantitative comparison between *WMAP* 9-year and *Planck* 2015 temperature power spectra over their common multipole range. I will also highlight the importance of examining the correlations between additional parameters when investigating extensions to the standard ΛCDM model and describe how these correlations can be quantified with simulations and Monte Carlo Markov Chain methods.

Primary Reader: Charles Bennett

Secondary Reader: Tobias Marriage

Acknowledgments

I would like to thank my advisor, Prof. Charles Bennett, for his guidance, support and patience through my Ph.D. years. I am also grateful to Graeme Addison, whom I have learnt from and whose many discussions helped bring my research projects to life. I would also like to thank everyone in my dissertation committee for their expertise, time and feedback. Lastly I would like to thank my husband, friends and members of the Johns Hopkins community.

Table of Contents

List of Tables

List of Figures

Chapter 1

Introduction

Over the last two decades, substantial progress has been made on refining our understanding of the universe to unprecedented precision. The standard ΛCDM model has successfully described the content and the evolution of the universe with predictions in impressive agreement with observations, e.g. of the Cosmic Microwave Background (CMB) (Hinshaw et al., 2013; Planck Collaboration, 2016; Planck Collaboration, 2018; Sievers et al., 2013; Story et al., 2013), Baryon Acoustic Oscillation (BAO) (Eisenstein et al., 2005; Anderson et al., 2012), and weak gravitational lensing (Erben et al., 2013; Hildebrandt et al., 2017; Abbott et al., 2018). Yet increasingly precise measurements have also revealed major tension between results from observations of early and late cosmological time. The most notable one is the $\sim 5\sigma$ disagreement between the Hubble constant measurements from direct distance ladder measurements (Riess, 2019) and from the Planck CMB data (Planck Collaboration, 2018). The measurement of H_0 via strong lensing time delays (Wong et al., 2020) is consistent with the SH0ES measurement (Riess et al., 2019) and in 5.3σ tension with Planck. Addison et al., 2018 showed that the tension between early and

late time universe measurements persists even without the inclusion of Planck data, with BAO scale measurements.

Various avenues to reconcile this tension have been explored. Systematic effects in measurements have been investigated, yet no obvious explanation for the tension has been found (Efstathiou, 2014; Planck Collaboration, 2017; Aylor et al., 2019). On the theory side, extensions or alternatives to the ΛCDM model have been proposed to change our understanding of the physics of the expansion history. For example, the effects of varying the effective number of neutrino species (e.g., Riess et al., 2016) and the equation of state parameter of dark energy (e.g., Joudaki et al., 2017) have been studied, though these extensions have not been able to effectively relieve the tension without including multiple turning points in the evolution of the dark energy equation of state (Zhao et al., 2017). Early dark energy models have been suggested as a possible solution (Poulin et al., 2019; Smith, Poulin, and Amin, 2020), yet they do not provide a good fit to large-scale structure data (Hill et al., 2020; Ivanov et al., 2020). In short, we have not yet seen a convincing explanation for the departure from the standard ΛCDM as a solution to the Hubble tension.

However, before embarking on any of these avenues, one needs to first understand how significant results from different cosmological probes agree or disagree. With this in mind, my research has focused on applying statistical tools to quantitatively study consistency both between different data sets and internally within a data set. Moreover, to aid hypothesis testing for alternative theories, I developed a method to quantify correlations between additional parameters in ΛCDM extensions that are not fitted simultaneously.

The outline of this thesis is as follows. In the rest of this chapter, I will lay down the theoretical foundation of my research. Specifically I will give an overview of the ΛCDM model and the physics of the CMB, followed by an introduction to the computational tools I used in my work. In the following chapters, I will present my work on quantifying consistency between results from different observation and from different models. In chapter 2, I reproduce Addison et al., 2016, which examines the internal consistency of the Planck 2015 CMB temperature anisotropy power spectrum. Chapter 3 is taken from Huang et al., 2018. It details the procedure and results from quantitative comparison between WMAP 9-year and Planck 2015 temperature power spectra over their common multipole range. I find that their spectra are consistent within 1σ. In Chapter 4 I describe my work in Huang, Addison, and Bennett, 2019, which highlights the importance of examining the correlations between additional parameters when investigating extensions to the standard ΛCDM model and describes how these correlations can be quantified with simulations and Monte Carlo Markov Chain methods.

1.1 The ΛCDM Universe

Our universe can be well described by ΛCDM, the standard model of cosmology, which accounts for the presence of cold dark matter (CDM) and dark energy (associated with the cosmological constant Λ) as well as radiation and baryonic matter.

The ΛCDM model is based on the framework of general relativity and the observation that the universe is largely isotropic and homogeneous. Assuming

perfect homogeneity and isotropy, the Friedmann-Lemaître-Robertson-Walker (FLRW) metric, which incorporates gravity into a curved space-time and the expansion of the universe into the time-dependent scale factor $a(t)$, is written as

$$\mathrm{d}s^2 = g_{\mu\nu} dx^\mu dx^\nu = -dt^2 + a(t)^2 d\Sigma^2 \tag{1.1}$$

in units with the speed of light $c = 1$. Here Σ denotes a 3-dimensional space that is either elliptic, Euclidean or hyperbolic. In the simplest ΛCDM model, where space is approximately flat, the FLRW metric can be written as

$$\mathrm{d}s^2 = g_{\mu\nu} dx^\mu dx^\nu = -dt^2 + a(t)^2 \delta_{ij} dx^i dx^j \tag{1.2}$$

with x being the co-moving coordinates. For simplicity, we can also define the conformal FLRW-metric as

$$\mathrm{d}s^2 = a(\tau)^2(-d\tau^2 + \delta_{ij} dx^i dx^j) \text{ or } g_{\mu\nu} = a^2 \eta_{\mu\nu}, \tag{1.3}$$

where the conformal time $d\tau$ is defined as

$$d\tau = \frac{dt}{a(t)}. \tag{1.4}$$

In the ΛCDM framework, the relationship between the space-time geometry and the energy of the matter in the universe is described by the Einstein field equation with the cosmological constant Λ:

$$R_{\mu\nu} - \frac{1}{2} g_{\mu\nu} R = 8\pi G T_{\mu\nu} + \Lambda g_{\mu\nu}. \tag{1.5}$$

Here $R_{\mu\nu}$ and R are the Ricci tensor and scalar respectively. They are determined by the metric $g_{\mu\nu}$.

Λ, the cosmological constant, first proposed by Einstein in 1917 to make the universe static and later abandoned, is invoked to account for the observed acceleration of the expansion of the universe. It is the simplest realization of dark energy, which is a strange form of energy that is gravitationally repulsive.

In 1.5, $T_{\mu\nu}$ is the energy-momentum tensor. Assuming the matter in the universe as an isotropic perfect fluid in the co-moving coordinates, it is given by

$$T_{\mu\nu} = \begin{pmatrix} -\rho & 0 & 0 & 0 \\ 0 & \mathcal{P} & 0 & 0 \\ 0 & 0 & \mathcal{P} & 0 \\ 0 & 0 & 0 & \mathcal{P} \end{pmatrix} \tag{1.6}$$

where ρ is the energy density and $\mathcal{P}$ is the pressure of the fluid.

Inserting the metric and the energy-momentum tensor into the Einstein equation results in the Friedmann equations:

$$\left(\frac{\dot{a}}{a}\right)^2 = \frac{8\pi G\rho + \Lambda}{3} \tag{1.7}$$

and

$$\frac{\ddot{a}}{a} = -\frac{4\pi G}{3}(\rho + 3\mathcal{P}) + \frac{\Lambda}{3}. \tag{1.8}$$

The Hubble parameter is defined as $H \equiv \frac{\dot{a}}{a}$, describing the expansion rate of the universe.

In addition, the energy conservation law for the perfect fluid leads to

$$\dot{\rho} = -3H(\rho + \mathcal{P}). \tag{1.9}$$

To solve 1.9 for a specific type of fluid, the relation between its energy density and its pressure is written in a simple linear form:

$$\mathcal{P} = \omega\rho \tag{1.10}$$

where ω is the equation of state parameter. With 1.10, the fluid equation 1.9 implies how the energy density evolves in an expanding universe:

$$\frac{\rho}{\rho_0} = \left(\frac{a}{a_0}\right)^{-3(1+\omega)} \tag{1.11}$$

where the subscript 0 denotes values at present time.

For important cosmological mass-energy, ω is constant in time. For radiation (photons and neutrinos), $\omega = 1/3$. For non-relativistic matter, $\omega = 0$. The non-relativistic matter sector consists of baryons, which are massive elementary particles made up of three quarks, and cold dark matter, which does not interact with the electromagnetic force. The only interactions of cold dark matter with others are gravitational. Baryonic matter account for roughly 5% of the total density in the universe today, while dark matter around 26%. The remaining 70% of the universe is dark energy, acting as a cosmological constant Λ with $\omega = -1$, corresponding to a negative pressure. It is responsible for the accelerated expansion of the universe.

1.2 Inflation

Though the ΛCDM model fits our observations of the universe very well, it does not explain why the universe is so homogeneous and isotropic, that

even regions which could not have been in causal contact share almost the same temperature. Nor does it explain why the universe is remarkably flat (Hinshaw et al., 2013; Planck Collaboration, 2016; Planck Collaboration, 2018), without some extreme fine-tuning of early conditions.

The Inflation theory provides solutions to all these problems with an exponential expansion of space that occurred 10^{-36}s after the Big Bang (Guth, 1981; Linde, 1982; Albrecht and Steinhardt, 1982). With the scale factor $a(t)$ increased by greater than e^{60} within approximately 10^{-32}s, the distance between particles that were once in causal contact expanded to be greater than the horizon and the particles became causally disconnected. With the accelerating expansion of space, initial inhomogeneities and anisotropies were smoothed out, and spatial curvature was driven to near zero.

Inflation also expands microscopic quantum fluctuations in the early universe to cosmological scale, giving rise to structure formation in the universe. Perturbations produced by quantum fluctuations result in modification of the metric:

$$g_{\mu\nu} = \bar{g_{\mu\nu}} + \delta g_{\mu\nu} = a^2(\eta_{\mu\nu} + 2\zeta\eta_{\mu\nu} + h_{\mu\nu}), \tag{1.12}$$

where ζ describes scalar density perturbations and $h_{\mu\nu}$ describes tensor perturbations.

The power spectrum P_s of the scalar perturbations can be parametrized by a power law with amplitude A_s, spectral index n_s and an arbitrary wavenumber k_*:

$$P_s(k) = A_s(k_*)\left(\frac{k}{k_*}\right)^{n_s-1}. \tag{1.13}$$

An analogous expression applies for the tensor perturbations.

Both *WMAP* and *Planck* data support the theory of inflation, with the observation of a slightly tilted spectrum of initial scalar fluctuations, $n_s = 0.965 \pm 0.004$ (Planck Collaboration, 2018).

1.3 The Cosmic Microwave Background

The CMB is an afterglow of the hot and dense infant universe. The primordial universe was filled with a plasma of protons, electrons, and photons until it cooled due to expansion at around 380,000 years after the Big Bang (corresponding to redshift $z \sim 1100$), allowing neutral hydrogen atoms to form and photons to decouple. As the universe continued to expand and to cool, this radiation was reshifted to longer wavelengths, ending up in the microwave band today.

The CMB is an almost perfectly uniform and isotropic black-body spectrum in space, with a temperature of ~ 2.7 K (Fixsen, 2009) and anisotropies at the level of one part in 10^5. The black-body spectrum is a strong indication of the Big Bang model while slight imperfections provide information such as the matter density fluctuations that seeded structure formation in the universe (Hu, Sugiyama, and Silk, 1997).

Observations of the CMB are our most powerful probe of the physical conditions in the early universe and provide precise and accurate determinations of cosmological models and parameters.

1.3.1 Acoustic Oscillation

Before the universe became neutral at recombination, protons and electrons were tightly coupled to photons, forming a single photon-baryon plasma. The baryons were interacting in a gravitational potential field set up by dark matter. The photon-baryon plasma was not perfectly homogeneous but with density perturbations that were seeded by random quantum fluctuations during inflation. In the plasma, overdense regions became denser under gravity, but the compression was opposed by radiation pressure, which resulted in acoustic oscillations, with sound waves propagating through universe. The distance the sound wave travelled by recombination is referred to as the sound horizon. As the universe expanded, matter diffused and photons redshifted to lower energy and decoupled from the baryons. The phases of the acoustic oscillations were frozen in place at the epoch of recombination, leaving an imprint on the CMB.

1.3.2 Reionization

The universe stayed neutral since recombination until $z \sim 6$, when it became ionized again from UV radiation from newly formed galaxies and quasers (Becker et al., 2001; Fan et al., 2001). Reionization brought about 10% of the CMB photons back in contact with electrons via Thomson scattering, leading to an additional source of optical depth between us and the recombination surface:

$$\tau = \int_0^{z_{reion}} n_e(z)\sigma_T \frac{dt}{dz} dz \tag{1.14}$$

where $n_e(z)$ is the number density of free electrons and σ_T is the Thomson cross-section.

Reionization erased some of the primary anisotropy imprinted on the CMB at recombination on scales within the horizon.

1.3.3 CMB Power Spectrum

A basic observable of the CMB is its intensity as a function of direction on the sky. We can denote the temperature anisotropy at in the direction $\vec{n}$ with $\Delta_T(\mathbf{n})$. Since $\Delta_T(\mathbf{n})$ is defined on the surface of the celestial sphere it is useful to expand it in spherical harmonics:

$$\Delta_T(\mathbf{n}) = \sum_{\ell=0}^{\infty} \sum_{m=-\ell}^{\ell} a_{\ell m} Y_{\ell m}(\mathbf{n}) \tag{1.15}$$

where

$$a_{\ell m} = \int d\Omega_{\mathbf{n}} \Delta_T(\mathbf{n}) Y^*_{\ell m}(\mathbf{n}) \tag{1.16}$$

$$\approx \sum_p \Delta_T(p) \Omega_P Y^*_{\ell m}(p). \tag{1.17}$$

The integral over the sky is approximated by a discrete sum over map pixels p, with each pixel subtending a solid angle Ω_P. The temperature anisotropy we observe now evolves from the initial anisotropy that were produced by quantum-mechanical fluctuations in the early universe during inflation. Since those fluctuations can only be described probabilistically, we cannot predict the exact values of $a_{\ell m}$, but we can study the distribution from which they are drawn. With Δ_T as the temperature perturbation, the $a_{\ell m}$ has zero mean but nonzero variance. We define the variance of $a_{\ell m}$ to be C_ℓ, the temperature

power spectrum by:

$$\langle a_{\ell m} a^*_{\ell' m'} \rangle = \delta_{\ell \ell'} \delta_{m m'} C_\ell. \tag{1.18}$$

We can estimate the power spectrum by

$$C_\ell = \frac{1}{2\ell + 1} \sum_{m=-\ell}^{\ell} |a_{\ell m}|^2. \tag{1.19}$$

In general, C_ℓ corresponds to the temperature fluctuations on the angular scale $\sim 180^\circ/\ell$. When presenting the results of CMB observations, the power spectrum is usually displayed as $\ell(\ell+1)C_\ell/2\pi$, in units of $\mu\mathrm{K}^2$.

The shape of the CMB power spectrum depends on cosmological parameters.

Starting from low multipoles, where the corresponding angular scales are larger than the horizon at recombination, things were only weakly processed by gravity and pressure. So the power spectrum at low ℓ is still the primordial power spectrum from right after inflation, which can be parametrized by a power-law function, with A_s being the amplitude and n_s the spectral index. With n_s very close to one, it is nearly scale invariant.

At $\ell > 200$, the effect of baryon acoustic oscillation is manifest as peaks and troughs in the power spectrum. The $(2n-1)^{\text{th}}$ peaks corresponds to the mode that just underwent n compressions by recombination and the $2n^{\text{th}}$ peaks correspond to n rarefactions by recombination. Because a non-negligible fraction of matter in the universe is in the form of baryons, compressions are stronger than rarefactions. Therefore compression peaks are higher than the rarefaction peaks.

The high multipoles ($\ell \gtrsim 1000$) correspond to very small physical scales

which are smaller than the mean free path of photons, and the initial fluctuations from inflation are washed out by photon diffusion. So the power spectrum decays exponentially with ℓ. The precise damping rate depends on all cosmological parameters. For example, higher baryon density leads to shorter free path for photons which results in less diffusion (Hu and White, 1997), while high dark matter density causes the universe to reach recombination at later times (slower expansion rate), which results in more diffusion. High multipole spectrum provides a consistency check on parameters.

1.4 Cosmological Parameters

The ΛCDM model can be summarized by six base parameters (Hinshaw et al., 2013). They are $\Omega_b h^2$, $\Omega_c h^2$, H_0, τ, n_s and A_s. Other cosmological parameters can be derived from these six.

$\Omega_b h^2$ and $\Omega_c h^2$ are the physical baryon density and the physical cold dark matter density, respectively. H_0 is the current rate of expansion of the universe, usually given in kilometers per second per megaparsec, and h is defined so that $H_0 = 100h$ km sec^{-1} Mpc^{-1}.

In the simplest model, the universe is assumed to be flat, which is consistent with the data (Hinshaw et al., 2013; Planck Collaboration, 2018). To maintain flatness, the dark energy density in units of the critical density Ω_Λ, is determined by the flatness constraint, $\Omega_b + \Omega_c + \Omega_\Lambda = 1$. The physical matter density $\Omega_m h^2$ (sum of $\Omega_b h^2$ and $\Omega_c h^2$) and Ω_Λ governs the expansion rate of the universe and together with H_0, determines the age of the universe. τ is the reionization optical depth. n_s the power-law spectral index of primordial

density scalar perturbations, while A_s is the amplitude. These perturbations in the photon-baryon fluid collapsed under gravity, but the compression was opposed by radiation pressure, which resulted in acoustic oscillations. Because radiation only interacts with baryons, $\Omega_b h^2$ governs the amplitude of this oscillation. Knowledge of these six parameters allows us to predict the power spectrum of the CMB. Conversely one can estimate the distributions of the parameters from a power spectrum. When parameter fitting, one can also vary θ_{MC} (in place of H_0), which is the angular size of the sound horizon at photon decoupling.

1.5 Cosmological Parameter Estimation

I use a publicly available software package called CAMB (Lewis, Challinor, and Lasenby, 2000) to calculate the temperature power spectrum from input cosmological parameters and CosmoMC (Lewis and Bridle, 2002) to perform the Markov Chain Monte Carlo (MCMC) parameter fitting of data to CAMB-computed models.

To compute the power spectrum, CAMB evolves the Boltzmann equations that describe CMB anisotropies using a line of sight integration approach. Instead of trying to solve the hierarchy of coupled differential equations (one equation for each ℓ), CAMB integrates the Boltzmann equation, so that it can be rewritten in terms of a source term and a geometric term. The former only depends on multipole moments at $\ell < 4$. The latter does not depend on cosmological parameters and so can be computed in advance.

Another public available software package, CosmoMC, estimates the cosmological parameters by sampling points sequentially according to the Metropolis-Hastings Algorithm (Metropolis et al., 1953) and evaluating the likelihood at each point, which is defined as the probability of getting the data given the theory (Hobson and Maisinger, 2002):

$$\begin{aligned} \mathcal{L}(p) \quad &\propto \quad \frac{1}{\sqrt{2\pi|\Sigma|}} \times \\ &\exp[-\frac{1}{2}(\hat{D} - M(p))^T \Sigma^{-1} (\hat{D} - M(p)] \end{aligned} \tag{1.20}$$

where p stands for the set of parameters that give the model power spectrum $M(p)$. $\hat{D}$ is the power spectrum which can be extracted from CMB observations or generated from simulations. Σ is its covariance matrix. By running CosmoMC along with CAMB, marginalized distributions of parameters can be obtained.

References

Abbott, T. M. C. et al. (2018). "Dark Energy Survey year 1 results: Cosmological constraints from galaxy clustering and weak lensing". In: *PRD* 98.4, 043526, p. 043526. DOI: 10.1103/PhysRevD.98.043526. arXiv: 1708.01530 [astro-ph.CO].

Addison, G. E., Y. Huang, D. J. Watts, C. L. Bennett, M. Halpern, G. Hinshaw, and J. L. Weiland (2016). "Quantifying Discordance in the 2015 Planck CMB Spectrum". In: *APJ* 818, 132, p. 132. DOI: 10.3847/0004-637X/818/2/132. arXiv: 1511.00055.

Addison, G. E., D. J. Watts, C. L. Bennett, M. Halpern, G. Hinshaw, and J. L. Weiland (2018). "Elucidating ΛCDM: Impact of Baryon Acoustic Oscillation Measurements on the Hubble Constant Discrepancy". In: *APJ* 853, 119, p. 119. DOI: 10.3847/1538-4357/aaa1ed. arXiv: 1707.06547 [astro-ph.CO].

Albrecht, Andreas and Paul J. Steinhardt (1982). "Cosmology for Grand Unified Theories with Radiatively Induced Symmetry Breaking". In: *Phys. Rev. Lett.* 48 (17), pp. 1220–1223. DOI: 10.1103/PhysRevLett.48.1220. URL: https://link.aps.org/doi/10.1103/PhysRevLett.48.1220.

Anderson, Lauren, Eric Aubourg, Stephen Bailey, Dmitry Bizyaev, Michael Blanton, Adam S. Bolton, J. Brinkmann, Joel R. Brownstein, Angela Burden, Antonio J. Cuesta, Luiz A. N. da Costa, Kyle S. Dawson, Roland de Putter, Daniel J. Eisenstein, James E. Gunn, Hong Guo, Jean-Christophe Hamilton, Paul Harding, Shirley Ho, Klaus Honscheid, Eyal Kazin, David Kirkby, Jean-Paul Kneib, Antoine Labatie, Craig Loomis, Robert H. Lupton, Elena Malanushenko, Viktor Malanushenko, Rachel Mandelbaum, Marc Manera, Claudia Maraston, Cameron K. McBride, Kushal T. Mehta, Olga Mena, Francesco Montesano, Demetri Muna, Robert C. Nichol, Sebastián E. Nuza, Matthew D. Olmstead, Daniel Oravetz, Nikhil Padmanabhan, Nathalie Palanque-Delabrouille, Kaike Pan, John Parejko, Isabelle Pâris, Will J. Percival, Patrick Petitjean, Francisco Prada, Beth Reid, Natalie A. Roe,

Ashley J. Ross, Nicholas P. Ross, Lado Samushia, Ariel G. Sánchez, David J. Schlegel, Donald P. Schneider, Claudia G. Scóccola, Hee-Jong Seo, Erin S. Sheldon, Audrey Simmons, Ramin A. Skibba, Michael A. Strauss, Molly E. C. Swanson, Daniel Thomas, Jeremy L. Tinker, Rita Tojeiro, Mariana Vargas Magaña, Licia Verde, Christian Wagner, David A. Wake, Benjamin A. Weaver, David H. Weinberg, Martin White, Xiaoying Xu, Christophe Yèche, Idit Zehavi, and Gong-Bo Zhao (2012). "The clustering of galaxies in the SDSS-III Baryon Oscillation Spectroscopic Survey: baryon acoustic oscillations in the Data Release 9 spectroscopic galaxy sample". In: *MNRAS* 427.4, pp. 3435–3467. DOI: 10.1111/j.1365-2966.2012.22066.x. arXiv: 1203.6594 [astro-ph.CO].

Aylor, Kevin, Mackenzie Joy, Lloyd Knox, Marius Millea, Srinivasan Raghunathan, and W. L. Kimmy Wu (2019). "Sounds Discordant: Classical Distance Ladder and ΛCDM-based Determinations of the Cosmological Sound Horizon". In: *APJ* 874.1, 4, p. 4. DOI: 10.3847/1538-4357/ab0898. arXiv: 1811.00537 [astro-ph.CO].

Becker, Robert H., Xiaohui Fan, Richard L. White, Michael A. Strauss, Vijay K. Narayanan, Robert H. Lupton, James E. Gunn, James Annis, Neta A. Bahcall, J. Brinkmann, A. J. Connolly, István Csabai, Paul C. Czarapata, Mamoru Doi, Timothy M. Heckman, G. S. Hennessy, Željko Ivezić, G. R. Knapp, Don Q. Lamb, Timothy A. McKay, Jeffrey A. Munn, Thomas Nash, Robert Nichol, Jeffrey R. Pier, Gordon T. Richards, Donald P. Schneider, Chris Stoughton, Alexand er S. Szalay, Aniruddha R. Thakar, and D. G. York (2001). "Evidence for Reionization at z∼6: Detection of a Gunn-Peterson Trough in a z=6.28 Quasar". In: *AJ* 122.6, pp. 2850–2857. DOI: 10.1086/324231. arXiv: astro-ph/0108097 [astro-ph].

Efstathiou, George (2014). "H_0 revisited". In: *MNRAS* 440.2, pp. 1138–1152. DOI: 10.1093/mnras/stu278. arXiv: 1311.3461 [astro-ph.CO].

Eisenstein, Daniel J., Idit Zehavi, David W. Hogg, Roman Scoccimarro, Michael R. Blanton, Robert C. Nichol, Ryan Scranton, Hee-Jong Seo, Max Tegmark, Zheng Zheng, Scott F. Anderson, Jim Annis, Neta Bahcall, Jon Brinkmann, Scott Burles, Francisco J. Castand er, Andrew Connolly, Istvan Csabai, Mamoru Doi, Masataka Fukugita, Joshua A. Frieman, Karl Glazebrook, James E. Gunn, John S. Hendry, Gregory Hennessy, Zeljko Ivezić, Stephen Kent, Gillian R. Knapp, Huan Lin, Yeong-Shang Loh, Robert H. Lupton, Bruce Margon, Timothy A. McKay, Avery Meiksin, Jeffery A. Munn, Adrian Pope, Michael W. Richmond, David Schlegel, Donald P. Schneider, Kazuhiro Shimasaku, Christopher Stoughton, Michael A. Strauss, Mark

SubbaRao, Alexander S. Szalay, István Szapudi, Douglas L. Tucker, Brian Yanny, and Donald G. York (2005). "Detection of the Baryon Acoustic Peak in the Large-Scale Correlation Function of SDSS Luminous Red Galaxies". In: *APJ* 633.2, pp. 560–574. DOI: 10.1086/466512. arXiv: astro-ph/0501171 [astro-ph].

Erben, T., H. Hildebrandt, L. Miller, L. van Waerbeke, C. Heymans, H. Hoekstra, T. D. Kitching, Y. Mellier, J. Benjamin, C. Blake, C. Bonnett, O. Cordes, J. Coupon, L. Fu, R. Gavazzi, B. Gillis, E. Grocutt, S. D. J. Gwyn, K. Holhjem, M. J. Hudson, M. Kilbinger, K. Kuijken, M. Milkeraitis, B. T. P. Rowe, T. Schrabback, E. Semboloni, P. Simon, M. Smit, O. Toader, S. Vafaei, E. van Uitert, and M. Velander (2013). "CFHTLenS: the Canada-France-Hawaii Telescope Lensing Survey - imaging data and catalogue products". In: *MNRAS* 433.3, pp. 2545–2563. DOI: 10.1093/mnras/stt928. arXiv: 1210.8156 [astro-ph.CO].

Fan, Xiaohui, Vijay K. Narayanan, Robert H. Lupton, Michael A. Strauss, Gillian R. Knapp, Robert H. Becker, Richard L. White, Laura Pentericci, S. K. Leggett, Zoltán Haiman, James E. Gunn, Željko Ivezić, Donald P. Schneider, Scott F. Anderson, J. Brinkmann, Neta A. Bahcall, Andrew J. Connolly, István Csabai, Mamoru Doi, Masataka Fukugita, Tom Geballe, Eva K. Grebel, Daniel Harbeck, Gregory Hennessy, Don Q. Lamb, Gajus Miknaitis, Jeffrey A. Munn, Robert Nichol, Sadanori Okamura, Jeffrey R. Pier, Francisco Prada, Gordon T. Richards, Alex Szalay, and Donald G. York (2001). "A Survey of z>5.8 Quasars in the Sloan Digital Sky Survey. I. Discovery of Three New Quasars and the Spatial Density of Luminous Quasars at z$_\sim$6". In: *AJ* 122.6, pp. 2833–2849. DOI: 10.1086/324111. arXiv: astro-ph/0108063 [astro-ph].

Fixsen, D. J. (2009). "THE TEMPERATURE OF THE COSMIC MICROWAVE BACKGROUND". In: *The Astrophysical Journal* 707.2, pp. 916–920. DOI: 10.1088/0004-637x/707/2/916. URL: https://doi.org/10.1088\%2F0004-637x%2F707%2F2%2F916.

Guth, Alan H. (1981). "Inflationary universe: A possible solution to the horizon and flatness problems". In: *Phys. Rev. D* 23 (2), pp. 347–356. DOI: 10.1103/PhysRevD.23.347. URL: https://link.aps.org/doi/10.1103/PhysRevD.23.347.

Hildebrandt, H., M. Viola, C. Heymans, S. Joudaki, K. Kuijken, C. Blake, T. Erben, B. Joachimi, D. Klaes, L. Miller, C. B. Morrison, R. Nakajima, G. Verdoes Kleijn, A. Amon, A. Choi, G. Covone, J. T. A. de Jong, A. Dvornik, I. Fenech Conti, A. Grado, J. Harnois-Déraps, R. Herbonnet, H.

Hoekstra, F. Köhlinger, J. McFarland, A. Mead, J. Merten, N. Napolitano, J. A. Peacock, M. Radovich, P. Schneider, P. Simon, E. A. Valentijn, J. L. van den Busch, E. van Uitert, and L. Van Waerbeke (2017). "KiDS-450: cosmological parameter constraints from tomographic weak gravitational lensing". In: *MNRAS* 465.2, pp. 1454–1498. DOI: 10.1093/mnras/stw2805. arXiv: 1606.05338 [astro-ph.CO].

Hill, J. Colin, Evan McDonough, Michael W. Toomey, and Stephon Alexander (2020). "Early Dark Energy Does Not Restore Cosmological Concordance". In: *arXiv e-prints*, arXiv:2003.07355, arXiv:2003.07355. arXiv: 2003.07355 [astro-ph.CO].

Hinshaw, G., D. Larson, E. Komatsu, D. N. Spergel, C. L. Bennett, J. Dunkley, M. R. Nolta, M. Halpern, R. S. Hill, N. Odegard, L. Page, K. M. Smith, J. L. Weiland, B. Gold, N. Jarosik, A. Kogut, M. Limon, S. S. Meyer, G. S. Tucker, E. Wollack, and E. L. Wright (2013). "Nine-year Wilkinson Microwave Anisotropy Probe (WMAP) Observations: Cosmological Parameter Results". In: *APJS* 208.2, 19, p. 19. DOI: 10.1088/0067-0049/208/2/19. arXiv: 1212.5226 [astro-ph.CO].

Hobson, M. P. and Klaus Maisinger (2002). "Maximum-likelihood estimation of the cosmic microwave background power spectrum from interferometer observations". In: *MNRAS* 334.3, pp. 569–588. DOI: 10.1046/j.1365-8711.2002.05524.x. arXiv: astro-ph/0201438 [astro-ph].

Hu, Wayne, Naoshi Sugiyama, and Joseph Silk (1997). "The physics of microwave background anisotropies". In: *NAT* 386.6620, pp. 37–43. DOI: 10.1038/386037a0. arXiv: astro-ph/9504057 [astro-ph].

Hu, Wayne and Martin White (1997). "The Damping Tail of Cosmic Microwave Background Anisotropies". In: *The Astrophysical Journal* 479.2, pp. 568–579. DOI: 10.1086/303928. URL: https://doi.org/10.1086\%2F303928.

Huang, Y., G. E. Addison, and C. L. Bennett (2019). "Accounting for Correlations When Fitting Extra Cosmological Parameters". In: *APJ* 882.2, 124, p. 124. DOI: 10.3847/1538-4357/ab3654. arXiv: 1904.10521 [astro-ph.CO].

Huang, Y., G. E. Addison, J. L. Weiland, and C. L. Bennett (2018). "Assessing Consistency between WMAP 9 Year and Planck 2015 Temperature Power Spectra". In: *APJ* 869, 38, p. 38. DOI: 10.3847/1538-4357/aaeb1f. arXiv: 1804.05428 [astro-ph.CO].

Ivanov, Mikhail M., Evan McDonough, J. Colin Hill, Marko Simonović, Michael W. Toomey, Stephon Alexand er, and Matias Zaldarriaga (2020). "Constraining Early Dark Energy with Large-Scale Structure". In: *arXiv e-prints*, arXiv:2006.11235, arXiv:2006.11235. arXiv: 2006.11235 [astro-ph.CO].

Joudaki, Shahab, Alexander Mead, Chris Blake, Ami Choi, Jelte de Jong, Thomas Erben, Ian Fenech Conti, Ricardo Herbonnet, Catherine Heymans, Hendrik Hildebrandt, Henk Hoekstra, Benjamin Joachimi, Dominik Klaes, Fabian Köhlinger, Konrad Kuijken, John McFarland, Lance Miller, Peter Schneider, and Massimo Viola (2017). "KiDS-450: testing extensions to the standard cosmological model". In: *MNRAS* 471, pp. 1259–1279. DOI: 10.1093/mnras/stx998. arXiv: 1610.04606 [astro-ph.CO].

Lewis, Antony and Sarah Bridle (2002). "Cosmological parameters from CMB and other data: A Monte Carlo approach". In: *PRD* 66.10, 103511, p. 103511. DOI: 10.1103/PhysRevD.66.103511. arXiv: astro-ph/0205436 [astro-ph].

Lewis, Antony, Anthony Challinor, and Anthony Lasenby (2000). "Efficient Computation of Cosmic Microwave Background Anisotropies in Closed Friedmann-Robertson-Walker Models". In: *APJ* 538.2, pp. 473–476. DOI: 10.1086/309179. arXiv: astro-ph/9911177 [astro-ph].

Linde, A.D. (1982). "A new inflationary universe scenario: A possible solution of the horizon, flatness, homogeneity, isotropy and primordial monopole problems". In: *Physics Letters B* 108.6, pp. 389 –393. ISSN: 0370-2693. DOI: https://doi.org/10.1016/0370-2693(82)91219-9. URL: http://www.sciencedirect.com/science/article/pii/0370269382912199.

Metropolis, Nicholas, Arianna W. Rosenbluth, Marshall N. Rosenbluth, Augusta H. Teller, and Edward Teller (1953). "Equation of State Calculations by Fast Computing Machines". In: *JCP* 21.6, pp. 1087–1092. DOI: 10.1063/1.1699114.

Planck Collaboration (2016). "Planck 2015 results. XIII. Cosmological parameters". In: *AAP* 594, A13, A13. DOI: 10.1051/0004-6361/201525830. arXiv: 1502.01589 [astro-ph.CO].

Planck Collaboration (2017). "Planck intermediate results. LI. Features in the cosmic microwave background temperature power spectrum and shifts in cosmological parameters". In: *AAP* 607, A95, A95. DOI: 10.1051/0004-6361/201629504. arXiv: 1608.02487 [astro-ph.CO].

Planck Collaboration (2018). "Planck 2018 results. VI. Cosmological parameters". In: *arXiv e-prints*, arXiv:1807.06209, arXiv:1807.06209. arXiv: 1807.06209 [astro-ph.CO].

Poulin, Vivian, Tristan L. Smith, Tanvi Karwal, and Marc Kamionkowski (2019). "Early Dark Energy can Resolve the Hubble Tension". In: *PRL* 122.22, 221301, p. 221301. DOI: 10.1103/PhysRevLett.122.221301. arXiv: 1811.04083 [astro-ph.CO].

Riess, Adam G. (2019). "The expansion of the Universe is faster than expected". In: *Nature Reviews Physics* 2.1, pp. 10–12. DOI: 10.1038/s42254-019-0137-0. arXiv: 2001.03624 [astro-ph.CO].

Riess, Adam G., Stefano Casertano, Wenlong Yuan, Lucas M. Macri, and Dan Scolnic (2019). "Large Magellanic Cloud Cepheid Standards Provide a 1% Foundation for the Determination of the Hubble Constant and Stronger Evidence for Physics beyond ΛCDM". In: *APJ* 876.1, 85, p. 85. DOI: 10.3847/1538-4357/ab1422. arXiv: 1903.07603 [astro-ph.CO].

Riess, Adam G., Lucas M. Macri, Samantha L. Hoffmann, Dan Scolnic, Stefano Casertano, Alexei V. Filippenko, Brad E. Tucker, Mark J. Reid, David O. Jones, Jeffrey M. Silverman, Ryan Chornock, Peter Challis, Wenlong Yuan, Peter J. Brown, and Ryan J. Foley (2016). "A 2.4% Determination of the Local Value of the Hubble Constant". In: *APJ* 826, 56, p. 56. DOI: 10.3847/0004-637X/826/1/56. arXiv: 1604.01424 [astro-ph.CO].

Sievers, Jonathan L., Renée A. Hlozek, Michael R. Nolta, Viviana Acquaviva, Graeme E. Addison, Peter A. R. Ade, Paula Aguirre, Mandana Amiri, John William Appel, L. Felipe Barrientos, Elia S. Battistelli, Nick Battaglia, J. Richard Bond, Ben Brown, Bryce Burger, Erminia Calabrese, Jay Chervenak, Devin Crichton, Sudeep Das, Mark J. Devlin, Simon R. Dicker, W. Bertrand Doriese, Joanna Dunkley, Rolando Dünner, Thomas Essinger-Hileman, David Faber, Ryan P. Fisher, Joseph W. Fowler, Patricio Gallardo, Michael S. Gordon, Megan B. Gralla, Amir Hajian, Mark Halpern, Matthew Hasselfield, Carlos Hernández-Monteagudo, J. Colin Hill, Gene C. Hilton, Matt Hilton, Adam D. Hincks, Dave Holtz, Kevin M. Huffenberger, David H. Hughes, John P. Hughes, Leopoldo Infante, Kent D. Irwin, David R. Jacobson, Brittany Johnstone, Jean Baptiste Juin, Madhuri Kaul, Jeff Klein, Arthur Kosowsky, Judy M. Lau, Michele Limon, Yen-Ting Lin, Thibaut Louis, Robert H. Lupton, Tobias A. Marriage, Danica Marsden, Krista Martocci, Phil Mauskopf, Michael McLaren, Felipe Menanteau, Kavilan Moodley, Harvey Moseley, Calvin B. Netterfield, Michael D. Niemack, Lyman A. Page, William A. Page, Lucas Parker, Bruce Partridge, Reed Plimpton, Hernan Quintana, Erik D. Reese, Beth Reid, Felipe Rojas, Neelima Sehgal, Blake D. Sherwin, Benjamin L. Schmitt, David N. Spergel, Suzanne T. Staggs, Omelan Stryzak, Daniel S. Swetz, Eric R. Switzer, Robert Thornton, Hy Trac, Carole Tucker, Masao Uehara, Katerina Visnjic, Ryan Warne, Grant Wilson, Ed Wollack, Yue Zhao, and Caroline Zunckel (2013). "The Atacama Cosmology Telescope: cosmological parameters from three seasons of

data". In: *JCAP* 2013.10, 060, p. 060. DOI: 10.1088/1475-7516/2013/10/060. arXiv: 1301.0824 [astro-ph.CO].

Smith, Tristan L., Vivian Poulin, and Mustafa A. Amin (2020). "Oscillating scalar fields and the Hubble tension: A resolution with novel signatures". In: *PRD* 101.6, 063523, p. 063523. DOI: 10.1103/PhysRevD.101.063523. arXiv: 1908.06995 [astro-ph.CO].

Story, K. T., C. L. Reichardt, Z. Hou, R. Keisler, K. A. Aird, B. A. Benson, L. E. Bleem, J. E. Carlstrom, C. L. Chang, H.-M. Cho, T. M. Crawford, A. T. Crites, T. de Haan, M. A. Dobbs, J. Dudley, B. Follin, E. M. George, N. W. Halverson, G. P. Holder, W. L. Holzapfel, S. Hoover, J. D. Hrubes, M. Joy, L. Knox, A. T. Lee, E. M. Leitch, M. Lueker, D. Luong-Van, J. J. McMahon, J. Mehl, S. S. Meyer, M. Millea, J. J. Mohr, T. E. Montroy, S. Padin, T. Plagge, C. Pryke, J. E. Ruhl, J. T. Sayre, K. K. Schaffer, L. Shaw, E. Shirokoff, H. G. Spieler, Z. Staniszewski, A. A. Stark, A. van Engelen, K. Vanderlinde, J. D. Vieira, R. Williamson, and O. Zahn (2013). "A MEASUREMENT OF THE COSMIC MICROWAVE BACKGROUND DAMPING TAIL FROM THE 2500-SQUARE-DEGREE SPT-SZ SURVEY". In: *The Astrophysical Journal* 779.1, p. 86. DOI: 10.1088/0004-637x/779/1/86. URL: https://doi.org/10.1088%2F0004-637x%2F779%2F1%2F86.

Wong, Kenneth C., Sherry H. Suyu, Geoff C. F. Chen, Cristian E. Rusu, Martin Millon, Dominique Sluse, Vivien Bonvin, Christopher D. Fassnacht, Stefan Taubenberger, Matthew W. Auger, Simon Birrer, James H. H. Chan, Frederic Courbin, Stefan Hilbert, Olga Tihhonova, Tommaso Treu, Adriano Agnello, Xuheng Ding, Inh Jee, Eiichiro Komatsu, Anowar J. Shajib, Alessandro Sonnenfeld, Roger D. Bland ford, Léon V. E. Koopmans, Philip J. Marshall, and Georges Meylan (2020). "H0LiCOW XIII. A 2.4% measurement of H_0 from lensed quasars: 5.3σ tension between early and late-Universe probes". In: *MNRAS*. DOI: 10.1093/mnras/stz3094. arXiv: 1907.04869 [astro-ph.CO].

Zhao, Gong-Bo, Marco Raveri, Levon Pogosian, Yuting Wang, Robert G. Crittenden, Will J. Handley, Will J. Percival, Florian Beutler, Jonathan Brinkmann, Chia-Hsun Chuang, Antonio J. Cuesta, Daniel J. Eisenstein, Francisco-Shu Kitaura, Kazuya Koyama, Benjamin L'Huillier, Robert C. Nichol, Matthew M. Pieri, Sergio Rodriguez-Torres, Ashley J. Ross, Graziano Rossi, Ariel G. Sánchez, Arman Shafieloo, Jeremy L. Tinker, Rita Tojeiro, Jose A. Vazquez, and Hanyu Zhang (2017). "Dynamical dark energy in light of the latest observations". In: *Nature Astronomy* 1, pp. 627–632. DOI: 10.1038/s41550-017-0216-z. arXiv: 1701.08165 [astro-ph.CO].

Chapter 2

Quantifying Discordance in the 2015 *Planck* CMB spectrum

This chapter is a verbatim reprint from Addison & Huang et al 2016 (*APJ 818, 132, p. 132*), where we examine the internal consistency of the *Planck* 2015 cosmic microwave background (CMB) temperature anisotropy power spectrum. In this work, I perform parameter fitting on low and high multipole ranges of the *Planck* temperature power spectrum and quantitatively compare results from these fits. We find tension exists between model parameters inferred from different parts of the power spectrum. We find some parameter tensions to be larger than previously reported because of inaccuracy in the code used by the *Planck* Collaboration to generate model spectra. To further investigate the tension, I repeat the parameter fitting with the optical depth to reioniation and the phenomenological lensing amplitude set to different values. We find that internal tension within *Planck* data persists. In addition, the Planck $\ell \geq 1000$ constraints are also in tension with low-redshift data sets, including *Planck*'s own measurement of the CMB lensing power spectrum and the local distance ladder measurement.

2.1 Introduction

Measurements of the power spectrum of CMB temperature fluctuations (hereafter 'TT spectrum') are a cornerstone of modern cosmology. The most precise constraints are currently provided by the final 9-year *Wilkinson Microwave Anisotropy Probe* (*WMAP*) analysis (Bennett et al., 2013; Hinshaw et al., 2013), high-resolution ground-based instruments including the Atacama Cosmology Telescope (ACT; Sievers et al., 2013) and the South Pole Telescope (SPT; Story et al., 2013), and most recently *Planck* (Planck Collaboration XIII, 2016). Significant improvements in both CMB polarization and low-redshift, late-time observations are anticipated in the near future and will be used to measure or tightly constrain key cosmological quantities including the total neutrino mass, deviations of dark energy from a cosmological constant and the amplitude of primordial gravitational waves (e.g., Abazajian et al., 2015a; Abazajian et al., 2015b; Kim et al., 2015). Many of these future results will rely on having precise and accurate TT constraints. Assessing consistency both between and internally within each TT measurement is therefore extremely important.

While the *Planck* data from the first data release in 2013 (Planck Collaboration XVI, 2014) were qualitatively in agreement with *WMAP*, supporting the minimal ΛCDM model, there were small but highly significant quantitative differences between the cosmological parameters inferred. For example, Larson et al. (2015) found a $\sim 6\sigma$ overall parameter discrepancy after accounting for the cosmic variance common to both experiments.

Several systematic effects were corrected in the *Planck* 2015 data release,

including issues relating to data calibration and map making (Planck Collaboration, 2016a), which led to a shift in the inferred TT power spectrum amplitude by 3.5σ in units of the 2015 uncertainty (Table 1 of Planck Collaboration XIII, 2016), and an artifact with a statistical significance of $2.4 - 3.1\sigma$ near multipole $\ell \simeq 1800$ in the 217 GHz temperature power spectrum (Planck Collaboration, 2014). See also discussion in Spergel, Flauger, and Hložek (2015).

The *WMAP* and *Planck* 2015 TT spectra appear to be in agreement over their common multipole range (Fig. 46 of Planck Collaboration XI, 2016). When the additional information in the high-order acoustic peaks and damping tail of the TT spectrum are included, however, the *Planck* parameters pull away from *WMAP* (Section 4.1.6 of Planck Collaboration XI, 2016), leading to tension between *Planck* and several low-redshift cosmological measurements if ΛCDM is assumed, including a 2.5σ tension with the Riess et al. (2011) determination of the Hubble constant, H_0, $2 - 3\sigma$ tension with weak lensing measurements of the CFHTLens survey (Heymans et al., 2012), and tension with the abundance of massive galaxy clusters (e.g., Planck Collaboration, 2016b).

In this chapter we examine the internal consistency of the *Planck* TT spectrum. We show that tension exists between ΛCDM parameters inferred from the *Planck* TT spectrum at the multipoles accessible to *WMAP* ($\ell \lesssim 1000$) and at higher multipoles ($\ell \gtrsim 1000$). The constraints from high multipoles are, furthermore, in tension with many low-redshift cosmological measurements, including *Planck*'s own lensing potential power spectrum measurement

and baryon acoustic oscillation (BAO) from galaxy surveys, while the low-multipole *Planck* TT, *Planck* lensing, *WMAP*, BAO, and distance ladder H_0 data are all in reasonable agreement.

We describe the data sets used and parameter fitting methodology in Section 2.2 and present results in Section 2.3. Discussions and conclusions follow in Sections 2.4 and 2.5.

2.2 Data and Parameter Fitting

We use CAMB[1] (Lewis, Challinor, and Lasenby, 2000) to calculate temperature and lensing potential power spectra as a function of cosmological parameters and `CosmoMC`[2] (Lewis and Bridle, 2002) to perform Monte-Carlo Markov Chain (MCMC) parameter fitting and obtain marginalized parameter distributions, adopting the default *Planck* settings, including a neutrino mass of 0.06 eV (Planck Collaboration XVI, 2014). We use the public temperature-only *Planck* 2015 `lowl` likelihood for $2 \leq \ell \leq 29$, the binned `plik` likelihood for $30 \leq \ell \leq 2508$, and, in some cases, the *Planck* 2015 lensing likelihood, which includes multipoles of the lensing potential power spectrum $C_L^{\phi\phi}$ covering $40 \leq L \leq 400$ (Planck Collaboration XI, 2016; Planck XV et al., 2015). We fit for six ΛCDM parameters: the physical baryon and CDM densities, $\Omega_b h^2$ and $\Omega_c h^2$, the angular acoustic scale, parametrized by $\theta_{\rm MC}$, the optical depth, τ, the primordial scalar fluctuation amplitude, A_s, and the scalar spectral index, n_s.

[1] `camb.info`
[2] `http://cosmologist.info/cosmomc/`

Other parameters, including H_0, the total matter density, Ω_m, and the present-day mass fluctuation amplitude, σ_8, are derived from these six. Additional foreground and calibration parameters used in the fits are described by Planck Collaboration XI (2016).

At of the completion of this work, the analysis of *Planck*'s polarization data is only partially complete. At high multipoles, significant systematic errors remain in the TE and EE spectra, putatively due to beam mismatch, which leads to temperature-polarization leakage (Sec. 3.3.2 of Planck Collaboration XIII, 2016). At low multipoles ($\ell < 30$), the 100, 143 and 217 GHz polarization data have significant residual systematic errors and are "not considered usable for cosmological analyses"[3]. The LFI 70 GHz data, in conjunction with the 30 and 353 GHz maps as Galactic foreground tracers, are used to constrain τ. Using the polarized 353 GHz map as a dust tracer results in a value of τ lower than constraints from *WMAP* (0.066 ± 0.016 compared to 0.089 ± 0.014, Hinshaw et al., 2013; Planck Collaboration XIII, 2016). Given these complexities and uncertainties, we have chosen to leave polarization data out of the current analysis and focus on conclusions that can be drawn from the TT data alone.

Without polarization data, τ is only weakly constrained, but it does couple to other cosmological parameters. We considered two approaches for setting priors on τ. First we adopted a Gaussian prior of $\tau = 0.07 \pm 0.02$ as in Planck Collaboration XI (2016), which is consistent within 1σ with the range of values inferred from *WMAP* and *Planck* data (Hinshaw et al., 2013; Planck

[3]According to the *Planck* 2015 Release Explanatory Supplement http://wiki.cosmos.esa.int/planckpla2015/index.php/Frequency_Maps#Caveats_and_known_issues

Collaboration XIII, 2016). Second, to gain more insight into exactly how τ does or does not affect our conclusions about TT consistency, we also ran chains with τ fixed to specific values: 0.06, 0.07, 0.08, and 0.09.

When assessing consistency between parameter constraints from two data sets that can be considered independent we use the difference of mean parameter values, which we treat as multivariate Gaussian with zero mean and covariance given by the sum of the covariance matrices from the individual data sets. The mean and covariance for each data set are estimated from the MCMC chains. We then quote equivalent Gaussian 'sigma' levels for the significance of the parameter differences.

We also considered using the difference of best-fit parameters, rather than difference of means, for these comparisons. For Gaussian posterior distributions this choice should make little difference. We find that this is generally true, with significance levels for parameter differences changing only at the $0.1 - 0.2\sigma$ level. In a few cases, however, we found a significant shift, due to an offset between the mean and best-fit parameters. In all cases the Gaussian distribution specified by the mean and covariance matrix from the chains provided an excellent match to the distribution of the actual MCMC samples, and for this reason we quote results based on the differences of the mean rather than best-fit parameters. It is possible that the mismatches are caused by problems in the algorithm used to determine the best-fit parameters[4]. Note that simply taking the maximum-likelihood parameters directly from the MCMC chains is unreliable due to the large parameter volume sampled (typically

[4]See http://cosmologist.info/cosmomc/readme.html

around 20 parameters, including nuisance parameters, e.g., for foregrounds). The overall posterior distribution is well mapped out by a converged chain but the tiny region of parameter space close to the likelihood peak is not.

2.3 Results

Figure 2.1 shows the two-dimensional ΛCDM parameter constraints for the *Planck* 2015 TT spectra spanning $2 \leq \ell < 1000$ and $1000 \leq \ell \leq 2508$, with a $\tau = 0.07 \pm 0.02$ prior. Similar contours are shown in Figure 31 of Planck Collaboration XI (2016) using the same prior on τ. Two differences in our fit act to pull some of the low and high multipole parameter constraints away from one another. Firstly, the constraints in the *Planck* figure only extend down to $\ell = 30$ because the intention was to test robustness of the `plik` likelihood only. We use the full range $2 \leq \ell < 1000$ with the intention of examining parameter values. Secondly, the *Planck* fit uses the *PICO*[5] (Fendt and Wandelt, 2007) code rather than CAMB to generate TT spectra. We find that the *PICO* and CAMB results are noticeably different for the $1000 \leq \ell \leq 2508$ fit. *PICO* requires only a fraction of the computation time and provides a good approximation to CAMB, but only within a limited volume of parameter space. Some parameter combinations outside this volume are allowed by the $1000 \leq \ell \leq 2508$ data. In these cases, the *PICO* output deviates from the CAMB spectrum and a poor likelihood is returned, leading to artificial truncation of the contours, particularly for $\Omega_b h^2$ and n_s.

From Figure 2.1 it is clear that some tension exists between parameters

[5] https://pypi.python.org/pypi/pypico

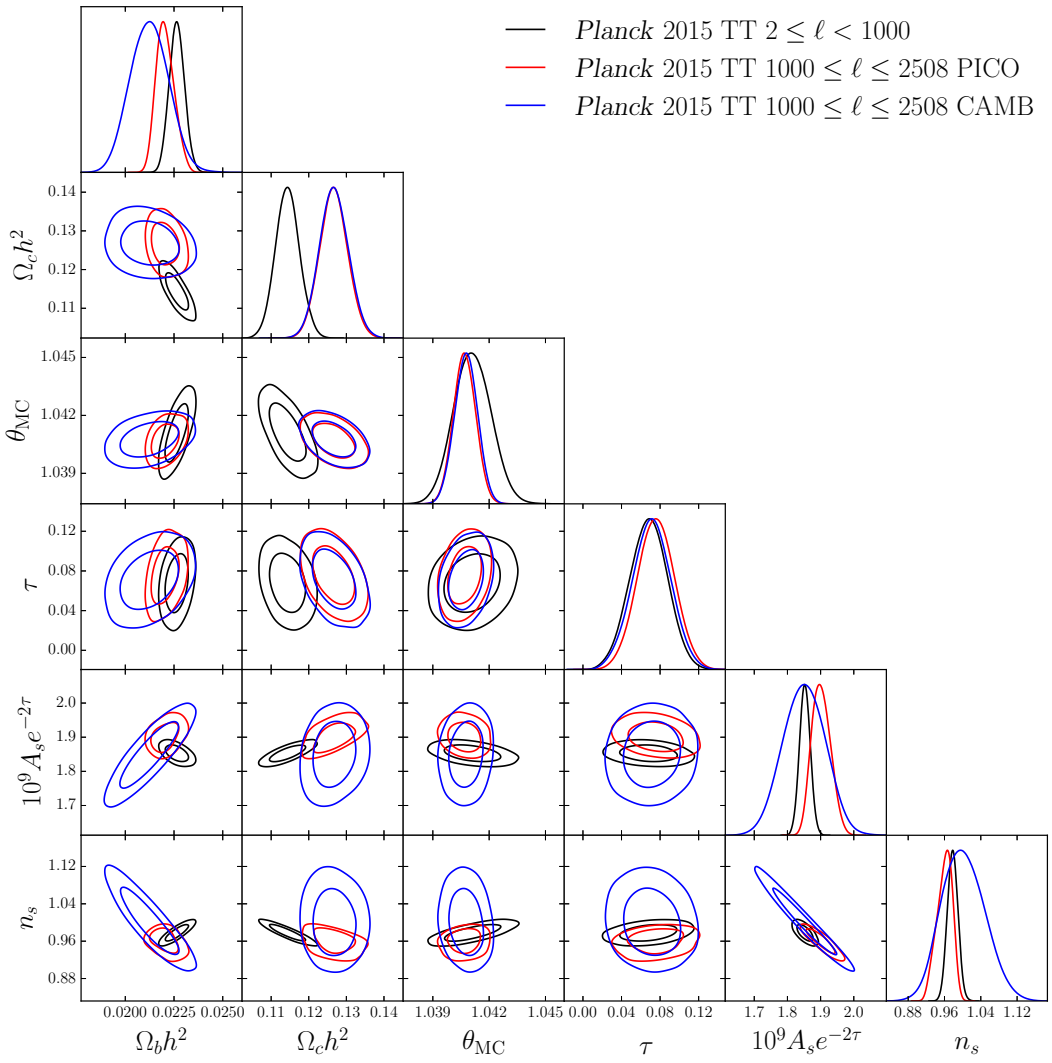

Figure 2.1: Contours enclosing 68.3% and 95.5% of MCMC sample points from fits to the *Planck* TT spectrum.

Results are shown for $2 \leq \ell < 1000$, roughly the multipole range accessible to *WMAP*, and higher multipoles, $1000 \leq \ell \leq 2508$. These constraints are effectively independent and are in tension, for example $\Omega_c h^2$ differs by 2.5σ. Results are also shown for the $1000 \leq \ell \leq 2508$ fit where the *PICO* code is used to estimate the theoretical TT spectra instead of the more accurate CAMB. Using *PICO* leads to an artificial truncation of the contours and diminishes the discrepancy between the high and low multipole fits for some parameters. We adopt a Gaussian prior of $\tau = 0.07 \pm 0.02$.

inferred from the $\ell < 1000$ and $\ell \geq 1000$ *Planck* TT spectra. Assuming the two sets of constraints are independent, the values of $\Omega_c h^2$ differ by 2.5σ. Independence is a valid assumption because even the bins on either side of the $\ell = 1000$ split point are only correlated at the 4% level and the degree of correlation falls off with increasing bin separation. Taken together the five free ΛCDM parameters differ by 1.8σ, however it should be noted that $\Omega_c h^2$ plays a far more significant role in comparisons with low-redshift cosmological constraints (Section 2.3.3) than, for example, $\theta_{\rm MC}$.

For fixed τ we find differences in $\Omega_c h^2$ of 3.0, 2.7, 2.9, and 2.1σ for τ values of 0.06, 0.07, 0.08 and 0.09, respectively. Constraints on each parameter for these cases are shown in Figure 2.2. Apart from the expected strong correlation with A_s (the TT power spectrum amplitude scales as $A_s e^{-2\tau}$) there is relatively little variation with τ. Note that while increasing τ reduces the tension in $\Omega_c h^2$, higher values of τ are mildly disfavored by *Planck*'s own polarization analysis (Planck Collaboration XIII, 2016).

We investigated the effect of fixing the foreground parameters to the best-fit values inferred from the fit to the whole *Planck* multipole range rather than allowing them to vary separately in the $\ell < 1000$ and $\ell \geq 1000$ fits. This helps break degeneracies between foreground and ΛCDM parameters and leads to small shifts in ΛCDM parameter agreement, with the tension in $\Omega_c h^2$ decreasing to 2.3σ for $\tau = 0.07 \pm 0.02$, for example. The best-fit χ^2 is, however, worse by 3.1 and 4.8 for the $\ell < 1000$ and $\ell \geq 1000$ fits, respectively, reflecting the fact that the $\ell < 1000$ and $\ell \geq 1000$ data mildly prefer different foreground parameters. Overall the choice of foreground parameters does not

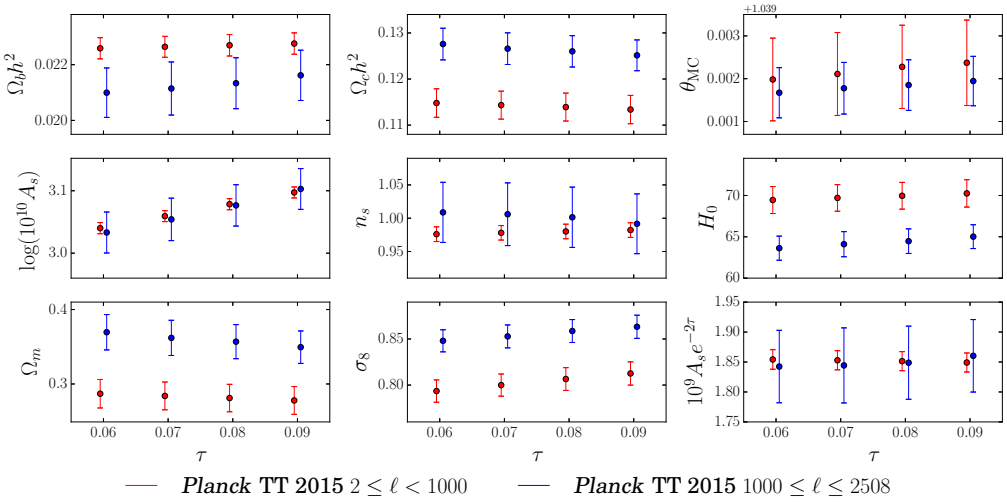

Figure 2.2: Marginalized confidence ΛCDM parameter constraints from fits to the $\ell < 1000$ and $\ell \geq 1000$ *Planck* TT spectra.

Here we replace the prior on τ with fixed values of 0.06, 0.07, 0.08, and 0.09, to more clearly assess the effect τ has on other parameters in these fits. Aside from the strong correlation with A_s, which arises because the TT spectrum amplitude scales as $A_s e^{-2\tau}$, dependence on τ is fairly weak. Tension at the $> 2\sigma$ level is apparent in $\Omega_c h^2$ and derived parameters, including H_0, Ω_m, and σ_8.

significantly impact our conclusions.

2.3.1 Comparing Temperature and Lensing Spectra

Planck Collaboration XIII (2016) found that allowing a non-physical enhancement of the lensing effect in the TT power spectrum, parametrized by the amplitude parameter A_L (Calabrese et al., 2008), was effective at relieving the tension between the low and high multipole *Planck* TT constraints. For the range of scales covered by *Planck*, the main effect of increasing A_L is to slightly smooth out the acoustic peaks. If ΛCDM parameters are fixed, a 20% change in A_L suppresses the fourth and higher peaks by around 0.5% and raises troughs by around 1%, for example.

In Figure 2.3 we show the effect of fixing A_L to values other than the physical value of unity on the $\ell < 1000$ and $\ell \geq 1000$ parameter comparison, for $\tau = 0.07 \pm 0.02$. For $A_L > 1$ the parameters from $\ell \geq 1000$ shift toward the $\ell < 1000$ results, resulting in lower values of $\Omega_c h^2$ and higher values of H_0. Planck Collaboration XIII (2016) found $A_L = 1.22 \pm 0.10$ for `plik` combined with the low-ℓ *Planck* joint temperature and polarization likelihood, although note that this fit was performed using *PICO* rather than CAMB, which uses a somewhat different A_L definition.

Lensing also induces specific non-Gaussian signatures in CMB maps that can be used to recover the lensing potential power spectrum (hereafter '$\phi\phi$ spectrum'). Planck XV et al. (2015) report a measurement of the $\phi\phi$ spectrum using temperature and polarization data with a combined significance of $\sim 40\sigma$. The $\phi\phi$ spectrum constrains $\sigma_8 \Omega_m^{0.25} = 0.591 \pm 0.021$, assuming priors of

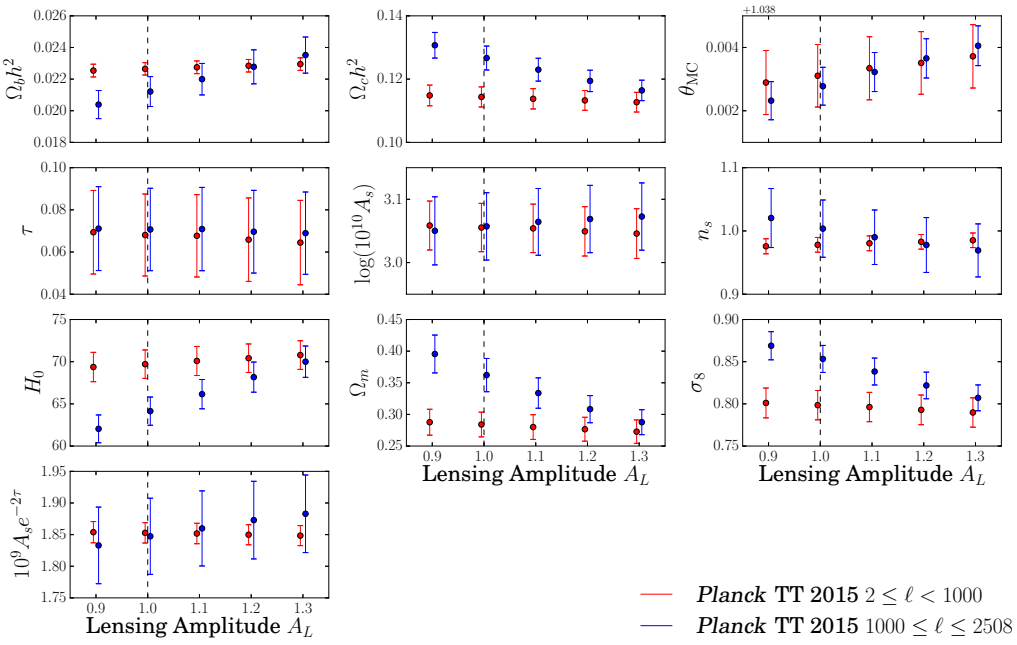

Figure 2.3: Marginalized parameter constraints from fits to TT spectra with different values of A_L

Here are marginalized 68.3% parameter constraints from fits to the $\ell < 1000$ and $\ell \geq 1000$ *Planck* TT spectra with different values of the phenomenological lensing amplitude parameter, A_L, which has a physical value of unity (dashed line). Increasing A_L smooths out the high order acoustic peaks, which improves agreement between the two multipole ranges. Note that a high value of A_L is not favored by the direct measurement of the $\phi\phi$ lensing potential power spectrum (see text).

$\Omega_b h^2 = 0.0223 \pm 0.0009$, $n_s = 0.96 \pm 0.02$, and $0.4 < H_0/100 \text{ km s}^{-1} \text{ Mpc}^{-1} < 1.0$ (Planck XV et al., 2015). We computed constraints on this same parameter combination from *Planck* TT data using a $\tau = 0.07 \pm 0.02$ prior:

$$\begin{aligned} \sigma_8 \Omega_m^{0.25} &= 0.591 \pm 0.021 \text{ (\textit{Planck} 2015 } \phi\phi), \\ &= 0.583 \pm 0.019 \text{ (\textit{Planck} 2015 TT } \ell < 1000), \\ &= 0.662 \pm 0.020 \text{ (\textit{Planck} 2015 TT } \ell \geq 1000). \end{aligned} \tag{2.1}$$

The $\ell < 1000$ and $\ell \geq 1000$ TT values differ by 2.9σ, consistent with the difference in $\Omega_c h^2$ discussed above. The $\ell \geq 1000$ and $\phi\phi$ values are in tension at the 2.4σ level (for fixed values of τ in the range $0.06 - 0.09$ we find a $2.4 - 2.5\sigma$ difference). The $\ell < 1000$ TT and $\phi\phi$ values are consistent within 0.3σ.

It is worth noting that while allowing $A_L > 1$ does relieve tension between the low-ℓ and high-ℓ TT results, it does not alleviate the high-ℓ TT tension with $\phi\phi$. For $A_L = 1.2$ (by the CAMB definition) we find $\sigma_8 \Omega_m^{0.25} = 0.612 \pm 0.019$ from $\ell \leq 1000$, while the $\phi\phi$ spectrum requires $\sigma_8 \Omega_m^{0.25} = 0.541 \pm 0.019$. This is because the $\phi\phi$ power roughly scales as $A_L(\sigma_8 \Omega_m^{0.25})^2$, so, for fixed $\phi\phi$, increasing A_L by 20% requires a $\sim$ 10% decrease in $\sigma_8 \Omega_m^{0.25}$. As shown in Figure 2.4, there is no value of A_L that produces agreement between these data.

The $\phi\phi$ spectrum featured prominently in the *Planck* claim that the true value of τ is lower than the value inferred by *WMAP* (Planck Collaboration XIII, 2016). While a full investigation into τ is deferred to future work we note here that the effect of the $\phi\phi$ spectrum on τ is completely dependent

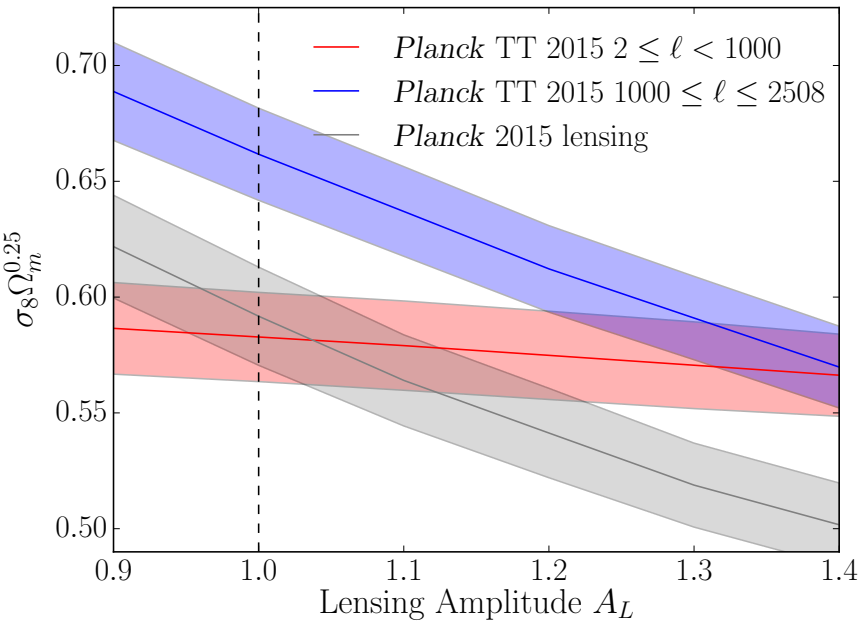

Figure 2.4: Parameter constraints on $\sigma_8\Omega_m^{0.25}$ from fits to Planck TT spectra and lensing spectrum.

Here shows constraints on $\sigma_8\Omega_m^{0.25}$ from fits to the $\ell < 1000$ and $\ell \geq 1000$ Planck TT spectra, and to the Planck $\phi\phi$ lensing spectrum. Results are shown as a function of the phenomenological lensing amplitude parameter A_L. The $\phi\phi$ measurement constrains the product $A_L(\sigma_8\Omega_m^{0.25})^2$. A similar trend is apparent in the $\ell \geq 1000$ constraint, where lensing has a significant effect. For $\ell < 1000$ the lensing effect is small, resulting in almost no dependence on A_L. The $\ell < 1000$ and $\phi\phi$ constraints agree well for the physical value of $A_L = 1$ (dashed line). Increasing A_L helps reconcile the low-ℓ and high-ℓ constraints but does not improve agreement between the high-ℓ and $\phi\phi$ constraints.

on the choice of temperature and polarization data. The shift to lower τ in the joint *Planck* 2015 TT-$\phi\phi$ fit is partly a reflection of the tension discussed above. Adding the *Planck* $\phi\phi$ spectrum to the *WMAP*9 data, in contrast, leads to no measurable shift in τ at all, reflecting the fact that the $\phi\phi$ spectrum and *WMAP* temperature and polarization data (with $\tau = 0.089 \pm 0.014$) are in excellent agreement. Figure 2.5 shows that, while some parameter constraints are tightened by a factor of two over *WMAP* alone, the mean values shift by $< 0.25\sigma$.

2.3.2 Comparison With SPT

Planck Collaboration XVI (2014) reported moderate to strong tension between cosmological parameters from the SPT TT spectrum, derived from mapping over 2500 square degrees of the sky and covering $650 \leq \ell \leq 3000$ (Story et al., 2013), and the *Planck* TT spectrum. Planck Collaboration XIII (2016) comment that this tension has worsened for the *Planck* 2015 data. A detailed comparison of these data sets is beyond the scope of this work, however we note that when we recalibrate the public SPT spectrum to the full-sky *Planck* 2015 spectrum following the method described by Story et al. (2013), using data from $650 \leq \ell \leq 1000$ and correcting for foregrounds, we recover the original SPT calibration to *WMAP* within 0.3σ. For the 143 GHz *Planck* spectrum, most directly comparable to the 150 GHz SPT channel, the agreement is better than 0.1σ. The disagreement between SPT and *Planck* therefore cannot be resolved by simply calibrating SPT to *Planck* rather than *WMAP* in this manner. We note that the high-multipole ACT TT measurements are consistent with *WMAP*

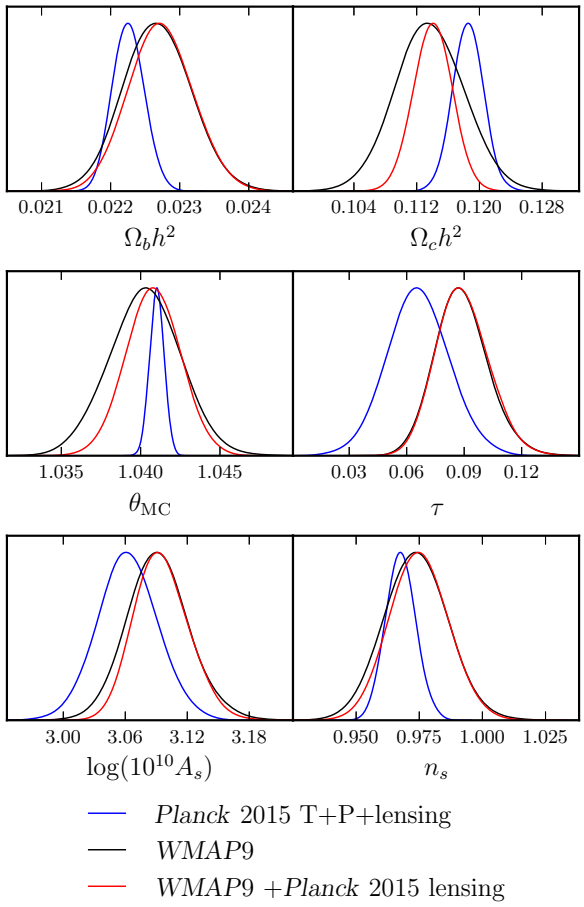

Figure 2.5: Marginalized parameter constraints comparing results from *Planck* 2015 and *WMAP*9.

Here are marginalized ΛCDM parameter constraints comparing results from *Planck* 2015 (combined temperature, polarization and lensing) with *WMAP*9 alone and *WMAP*9 in conjunction with the *Planck* $\phi\phi$ lensing power spectrum. Adding the $\phi\phi$ spectrum to *Planck* temperature and polarization data results in a downward shift in τ, which reflects internal tension between the high-multipole *Planck* TT spectrum and $\phi\phi$ (see text). The *WMAP*9 and *Planck* $\phi\phi$ constraints are in very good agreement. Adding $\phi\phi$ to *WMAP* leads to a negligible shift in τ and shifts of $< 0.25\sigma$ in other parameters.

and SPT, as well as *Planck* 2013 if a recalibration is allowed (Calabrese et al., 2013; Louis et al., 2014), and so do not currently help our understanding of these tensions. More precise upcoming measurements from ACTPol will be useful for future comparisons.

2.3.3 Comparison With BAO and Local H_0 Measurements

Figure 2.6 shows a comparison of CMB ΛCDM constraints with the 1% BAO scale measurement from the Baryon Oscillation Spectroscopic Survey (BOSS) 'CMASS' galaxy sample at an effective $z = 0.57$ (Anderson et al., 2014) and the most precise local distance ladder constraint on the Hubble constant, $H_0 = 73.0 \pm 2.4$ km s^{-1} Mpc^{-1} (Riess et al., 2011; Bennett et al., 2014). The BAO scale is parametrized as the ratio of the combined radial and transverse dilation scale, D_V (Eisenstein et al., 2005), to the sound horizon at the drag epoch, r_d, which has a fiducial value $r_{d,\mathrm{fid}} = 149.28$ Mpc (Anderson et al., 2014).

The BOSS BAO D_V/r_d constraint is at the higher end of the range preferred by *WMAP* and *Planck* $\ell < 1000$, though consistent within 1σ. The *Planck* $\ell \geq 1000$ data predict higher values of D_V/r_d, and lower values of H_0, than the BOSS BAO and distance ladder measurements at the 2.5σ and 3.0σ level, respectively, for $\tau = 0.07 \pm 0.02$. The difference between the *Planck* high-multipole constraint and the Riess *et al.* H_0 constraint is extremely unlikely to be explained by statistical fluctuation alone. The SPT-only values provided by Story et al. (2013)[6] are also shown. The SPT predictions for D_V/r_d and H_0 are

[6] http://pole.uchicago.edu/public/data/story12/chains/

discrepant with those from *Planck* $\ell \geq 1000$ at the 2.6σ and 2.7σ levels. Note that SPT used a *WMAP*-based τ prior but that τ couples very weakly to the inferred BAO scale.

The consistency between the *Planck* and BAO constraints has been repeatedly highlighted (Planck Collaboration XVI, 2014; Planck Collaboration XIII, 2016). We find that this agreement arises more in spite of than because of the high-multipole TT spectrum that *WMAP* did not measure. Figure 2.7 shows constraints in the $\Omega_m - H_0$ plane from combining BOSS CMASS with the BOSS 'LOWZ' sample (Anderson et al., 2014), Sloan Digital Sky Survey Main Galaxy Sample (Ross et al., 2015, SDSS MGS), and Six-degree-Field Galaxy Survey (Beutler et al., 2011, 6dFGS) measurements. This is the same combination utilized in the *Planck* 2015 cosmological analysis. The BAO contours are plotted assuming $\Omega_b h^2 = 0.02223$, although the exact choice has little effect (Addison, Hinshaw, and Halpern, 2013; Bennett et al., 2014). CMB constraints are plotted for comparison. The $> 2\sigma$ tension between the *Planck* $\ell \geq 1000$ and BOSS BAO constraints persists with the full BAO dataset.

Bennett et al. (2014) combined *WMAP*9, ACT, SPT, BAO, and distance ladder measurements and found that these measurements are consistent and together constrain $H_0 = 69.6 \pm 0.7$ km s^{-1} Mpc^{-1}. This concordance value differs from the *Planck* $\ell \geq 1000$ constraint of 64.1 ± 1.7 km s^{-1} Mpc^{-1} at 3.1σ but agrees well with the *Planck* $\ell < 1000$ constraint of 69.7 ± 1.7 km s^{-1} Mpc^{-1}.

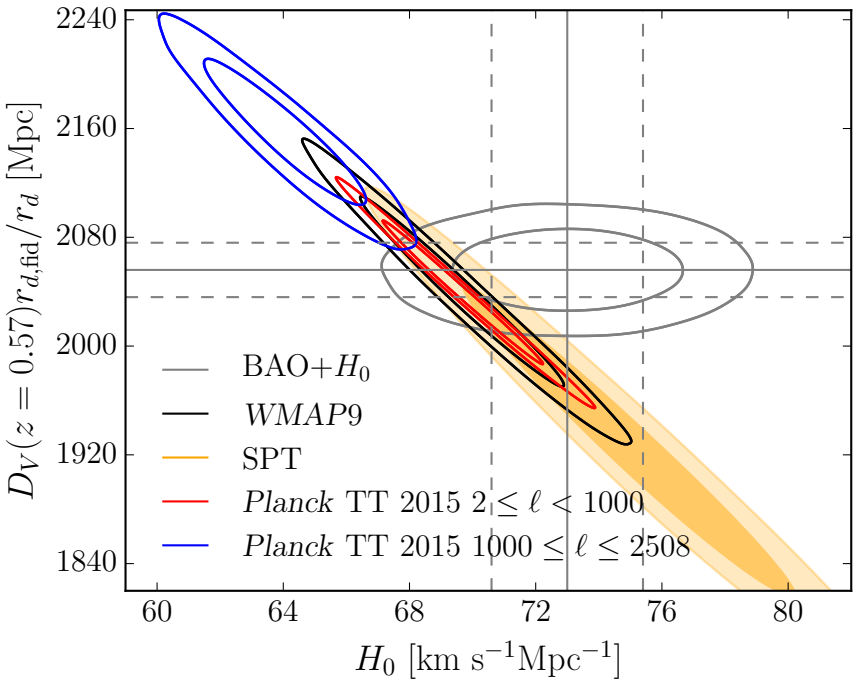

Figure 2.6: BAO scale and local distance ladder H_0 measurement from different data sets

Here are BOSS BAO scale and local distance ladder H_0 measurements (Riess et al., 2011; Anderson et al., 2014; Bennett et al., 2014) with ΛCDM CMB 68.3 and 94.5% confidence contours overplotted. The *Planck* $\ell \geq 1000$ constraints are discrepant with the BAO and distance ladder measurements at the 2.5σ and 3.0σ levels, respectively, while the *WMAP*9 and *Planck* $\ell < 1000$ constraints are consistent with both within 1σ. Constraints from SPT (covering $650 \leq \ell \leq 3000$) are also shown. *Planck* and SPT currently provide the most precise measurements of the CMB damping tail and their predictions for the $z = 0.57$ BAO scale and H_0 differ at the 2.6σ and 2.7σ level.

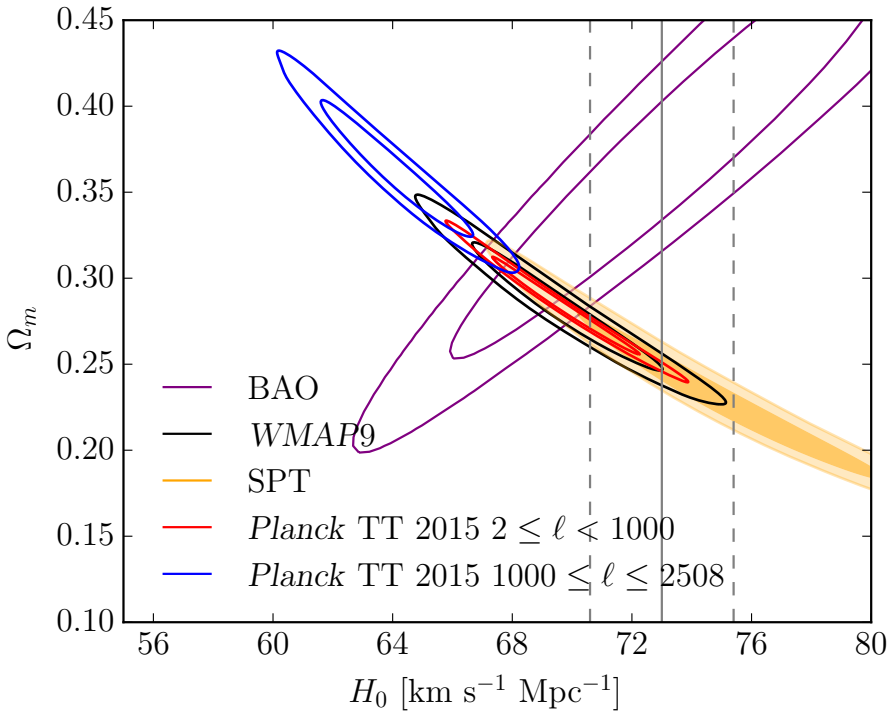

Figure 2.7: Comparison of CMB, BAO, and distance ladder constraints in the $\Omega_m - H_0$ plane

We show here the BAO constraints from combining the BOSS CMASS, BOSS LOWZ, SDSS MGS, and 6dFGRS measurements, assuming $\Omega_b h^2 = 0.0223$ (see text). The tension between *Planck* $\ell \geq 1000$ and BOSS CMASS BAO (Fig. 6) persists when comparing to the joint BAO constraint.

2.3.4 Choice of Multipole Split

The choice of $\ell = 1000$ as the split point for parameter comparisons matches the tests described by Planck Collaboration XI (2016) and roughly corresponds to the maximum multipoles accessible to *WMAP*, but the exact choice is arbitrary. To test the robustness of our findings we also considered the effect of splitting the *Planck* TT spectrum at $\ell = 800$. This choice achieves an almost-even division of the *Planck* TT spectrum constraining power as assessed by the determinants of the ΛCDM parameter covariance matrices from fits to $2 \leq \ell \leq 799$ and $800 \leq \ell \leq 2508$, which differ by only a few per cent.

Adding the $800 \leq \ell < 1000$ range, including the third acoustic peak, to the high-multipole *Planck* fit has a significant effect on several parameters, including n_s and $\Omega_b h^2$, tightening constraints on these parameters by factors of four and two, respectively. Conversely, the uncertainty on $\theta_{\rm MC}$ is increased by 50% for $\ell \leq 800$ compared to $\ell \leq 1000$. Despite these changes, the tensions discussed above for a split at $\ell = 1000$ remain for a split at $\ell = 800$, with the 2.5σ tension in $\Omega_c h^2$ for the $\ell = 1000$ split shifting to 2.7σ for the $\ell = 800$ case (assuming a $\tau = 0.07 \pm 0.02$ prior). From $\ell \geq 800$ we find $\sigma_8 \Omega_m^{0.25} = 0.657 \pm 0.018$, which is higher than the *Planck* $\phi\phi$ constraint in equation (1) by 2.4σ, the same difference as for $\ell \geq 1000$. We conclude that the particular choice of $\ell = 1000$ is not driving our results.

2.4 Discussion

We have found multiple similar tensions at the $> 2\sigma$ level between the *Planck* 2015 high-multipole TT power spectrum and a range of other measurements. In general such tensions could be due to: (i) statistical fluctuations, (ii) an incorrect cosmological model, or (iii) systematic errors or underestimation of statistical errors in the *Planck* spectrum. A combination of these factors is also possible.

If the tensions were largely due to an unlikely statistical fluctuation, our results suggest that it is parameters from the high-multipole *Planck* TT spectrum that have scattered unusually far from the underlying values, on the basis that the low-multipole *Planck* TT, *WMAP*, *Planck* $\phi\phi$, BAO and distance ladder H_0 measurements are all in reasonable agreement with one another (see also Bennett et al., 2014). One might argue that the $\ell < 1000$ *WMAP* and *Planck* constraints are pulled away from the true values by the multipoles at $\ell < 30$. However, all parameter constraints we have quoted include cosmic variance uncertainty and thus account for this possibility (assuming Gaussian fluctuations). Furthermore, an unusual statistical fluctuation in the $\ell < 1000$ values cannot explain the disagreement between the *Planck* $\ell \geq 1000$ constraints and SPT, *Planck* $\phi\phi$, BAO, and the distance ladder measurements.

Cosmology beyond standard ΛCDM cannot be ruled out as the dominant cause of tension. We do not favor this explanation because, firstly, none of the physically motivated modifications investigated by Planck Collaboration XIII (2016) were found to be significantly preferred in fits to the full *Planck* TT spectrum, and, secondly, the most precise measurements of the CMB damping

tail, from *Planck* and SPT, disagree, as discussed in Sections 2.3.2 and 2.3.3.

From 2013 to 2015 the *Planck* results were revised due to several significant systematic effects. Without more detailed reanalysis of the *Planck* 2015 data we are not in a position to comment on remaining sources of systematic error in the *Planck* high-multipole spectrum. We do note that the TT covariance matrices described in Planck Collaboration XIII (2016) were calculated analytically assuming that sky components are Gaussian. Both foregrounds and the primary CMB have known non-Gaussian characteristics (in the latter case due to lensing, see, e.g., Benoit-Lévy, Smith, and Hu, 2012) that would result in this approximation underestimating the true TT spectrum uncertainties, particularly at high multipoles where the foreground power becomes comparable to the CMB signal and the lensing effect is most important.

Finally, we emphasize that, irrespective of what is responsible for these tensions, care must clearly be taken when interpreting joint fits including the full range of *Planck* multipoles, particularly given *Planck*'s high precision and ability to statistically dominate other measurements, regardless of accuracy.

2.5 Conclusions

We have discussed tensions between the *Planck* 2015 high-multipole TT spectrum ($\ell \geq 1000$, roughly the scales inaccessible to *WMAP*) and the cosmological measurements:

- the *Planck* 2015 TT spectrum at $\ell < 1000$, which prefers a value of $\Omega_c h^2$ 2.5σ lower than the high-multipole fit,

- the *Planck* 2015 $\phi\phi$ lensing power spectrum, which has an amplitude (parametrized by $\sigma_8\Omega_m^{0.25}$) 2.4σ lower than predicted from the $\ell \geq 1000$ TT spectrum,
- the SPT TT spectrum, covering $650 \leq \ell \leq 3000$, which predicts, for example, a Hubble constant 2.7σ higher than *Planck* $\ell \geq 1000$,
- the most precise measurement of the BAO scale, from the BOSS CMASS galaxy sample at effective redshift $z = 0.57$, which disagrees at the 2.5σ level, and
- the most precise local distance ladder determination of H_0, which is in tension at the 3.0σ level.

These differences are quoted assuming $\tau = 0.07 \pm 0.02$. We found that some tensions are reduced by allowing larger values of τ but note that this would introduce new tension with *Planck* polarization data. Definitive conclusions about τ will require a more detailed understanding of low-ℓ foreground contamination. The Cosmology Large Angular Scale Surveyor (CLASS) is expected to provide a cosmic variance limited measurement of τ (**class:2014**; Watts et al., 2015).

Given these results and the previously reported tensions with some weak lensing and cluster abundance data, we suggest that the parameter constraints from the high-multipole *Planck* data appear anomalous due to either an unlikely statistical fluctuation, remaining systematic errors, or both. Understanding the origin of these discrepancies is important given the role *Planck* data

might play in future cosmological advances.

References

Abazajian, K. N., K. Arnold, J. Austermann, B. A. Benson, C. Bischoff, J. Bock, J. R. Bond, J. Borrill, I. Buder, D. L. Burke, E. Calabrese, J. E. Carlstrom, C. S. Carvalho, C. L. Chang, H. C. Chiang, S. Church, A. Cooray, T. M. Crawford, B. P. Crill, K. S. Dawson, S. Das, M. J. Devlin, M. Dobbs, S. Dodelson, O. Doré, J. Dunkley, J. L. Feng, A. Fraisse, J. Gallicchio, S. B. Giddings, D. Green, N. W. Halverson, S. Hanany, D. Hanson, S. R. Hildebrandt, A. Hincks, R. Hlozek, G. Holder, W. L. Holzapfel, K. Honscheid, G. Horowitz, W. Hu, J. Hubmayr, K. Irwin, M. Jackson, W. C. Jones, R. Kallosh, M. Kamionkowski, B. Keating, R. Keisler, W. Kinney, L. Knox, E. Komatsu, J. Kovac, C. L. Kuo, A. Kusaka, C. Lawrence, A. T. Lee, E. Leitch, A. Linde, E. Linder, P. Lubin, J. Maldacena, E. Martinec, J. McMahon, A. Miller, V. Mukhanov, L. Newburgh, M. D. Niemack, H. Nguyen, H. T. Nguyen, L. Page, C. Pryke, C. L. Reichardt, J. E. Ruhl, N. Sehgal, U. Seljak, L. Senatore, J. Sievers, E. Silverstein, A. Slosar, K. M. Smith, D. Spergel, S. T. Staggs, A. Stark, R. Stompor, A. G. Vieregg, G. Wang, S. Watson, E. J. Wollack, W. L. K. Wu, K. W. Yoon, O. Zahn, and M. Zaldarriaga (2015a). "Inflation physics from the cosmic microwave background and large scale structure". In: *Astroparticle Physics* 63, pp. 55–65. DOI: 10.1016/j.astropartphys.2014.05.013. arXiv: 1309.5381 [astro-ph.CO].

Abazajian, K. N., K. Arnold, J. Austermann, B. A. Benson, C. Bischoff, J. Bock, J. R. Bond, J. Borrill, E. Calabrese, J. E. Carlstrom, C. S. Carvalho, C. L. Chang, H. C. Chiang, S. Church, A. Cooray, T. M. Crawford, K. S. Dawson, S. Das, M. J. Devlin, M. Dobbs, S. Dodelson, O. Doré, J. Dunkley, J. Errard, A. Fraisse, J. Gallicchio, N. W. Halverson, S. Hanany, S. R. Hildebrandt, A. Hincks, R. Hlozek, G. Holder, W. L. Holzapfel, K. Honscheid, W. Hu, J. Hubmayr, K. Irwin, W. C. Jones, M. Kamionkowski, B. Keating, R. Keisler, L. Knox, E. Komatsu, J. Kovac, C. L. Kuo, C. Lawrence, A. T. Lee, E. Leitch, E. Linder, P. Lubin, J. McMahon, A. Miller, L. Newburgh, M. D. Niemack, H. Nguyen, H. T. Nguyen, L. Page, C. Pryke, C. L. Reichardt, J. E. Ruhl, N.

Sehgal, U. Seljak, J. Sievers, E. Silverstein, A. Slosar, K. M. Smith, D. Spergel, S. T. Staggs, A. Stark, R. Stompor, A. G. Vieregg, G. Wang, S. Watson, E. J. Wollack, W. L. K. Wu, K. W. Yoon, and O. Zahn (2015b). "Neutrino physics from the cosmic microwave background and large scale structure". In: *Astroparticle Physics* 63, pp. 66–80. DOI: 10.1016/j.astropartphys.2014.05.014. arXiv: 1309.5383 [astro-ph.CO].

Addison, G. E., G. Hinshaw, and M. Halpern (2013). "Cosmological constraints from baryon acoustic oscillations and clustering of large-scale structure". In: *MNRAS* 436.2, pp. 1674–1683. DOI: 10.1093/mnras/stt1687. arXiv: 1304.6984 [astro-ph.CO].

Anderson, Lauren, Éric Aubourg, Stephen Bailey, Florian Beutler, Vaishali Bhardwaj, Michael Blanton, Adam S. Bolton, J. Brinkmann, Joel R. Brownstein, Angela Burden, Chia-Hsun Chuang, Antonio J. Cuesta, Kyle S. Dawson, Daniel J. Eisenstein, Stephanie Escoffier, James E. Gunn, Hong Guo, Shirley Ho, Klaus Honscheid, Cullan Howlett, David Kirkby, Robert H. Lupton, Marc Manera, Claudia Maraston, Cameron K. McBride, Olga Mena, Francesco Montesano, Robert C. Nichol, Sebastián E. Nuza, Matthew D. Olmstead, Nikhil Padmanabhan, Nathalie Palanque-Delabrouille, John Parejko, Will J. Percival, Patrick Petitjean, Francisco Prada, Adrian M. Price-Whelan, Beth Reid, Natalie A. Roe, Ashley J. Ross, Nicholas P. Ross, Cristiano G. Sabiu, Shun Saito, Lado Samushia, Ariel G. Sánchez, David J. Schlegel, Donald P. Schneider, Claudia G. Scoccola, Hee-Jong Seo, Ramin A. Skibba, Michael A. Strauss, Molly E. C. Swanson, Daniel Thomas, Jeremy L. Tinker, Rita Tojeiro, Mariana Vargas Magaña, Licia Verde, David A. Wake, Benjamin A. Weaver, David H. Weinberg, Martin White, Xiaoying Xu, Christophe Yèche, Idit Zehavi, and Gong-Bo Zhao (2014). "The clustering of galaxies in the SDSS-III Baryon Oscillation Spectroscopic Survey: baryon acoustic oscillations in the Data Releases 10 and 11 Galaxy samples". In: *MNRAS* 441.1, pp. 24–62. DOI: 10.1093/mnras/stu523. arXiv: 1312.4877 [astro-ph.CO].

Bennett, C. L., D. Larson, J. L. Weiland, and G. Hinshaw (2014). "The 1% Concordance Hubble Constant". In: *APJ* 794.2, 135, p. 135. DOI: 10.1088/0004-637X/794/2/135. arXiv: 1406.1718 [astro-ph.CO].

Bennett, C. L., D. Larson, J. L. Weiland, N. Jarosik, G. Hinshaw, N. Odegard, K. M. Smith, R. S. Hill, B. Gold, M. Halpern, E. Komatsu, M. R. Nolta, L. Page, D. N. Spergel, E. Wollack, J. Dunkley, A. Kogut, M. Limon, S. S. Meyer, G. S. Tucker, and E. L. Wright (2013). "Nine-year Wilkinson Microwave Anisotropy Probe (WMAP) Observations: Final Maps and

Results". In: *APJS* 208.2, 20, p. 20. DOI: 10.1088/0067-0049/208/2/20. arXiv: 1212.5225 [astro-ph.CO].

Benoit-Lévy, Aurélien, Kendrick M. Smith, and Wayne Hu (2012). "Non-Gaussian structure of the lensed CMB power spectra covariance matrix". In: *PRD* 86.12, 123008, p. 123008. DOI: 10.1103/PhysRevD.86.123008. arXiv: 1205.0474 [astro-ph.CO].

Beutler, Florian, Chris Blake, Matthew Colless, D. Heath Jones, Lister Staveley-Smith, Lachlan Campbell, Quentin Parker, Will Saunders, and Fred Watson (2011). "The 6dF Galaxy Survey: baryon acoustic oscillations and the local Hubble constant". In: *MNRAS* 416.4, pp. 3017–3032. DOI: 10.1111/j.1365-2966.2011.19250.x. arXiv: 1106.3366 [astro-ph.CO].

Calabrese, Erminia, Renée A. Hlozek, Nick Battaglia, Elia S. Battistelli, J. Richard Bond, Jens Chluba, Devin Crichton, Sudeep Das, Mark J. Devlin, Joanna Dunkley, Rolando Dünner, Marzieh Farhang, Megan B. Gralla, Amir Hajian, Mark Halpern, Matthew Hasselfield, Adam D. Hincks, Kent D. Irwin, Arthur Kosowsky, Thibaut Louis, Tobias A. Marriage, Kavilan Moodley, Laura Newburgh, Michael D. Niemack, Michael R. Nolta, Lyman A. Page, Neelima Sehgal, Blake D. Sherwin, Jonathan L. Sievers, Cristóbal Sifón, David N. Spergel, Suzanne T. Staggs, Eric R. Switzer, and Edward J. Wollack (2013). "Cosmological parameters from pre-planck cosmic microwave background measurements". In: *PRD* 87.10, 103012, p. 103012. DOI: 10.1103/PhysRevD.87.103012. arXiv: 1302.1841 [astro-ph.CO].

Calabrese, Erminia, An že Slosar, Alessandro Melchiorri, George F. Smoot, and Oliver Zahn (2008). "Cosmic microwave weak lensing data as a test for the dark universe". In: *Phys. Rev. D* 77 (12), p. 123531. DOI: 10.1103/PhysRevD.77.123531. URL: https://link.aps.org/doi/10.1103/PhysRevD.77.123531.

Eisenstein, Daniel J., Idit Zehavi, David W. Hogg, Roman Scoccimarro, Michael R. Blanton, Robert C. Nichol, Ryan Scranton, Hee-Jong Seo, Max Tegmark, Zheng Zheng, Scott F. Anderson, Jim Annis, Neta Bahcall, Jon Brinkmann, Scott Burles, Francisco J. Castand er, Andrew Connolly, Istvan Csabai, Mamoru Doi, Masataka Fukugita, Joshua A. Frieman, Karl Glazebrook, James E. Gunn, John S. Hendry, Gregory Hennessy, Zeljko Ivezić, Stephen Kent, Gillian R. Knapp, Huan Lin, Yeong-Shang Loh, Robert H. Lupton, Bruce Margon, Timothy A. McKay, Avery Meiksin, Jeffery A. Munn, Adrian Pope, Michael W. Richmond, David Schlegel, Donald P. Schneider, Kazuhiro Shimasaku, Christopher Stoughton, Michael A. Strauss, Mark SubbaRao, Alexander S. Szalay, István Szapudi, Douglas L. Tucker, Brian

Yanny, and Donald G. York (2005). "Detection of the Baryon Acoustic Peak in the Large-Scale Correlation Function of SDSS Luminous Red Galaxies". In: *APJ* 633.2, pp. 560–574. DOI: 10.1086/466512. arXiv: astro-ph/0501171 [astro-ph].

Fendt, William A. and Benjamin D. Wandelt (2007). "Pico: Parameters for the Impatient Cosmologist". In: *APJ* 654.1, pp. 2–11. DOI: 10.1086/508342. arXiv: astro-ph/0606709 [astro-ph].

Heymans, Catherine, Ludovic Van Waerbeke, Lance Miller, Thomas Erben, Hendrik Hildebrandt, Henk Hoekstra, Thomas D. Kitching, Yannick Mellier, Patrick Simon, Christopher Bonnett, Jean Coupon, Liping Fu, Joachim Harnois Déraps, Michael J. Hudson, Martin Kilbinger, Koenraad Kuijken, Barnaby Rowe, Tim Schrabback, Elisabetta Semboloni, Edo van Uitert, Sanaz Vafaei, and Malin Velander (2012). "CFHTLenS: the Canada-France-Hawaii Telescope Lensing Survey". In: *MNRAS* 427.1, pp. 146–166. DOI: 10.1111/j.1365-2966.2012.21952.x. arXiv: 1210.0032 [astro-ph.CO].

Hinshaw, G., D. Larson, E. Komatsu, D. N. Spergel, C. L. Bennett, J. Dunkley, M. R. Nolta, M. Halpern, R. S. Hill, N. Odegard, L. Page, K. M. Smith, J. L. Weiland, B. Gold, N. Jarosik, A. Kogut, M. Limon, S. S. Meyer, G. S. Tucker, E. Wollack, and E. L. Wright (2013). "Nine-year Wilkinson Microwave Anisotropy Probe (WMAP) Observations: Cosmological Parameter Results". In: *APJS* 208.2, 19, p. 19. DOI: 10.1088/0067-0049/208/2/19. arXiv: 1212.5226 [astro-ph.CO].

Kim, A. G., N. Padmanabhan, G. Aldering, S. W. Allen, C. Baltay, R. N. Cahn, C. B. D'Andrea, N. Dalal, K. S. Dawson, K. D. Denney, D. J. Eisenstein, D. A. Finley, W. L. Freedman, S. Ho, D. E. Holz, D. Kasen, S. M. Kent, R. Kessler, S. Kuhlmann, E. V. Linder, P. Martini, P. E. Nugent, S. Perlmutter, B. M. Peterson, A. G. Riess, D. Rubin, M. Sako, N. V. Suntzeff, N. Suzuki, R. C. Thomas, W. M. Wood-Vasey, and S. E. Woosley (2015). "Distance probes of dark energy". In: *Astroparticle Physics* 63, pp. 2–22. DOI: 10.1016/j.astropartphys.2014.05.007. arXiv: 1309.5382 [astro-ph.CO].

Larson, D., J. L. Weiland, G. Hinshaw, and C. L. Bennett (2015). "Comparing Planck and WMAP: Maps, Spectra, and Parameters". In: *APJ* 801.1, 9, p. 9. DOI: 10.1088/0004-637X/801/1/9. arXiv: 1409.7718 [astro-ph.CO].

Lewis, Antony and Sarah Bridle (2002). "Cosmological parameters from CMB and other data: A Monte Carlo approach". In: *PRD* 66.10, 103511, p. 103511. DOI: 10.1103/PhysRevD.66.103511. arXiv: astro-ph/0205436 [astro-ph].

Lewis, Antony, Anthony Challinor, and Anthony Lasenby (2000). "Efficient Computation of Cosmic Microwave Background Anisotropies in Closed Friedmann-Robertson-Walker Models". In: *APJ* 538.2, pp. 473–476. DOI: 10.1086/309179. arXiv: astro-ph/9911177 [astro-ph].

Louis, Thibaut, Graeme E. Addison, Matthew Hasselfield, J. Richard Bond, Erminia Calabrese, Sudeep Das, Mark J. Devlin, Joanna Dunkley, Rolando Dünner, Megan Gralla, Amir Hajian, Adam D. Hincks, Renée Hlozek, Kevin Huffenberger, Leopoldo Infante, Arthur Kosowsky, Tobias A. Marriage, Kavilan Moodley, Sigurd Næss, Michael D. Niemack, Michael R. Nolta, Lyman A. Page, Bruce Partridge, Neelima Sehgal, Jonathan L. Sievers, David N. Spergel, Suzanne T. Staggs, Benjamin Z. Walter, and Edward J. Wollack (2014). "The Atacama Cosmology Telescope: cross correlation with Planck maps". In: *JCAP* 2014.7, 016, p. 016. DOI: 10.1088/1475-7516/2014/07/016. arXiv: 1403.0608 [astro-ph.CO].

Planck Collaboration (2014). "Planck 2013 results. XII. Diffuse component separation". In: *AAP* 571, A12, A12. DOI: 10.1051/0004-6361/201321580. arXiv: 1303.5072 [astro-ph.CO].

Planck Collaboration (2016a). "Planck 2015 results. I. Overview of products and scientific results". In: *AAP* 594, A1, A1. DOI: 10.1051/0004-6361/201527101. arXiv: 1502.01582 [astro-ph.CO].

Planck Collaboration (2016b). "Planck 2015 results. XXIV. Cosmology from Sunyaev-Zeldovich cluster counts". In: *AAP* 594, A24, A24. DOI: 10.1051/0004-6361/201525833. arXiv: 1502.01597 [astro-ph.CO].

Planck Collaboration XI (2016). "Planck 2015 results. XI. CMB power spectra, likelihoods, and robustness of parameters". In: *AAP* 594, A11, A11. DOI: 10.1051/0004-6361/201526926. arXiv: 1507.02704.

Planck Collaboration XIII (2016). "Planck 2015 results. XIII. Cosmological parameters". In: *AAP* 594, A13, A13. DOI: 10.1051/0004-6361/201525830. arXiv: 1502.01589.

Planck Collaboration XVI (2014). "Planck 2013 results. XVI. Cosmological parameters". In: *AAP* 571, A16, A16. DOI: 10.1051/0004-6361/201321591. arXiv: 1303.5076.

Planck XV, P. A. R. Ade, N. Aghanim, M. Arnaud, M. Ashdown, J. Aumont, C. Baccigalupi, A. J. Banday, R. B. Barreiro, J. G. Bartlett, and et al. (2015). "Planck 2015 results. XV. Gravitational lensing". In: *ArXiv e-prints*. arXiv: 1502.01591.

Riess, Adam G., Lucas Macri, Stefano Casertano, Hubert Lampeitl, Henry C. Ferguson, Alexei V. Filippenko, Saurabh W. Jha, Weidong Li, and Ryan

Chornock (2011). "A 3% Solution: Determination of the Hubble Constant with the Hubble Space Telescope and Wide Field Camera 3". In: *APJ* 730.2, 119, p. 119. DOI: 10.1088/0004-637X/730/2/119. arXiv: 1103.2976 [astro-ph.CO].

Ross, Ashley J., Lado Samushia, Cullan Howlett, Will J. Percival, Angela Burden, and Marc Manera (2015). "The clustering of the SDSS DR7 main Galaxy sample - I. A 4 per cent distance measure at z = 0.15". In: *MNRAS* 449.1, pp. 835–847. DOI: 10.1093/mnras/stv154. arXiv: 1409.3242 [astro-ph.CO].

Sievers, Jonathan L., Renée A. Hlozek, Michael R. Nolta, Viviana Acquaviva, Graeme E. Addison, Peter A. R. Ade, Paula Aguirre, Mandana Amiri, John William Appel, L. Felipe Barrientos, Elia S. Battistelli, Nick Battaglia, J. Richard Bond, Ben Brown, Bryce Burger, Erminia Calabrese, Jay Chervenak, Devin Crichton, Sudeep Das, Mark J. Devlin, Simon R. Dicker, W. Bertrand Doriese, Joanna Dunkley, Rolando Dünner, Thomas Essinger-Hileman, David Faber, Ryan P. Fisher, Joseph W. Fowler, Patricio Gallardo, Michael S. Gordon, Megan B. Gralla, Amir Hajian, Mark Halpern, Matthew Hasselfield, Carlos Hernández-Monteagudo, J. Colin Hill, Gene C. Hilton, Matt Hilton, Adam D. Hincks, Dave Holtz, Kevin M. Huffenberger, David H. Hughes, John P. Hughes, Leopoldo Infante, Kent D. Irwin, David R. Jacobson, Brittany Johnstone, Jean Baptiste Juin, Madhuri Kaul, Jeff Klein, Arthur Kosowsky, Judy M. Lau, Michele Limon, Yen-Ting Lin, Thibaut Louis, Robert H. Lupton, Tobias A. Marriage, Danica Marsden, Krista Martocci, Phil Mauskopf, Michael McLaren, Felipe Menanteau, Kavilan Moodley, Harvey Moseley, Calvin B. Netterfield, Michael D. Niemack, Lyman A. Page, William A. Page, Lucas Parker, Bruce Partridge, Reed Plimpton, Hernan Quintana, Erik D. Reese, Beth Reid, Felipe Rojas, Neelima Sehgal, Blake D. Sherwin, Benjamin L. Schmitt, David N. Spergel, Suzanne T. Staggs, Omelan Stryzak, Daniel S. Swetz, Eric R. Switzer, Robert Thornton, Hy Trac, Carole Tucker, Masao Uehara, Katerina Visnjic, Ryan Warne, Grant Wilson, Ed Wollack, Yue Zhao, and Caroline Zunckel (2013). "The Atacama Cosmology Telescope: cosmological parameters from three seasons of data". In: *JCAP* 2013.10, 060, p. 060. DOI: 10.1088/1475-7516/2013/10/060. arXiv: 1301.0824 [astro-ph.CO].

Spergel, David N., Raphael Flauger, and Renée Hložek (2015). "Planck data reconsidered". In: *PRD* 91.2, 023518, p. 023518. DOI: 10.1103/PhysRevD.91.023518. arXiv: 1312.3313 [astro-ph.CO].

Story, K. T., C. L. Reichardt, Z. Hou, R. Keisler, K. A. Aird, B. A. Benson, L. E. Bleem, J. E. Carlstrom, C. L. Chang, H. M. Cho, T. M. Crawford, A. T. Crites, T. de Haan, M. A. Dobbs, J. Dudley, B. Follin, E. M. George, N. W. Halverson, G. P. Holder, W. L. Holzapfel, S. Hoover, J. D. Hrubes, M. Joy, L. Knox, A. T. Lee, E. M. Leitch, M. Lueker, D. Luong-Van, J. J. McMahon, J. Mehl, S. S. Meyer, M. Millea, J. J. Mohr, T. E. Montroy, S. Padin, T. Plagge, C. Pryke, J. E. Ruhl, J. T. Sayre, K. K. Schaffer, L. Shaw, E. Shirokoff, H. G. Spieler, Z. Staniszewski, A. A. Stark, A. van Engelen, K. Vand erlinde, J. D. Vieira, R. Williamson, and O. Zahn (2013). "A Measurement of the Cosmic Microwave Background Damping Tail from the 2500-Square-Degree SPT-SZ Survey". In: *APJ* 779.1, 86, p. 86. DOI: 10.1088/0004-637X/779/1/86. arXiv: 1210.7231 [astro-ph.CO].

Watts, Duncan J., David Larson, Tobias A. Marriage, Maximilian H. Abitbol, John W. Appel, Charles L. Bennett, David T. Chuss, Joseph R. Eimer, Thomas Essinger-Hileman, Nathan J. Miller, Karwan Rostem, and Edward J. Wollack (2015). "Measuring the Largest Angular Scale CMB B-mode Polarization with Galactic Foregrounds on a Cut Sky". In: *APJ* 814.2, 103, p. 103. DOI: 10.1088/0004-637X/814/2/103. arXiv: 1508.00017 [astro-ph.CO].

Chapter 3

Assessing Consistency Between *WMAP* 9-year and *Planck* 2015 Temperature Power Spectra

This chapter is taken from Huang et al. 2018 (*APJ 869, 38, p. 38*), where we perform a comparison of *WMAP* 9-year (*WMAP*9) and *Planck* 2015 cosmic microwave background (CMB) temperature power spectra across multipoles $30 \leq \ell \leq 1200$. We generate simulations to estimate the correlation between the two datasets due to cosmic variance from observing the same sky. We find that their spectra are consistent within 1σ. We also show that changing the fiducial power spectrum for simulations only impacts the comparison at around 0.1σ level. The consistency shown in our analysis provides high confidence in both the *WMAP*9 temperature power spectrum and the overlapping multipole region of *Planck* 2015's, virtually independent of any assumed cosmological model. Our results indicate that cosmological model differences between *Planck* and *WMAP* do not arise from measurement differences, but from the high multipoles not measured by *WMAP*.

3.1 Introduction

Observations of CMB temperature anisotropy and its power spectrum (hereafter TT spectrum) have provided great insight into early universe physics and enabled precise constraints on cosmological parameters, within the context of the Λ cold dark matter (ΛCDM) model (e.g., Bennett et al., 2013; Planck Collaboration, 2016c; Sievers et al., 2013; Story et al., 2013). The importance of the determination of cosmological parameters goes beyond studies involving the CMB. The choice of which CMB data set to use can meaningfully impact results from dark matter or hydrodynamic simulations, with implications for constraints on neutrino mass and alternative gravity models (e.g., Hojjati et al., 2015; McCarthy et al., 2018; Planck Collaboration, 2016d).

In recent years, tensions have been shown to exist between CMB and several low-redshift, late time observations as well as within CMB measurements. For example, the most recent constraint on the Hubble constant, H_0, from Riess et al., 2018 yielded a value 3.7σ higher than that from *Planck* 2015 (Planck Collaboration, 2016e). Moreover, a $2-3\sigma$ difference was shown between *Planck* 2015 and measurements of weak gravitational lensing (e.g., Joudaki et al., 2018; Köhlinger et al., 2017), concerning the parameter combination S_8[1], which describes the growth of cosmic structure. In addition, a 2.5σ discordance has been reported between the *Planck* 2015 $\ell < 1000$ and $1000 \leq \ell \leq 2508$ data in $\Omega_c h^2$, the cold dark matter density, which is a parameter highly correlated with those constrained by low-redshift measurement (Addison et al., 2016).

[1] $S_8 \equiv \sigma_8(\Omega_m/0.3)^{0.5}$, where σ_8 is the present day amplitude of the matter fluctuation spectrum and Ω_m is the present day matter density in units of the critical density.

However, using simulated *Planck*-like TT power spectra, Planck Collaboration, 2017 argued that these ℓ-range related shifts in parameters were not statistically significant across the full ΛCDM model space.

Given the importance of CMB constraints for current and future cosmology, and the existing tensions, it is crucial that CMB measurements are scrutinized. The two latest full-sky CMB surveys, *WMAP* (Bennett et al., 2013) and *Planck* (Planck Collaboration, 2016a), provide a valuable opportunity for consistency checks.

The difference between the *Planck* 2015 and *WMAP*9 spectra is within the *WMAP*9 uncertainties (Planck Collaboration, 2016b), and the value of each of the ΛCDM parameters is consistent within 1.5 times the *WMAP*9 uncertainty (Planck Collaboration, 2016a). However, we should note that the correlation between the two experiments is not negligible as they measure the same sky. Between the *WMAP*9 and the *Planck* 2013 release (Planck Collaboration, 2014b), Larson et al., 2015 found a $\sim 6\sigma$ parameter difference, with a minimal ΛCDM model assumed and the correlation between the two experiments accounted for. The *Planck* calibration was significantly revised in the 2015 release (Planck Collaboration, 2016), and this motivates revisiting the comparison with *WMAP*.

This chapter therefore investigates consistency between *WMAP*9 and *Planck* 2015 TT spectra and estimates their correlation using simulations. We examine the multipole range common to both experiments where power-spectrum based likelihoods are employed ($30 \leq \ell \leq 1200$). Only when their correlation is quantified, can we quantify their agreement/disagreement in a

meaningful sense. Unlike comparisons of parameters, comparisons of power spectra are minimally dependent on the assumed model. We will show in Section 3.4 that the choice of fiducial model used to generate simulated spectra and estimate covariance between *WMAP*9 and *Planck* 2015 has a negligible effect on our results. Thus discrepancies that appear between the power spectra would be an indication of experimental systematic errors, instead of evidence for physics beyond the standard model of cosmology.

We exclude the $\ell < 30$ region of the TT spectra from our analysis. Comparison of $\ell < 30$ spectra is complicated by the fact that the *Planck* 2015 results included *WMAP*9 data in a multifrequency fit. A different (pixel-based) likelihood and treatment of foregrounds is also required for these scales. The *Planck* 2015 and *WMAP*9 results for $\ell < 30$ are shown in Figure 2 of Planck Collaboration, 2016b and agree within a small fraction of the uncertainty for most of the multipoles. Differences due to imperfect noise or foreground modeling, or some other systematic error, could still exist. Given the size of the cosmic variance uncertainty at $\ell < 30$, however, it seems highly unlikely that they could meaningfully impact cosmological results.

Following the completion of this work, the *Planck* team has released their latest results (Planck Collaboration, 2018a). The 2015 and 2018 *Planck* TT spectra are in good agreement, as described in Section 3.6 of Planck Collaboration, 2018b. We therefore expect the level of consistency between *WMAP*9 and *Planck* 2018 to remain the same.

The outline of this paper is as follows. We describe our simulation procedures in Section 3.2 and test simulation fidelity in Section 3. We present

results in Section 3.4, followed by conclusions in Section 3.5.

3.2 Simulating TT Spectra and Covariance

Our goal is to quantify the consistency between the TT power spectra observed by *WMAP*9 and *Planck* 2015. Both teams provide estimates of their experiment's power spectrum $C_\ell - C_{\ell'}$ covariance matrices, however we also need the *WMAP*9 $\times$ *Planck* 2015 cross-covariance due to common cosmic variance. To estimate this we generated 4000 full-sky simulations of CMB temperature fluctuations. The outline of the simulation procedure is as follows.

1. Generate a set of spherical harmonic coefficients $a_{\ell m}$ using the sphtfunc.synalm routine in `Healpy`[2] from a fiducial TT power spectrum chosen to be the best-fit model from the $\ell \geq 30$ *WMAP*9 TT spectrum. See Table 3.1 for the cosmological parameters in this model. Unless otherwise noted, results shown come from this fiducial model. Table 3.1 also includes an alternative model, which is one from the $\ell \geq 30$ *Planck* 2015 TT spectrum. We will use the alternative model to test the stability of our results against different input, see Section 3.2.3 and Section 3.4. We also note that this is the only place where an assumed cosmological model comes in.

2. Multiply the $a_{\ell m}$ coefficients with the appropriate beam and pixel functions, then convert them into a CMB map using the sphtfunc.alm2map routine in `Healpy`.

[2] A Python implementation of `Healpix` (Górski et al., 2005), see https://healpy.readthedocs.io/en/latest/.

Parameter	*WMAP*9 TT	*Planck* 2015 TT
Fit ΛCDM parameters		
$\Omega_b h^2$	0.02230	0.02215
$\Omega_c h^2$	0.1158	0.1215
$100\theta_{MC}$	1.0393	1.0405
τ	0.07	0.07
$\log A_s$	3.059	3.078
n_s	0.9615	0.9595
Derived parameters		
H_0[km s^{-1}Mpc^{-1}]	68.24	66.52
Ω_m	0.2981	0.3261
σ_8	0.8007	0.8288

Table 3.1: Fiducial models
Here are the cosmological parameters describing the fiducial models used in our simulations. The second column shows the best-fit model from the $30 \leq \ell \leq 1200$ *WMAP*9 TT spectrum and the third that of the $30 \leq \ell \leq 2508$ *Planck* 2015 spectrum. They are both results of running the best-fit finding algorithm in CosmoMC (Lewis and Bridle, 2002) with τ fixed to be 0.07, together with the PICO code (Fendt and Wandelt, 2007), which computes CMB power spectra given the model.

3. Add to the map white noise with variance given by the experiments.

4. Apply sky masks and compute the TT spectrum from the masked maps using `PolSpice`[3] (Szapudi et al., 2001).

5. Compute analytically the power spectrum covariance (hereafter referred to as the analytic covariance), following the prescriptions given by Appendix C1.1.1 of Planck Collaboration, 2016b. The analytic calculations take into account the effects of masking, beam and pixel window functions, and the instrumental noise (Efstathiou, 2004). We will refer to this approach as "MASTER" (Hivon et al., 2002) to distinguish it from the alternative "C^{-1}" method used for *WMAP*9 (see Section 3.2.1).

6. Calculate the sample covariance of the simulated spectra (hereafter the simulated covariance).

7. To reduce the random fluctuations in the simulated covariance and the bias to its inverse matrix due to the finite number of simulations (Sellentin and Heavens, 2016), we apply the same binning scheme to the simulated spectra and covariance matrices (both the analytic and the simulated) as was applied in the published *Planck* 2015 likelihood code[4]. The number of bins that cover $30 \leq \ell \leq 1200$ is 136.

8. Calibrate the analytic covariance using the simulations, as described in Section 3.2.3. The calibrated matrix is referred to as the corrected analytic covariance, which we will be using for our final analysis. The

[3] http://www2.iap.fr/users/hivon/software/PolSpice/
[4] http://pla.esac.esa.int/pla/#cosmology

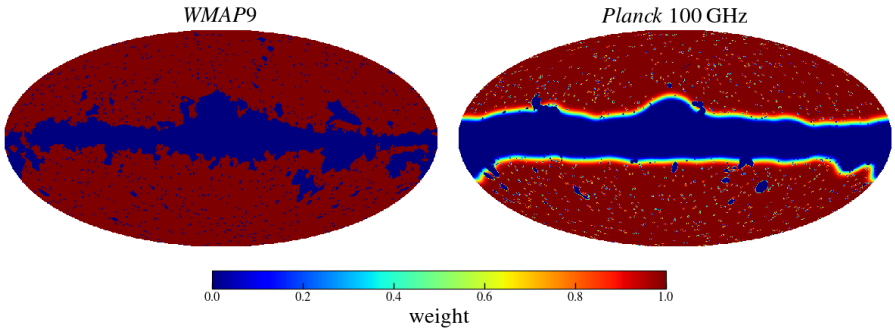

Figure 3.1: Temperature analysis mask

Left: the KQ85y9 temperature analysis mask used in the *WMAP*9 analysis (Bennett et al., 2013); right: the *Planck* 2015 T66 mask for 100 GHz (Planck Collaboration, 2016b). As shown, not all the areas chosen to be masked are the same. The unmasked fraction of the sky is 75% for *WMAP*9 and 66% for *Planck* 100 GHz. While the *WMAP*9 mask only has weights of 0 and 1, the *Planck* mask is apodized, with weights in between. The difference between *WMAP*9 and *Planck* 2015 sky masks is the reason that the *WMAP*9 and the *Planck* 2015 spectra are not fully correlated even at $\ell \leq 300$, where noise is negligible compared to cosmic variance uncertainty. See Section 3.2.3.

analytic covariance matrix underestimates the true covariance by up to 10% for some multipoles (see Section 3.6), and the simulations are used to correct for this.

9. With the binned corrected analytic covariance, we follow procedures described in Section 3.4 to derive the covariance of the difference between the observed *WMAP*9 and *Planck* 2015 TT spectra and test whether this difference is consistent with zero.

More details of the procedure are provided in the following subsections.

3.2.1 Simulating *WMAP*9 Spectra

The *WMAP* instrument was composed of 10 differencing assemblies (DAs) spanning five frequencies from 23 to 94 GHz (Bennett et al., 2003). The three lowest frequency bands are used as foreground monitors. Only the V band ($\sim$ 61 GHz) and the W band ($\sim$ 94 GHz) are used to compute the TT spectrum (Hinshaw et al., 2007). The beam widths for the V and the W band are 0.33° and 0.21° FWHM respectively. In the *WMAP* analysis, the $a_{\ell m}$ coefficients were computed from the `Healpix` $N_{\rm side}$ = 1024 (10 arcmin pixels) maps for each single year and each single-DA (V1, V2, W1-W4). For low multipoles ($2 \leq \ell < 30$) a pixel-based likelihood was used, while a power spectrum based likelihood was used for $30 \leq \ell \leq 1200$. Until the nine-year release of *WMAP* data, for $\ell \leq 600$ the coefficients were evaluated with uniform pixel weighting, which is optimal in the signal-dominated region, while inverse-noise weighting, optimal in the noise-dominated region, was used for $\ell > 600$ (Larson et al., 2011). The TT cross-power spectra are computed from all the pairs of independent maps. For *WMAP*9[5], a different power spectrum estimator, the C^{-1} method, was used (Bennett et al., 2013). However, it would be computationally challenging to implement C^{-1} on all our 4000 simulations. We will show in Section 3.4 that our results should not be affected significantly by the change of C_ℓ estimator. The *WMAP*9 analysis also took into account the uncertainties from the beam functions and point sources, but we exclude these because their effect is small (contributing about 0.06% of the $\ell > 30$ temperature log-likelihood) and is not expected to correlate with

[5]For the *WMAP*9 likelihood code, see https://lambda.gsfc.nasa.gov/product/map/current/likelihood_get.cfm.

Planck uncertainties.

Using the best-fit power spectrum of *WMAP*9 TT data with the reionization optical depth τ fixed to be 0.07 (see Table 3.1 for the model parameters), we generate 4000 realizations. At $30 \leq \ell \leq 1200$, τ is strongly degenerate with A_s, the amplitude of primordial density fluctuations, as the TT spectrum is only sensitive to the parameter combination $A_s e^{-2\tau}$. Fixing τ breaks the degeneracy, and the value 0.07 is also consistent with those inferred by *WMAP*9 and *Planck* 2015 data, being within 1.5σ of their constraints (see Table 1 of Weiland et al., 2018, for recently published values of τ from different choices of data sets).

To simulate the maps observed by each DA, we multiply the simulated spherical harmonics with the *WMAP*9 beam window function for that DA and add Gaussian noise. We make one noise map for each DA by inverting the sum of inverse variances from maps in different years. Then we apply the KQ85y9 temperature analysis mask (Bennett et al., 2013), which masks both galactic emission and bright point sources, leaving 75% of the sky to be analyzed, see Figure 3.1. Next we compute cross spectra for the six realistic maps with the appropriate pixel weighting applied to their corresponding range of multipoles.

3.2.2 Simulating *Planck* 2015 Spectra

The *Planck* instrument consists of seventy-four detectors in nine frequency bands between 30 and 857 GHz (Planck Collaboration, 2014a). Similarly to *WMAP*9, a pixel-based likelihood is used at $2 \leq \ell < 30$, and a power spectrum based likelihood is used for $30 \leq \ell \leq 2508$. For $\ell \geq 30$, TT spectra are

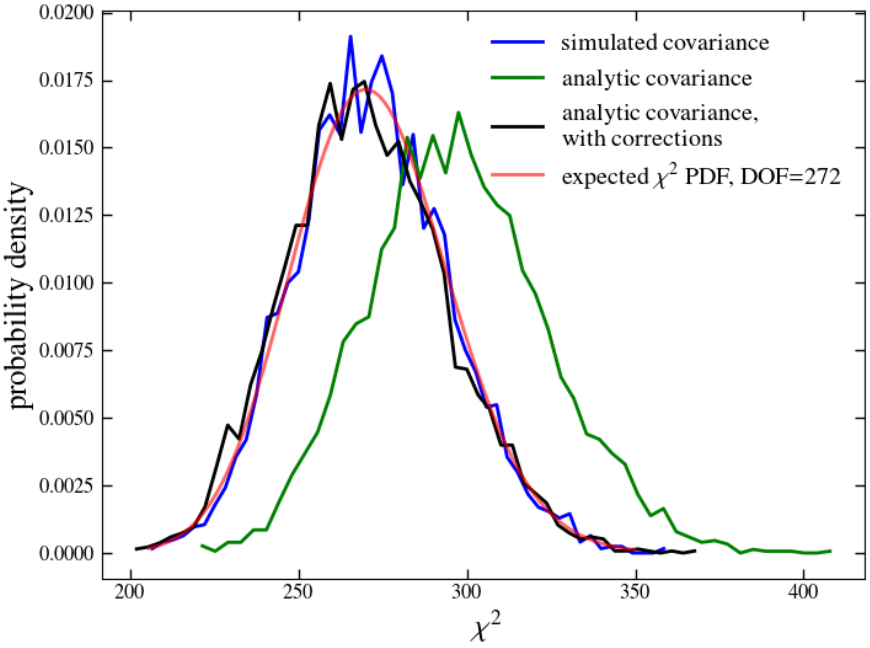

Figure 3.2: χ^2 distribution of binned spectra of *WMAP*9 and *Planck* 2015

Here shows the χ^2 distribution of 4000 simulated binned spectra of *WMAP*9 and *Planck* 2015, using different versions of binned covariance matrices. The analytic covariance (green) produces a χ^2 higher than expected, consistent with the fact that it underestimates the true covariance of the simulated spectra (see text and Section 3.6). The simulated covariance (blue) leads to a slightly narrower histogram, as the finite number of simulations introduces a slight bias into the inverse simulated covariance. The corrected analytic covariance (black) recovers the expected χ^2 probability density function (PDF), with 272 degrees of freedom (DOF). This indicates that the binned power spectrum is well approximated by a Gaussian distribution with the mean and the covariance matching the fiducial spectrum and the corrected analytic covariance matrix, respectively. Thus, for the subsequent analysis, we use the corrected analytic covariance matrix.

computed as cross-spectra between the first half-mission and the second half-mission maps of different detector combinations, in three frequency channels: 100 GHz, 143 GHz and 217 GHz. Their effective beam FWHM in arcmin are 9.68, 7.30 and 5.02 respectively (Planck Collaboration, 2016b). Different masks are applied to the half-mission maps for each frequency. The masks applied are T66, T57 and T47 for 100 GHz, 143 GHz and 217 GHz, respectively. See Figure 3.1 for the T66 mask of the 100 GHz temperature maps. The final power spectrum is an optimal combination of the 100×100 GHz, 143×143 GHz, 217×217 GHz and 143×217 GHz spectra.

The procedure of simulating *Planck* 2015 spectra is very similar to that of *WMAP*9, except we make use of the published *Planck* 2015 half-mission noise maps and simulate six CMB signal maps for the three frequencies mentioned above and their two half-missions. We include the effect of the published beam window functions and work at $N_{\rm side} = 2048$, corresponding to 5 arcmin pixels. We ignore the noise correlation between pixels (Planck Collaboration, 2016b), since the *Planck* and *WMAP* noise are independent and only enter the *WMAP*9 × *Planck* 2015 covariance matrix indirectly through the weighting of power spectra. Then we apply the masks for each frequency and obtain the cross spectra up to $\ell = 1200$ for the same four frequency combinations used in the experiment. We do not include *Planck* foregrounds in the simulations because the dominant Galactic and extragalactic dust foregrounds in the *Planck* channels are far smaller at the lower *WMAP* frequencies. We therefore do not expect foreground uncertainties to contribute significantly to the *WMAP*-*Planck* correlation.

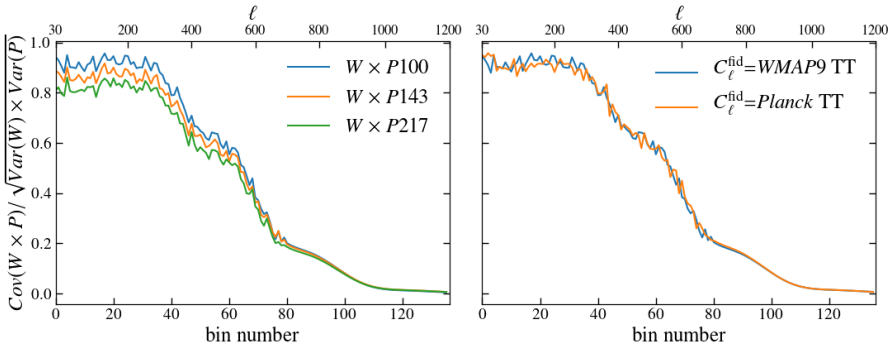

Figure 3.3: Correlation between *WMAP*9 (*W*) and *Planck* 2015 (*P*) binned TT power spectra

The correlation between *WMAP*9 (*W*) and *Planck* 2015 (*P*) binned TT power spectra, defined as the ratio of the diagonal elements of the corrected analytic covariance between the combined spectra, to the square root of the product of the experimental variances. The axis on the top shows the center multipole of each bin. The spiky structure in the first 80 bins is due to calibrating the analytic covariance using the simulations, which introduces small random fluctuations. Left: Comparison of the correlation between *WMAP*9 and different *Planck* 2015 frequency channels, with the *WMAP*9 best-fit spectrum as the fiducial spectrum. The *WMAP* mask uses 75% of the sky while the sky fractions of the masks for *Planck* 100, 143, and 217 GHz are 66%, 57%, and 47%, respectively. The correlation falls off at smaller scales as *WMAP* variance becomes dominated by noise. *Planck* masks with lower sky fraction produce lower correlation with *WMAP*9. Right: We also compare the correlation between the combined spectra using different fiducial models for simulations, the best-fit spectrum from *WMAP*9 $\ell \geq 30$ data, and *Planck* 2015 $\ell \geq 30$. In Section 3.4, we show that the choice of fiducial spectra makes a negligible difference.

3.2.3 Calculating Power Spectrum Covariance

We follow the procedure in Appendix C.1.1 of Planck Collaboration, 2016b applying the MASTER method (Efstathiou, 2004) to derive a full, analytic covariance for both experiments accounting for the effect of noise, window functions, masks and different map weighting schemes. The main idea of the procedure is that first we calculate the power spectrum of a masked map, then we perform mask deconvolution to recover an unbiased estimate of the true underlying spectrum. Next we bin both the simulated spectra and analytic covariance matrices, using the binning matrix B provided by the *Planck* 2015 likelihood code. The binned spectra and covariance are obtained from the following expressions:

$$C_b = \sum_{\ell} B_{b\ell} C_{\ell}, \tag{3.1}$$

$$\mathbf{\Sigma}_{XY,bb'} = \sum_{\ell,\ell'} B_{b\ell} \mathbf{\Sigma}_{XY,\ell\ell'} B^T_{\ell' b'} \tag{3.2}$$

where b runs over 136 bins and $\mathbf{\Sigma}$ is a covariance matrix. The subscripts X and Y are either W or P, referring to *WMAP*9 and *Planck* 2015 respectively. The measured/simulated C_ℓs are only approximately χ^2 distributed due to masking. With the large number of modes being combined into each bin, the C_bs can be well approximated as Gaussian (Planck Collaboration, 2016b).

We then co-add the spectra based on their inverse covariance to obtain one combined spectrum for *WMAP*9 and one for *Planck* 2015, as well as the covariance matrices for the combined spectra, following the steps in Appendix C of Hinshaw et al., 2003 and in Appendix C.4 of Planck Collaboration, 2016b

respectively.

As noted in Planck Collaboration, 2016b, the analytic covariance, though not subject to random fluctuations in the simulations, does not fully capture the covariance of the simulated power spectra. We believe the disagreement arises from an assumption made in the analytic calculation that there is negligible variation over a small range of multipoles in the power spectrum. This leads to underestimation around $\sim 10\%$ for signal dominated regions (see Section 3.6). To correct for such discrepancies, first we break down the covariance matrix $\mathbf{\Sigma}$ into 4 sub-blocks as

$$\mathbf{\Sigma} = \begin{pmatrix} \mathbf{\Sigma}_{WW} & \mathbf{\Sigma}_{WP} \\ \mathbf{\Sigma}_{PW} & \mathbf{\Sigma}_{PP} \end{pmatrix} \tag{3.3}$$

where each term is a 136×136 matrix, and 136 is the number of bins for $30 \leq \ell \leq 1200$. The elements $\mathbf{\Sigma}^{\rm ANA}_{XY,ij}$ in each sub-block of the analytic matrix are rescaled by the factor $r_i^2 = \mathbf{\Sigma}^{\rm SIM}_{XY,ii}/\mathbf{\Sigma}^{\rm ANA}_{XY,ii}$ which compares the simulated diagonal elements of one sub-block to the analytic. Then we rescale all the elements so that $\mathbf{\Sigma}^{\rm ANA,corrected}_{XY,ij} = \mathbf{\Sigma}^{\rm ANA}_{XY,ij} r_i r_j$. For the *WMAP-Planck* analytic covariance, the correction is applied only to the first 80 of 136 bins. For bin numbers over 80, the scatter in the simulated covariance due to the *WMAP* noise is much larger in magnitude than the analytic estimation.

Figure 3.2 shows the χ^2 distribution of 4000 simulated, binned and combined spectra of *WMAP*9 and *Planck* 2015, with 272 degrees of freedom. Here χ^2 is defined as

$$\chi^2 = \sum_{b,b'=1}^{272} (\hat{C}_b^{\rm SIM} - C_b^{\rm fid})(\mathbf{\Sigma}^{-1})_{bb'}(\hat{C}_{b'}^{\rm SIM} - C_{b'}^{\rm fid}) \tag{3.4}$$

where $C^{\rm fid}$ consists of two copies of the binned fiducial spectra and $\hat{C}^{\rm SIM} = (\hat{C}^{\rm SIM}_W, \hat{C}^{\rm SIM}_P)$ contains the simulated *WMAP* and *Planck* spectra. The different lines in Figure 3.2 show results with different choices of $\mathbf{\Sigma}$: the simulated, the analytic, or the analytic with corrections. For the subsequent analysis, we use the corrected analytic covariance matrix.

We show in Figure 3.3 the correlation between *WMAP*9 and *Planck* 2015 TT spectra, defined as the ratio of the diagonal elements of covariance between the two experiments, based on analytic calculation and calibrated by simulations, to the square root of the product of the experimental variances of *WMAP*9 and *Planck* 2015. The correlation falls from 0.8-0.9 at low multipoles, where both experiments are cosmic variance limited, to close to zero at higher multipoles, where*WMAP* variance is increasingly dominated by noise. The right panel of the figure shows that the correlation depends very weakly on the chosen fiducial spectrum.

3.3 Comparing Simulations to Experiments

To test whether our simulations capture experimental properties, we compare the corrected analytic variance of simulated power spectra to the ones published by the *WMAP* and *Planck* teams. Since we are only using the simulations and analytic calculations to estimate the cross-covariance between *WMAP* and *Planck*, the exact agreement for the $W \times W$ and the $P \times P$ covariance is not required. For *WMAP*9, the variance provided by the published likelihood code depends on the choice of the theory spectrum. We choose to use the best-fit power spectrum of *WMAP*9 TT data with a fixed τ, so as

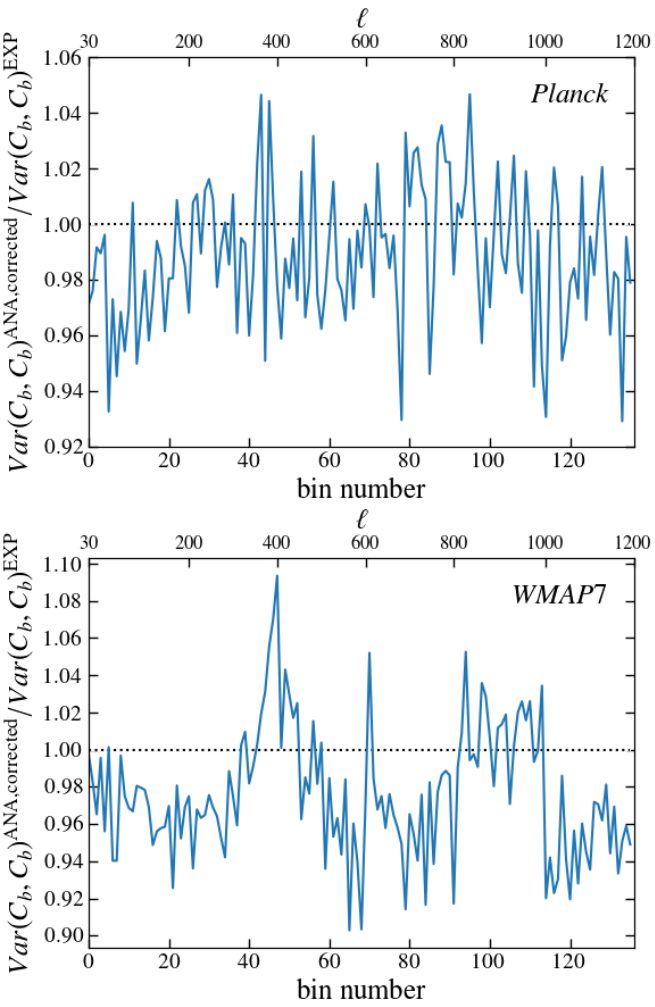

Figure 3.4: Ratio of the corrected analytic binned TT variance to the experimental variance

Here shows ratio of the corrected analytic binned TT variance to the experimental variance for *Planck* 2015 (top) and *WMAP*7 (bottom). We show the *WMAP*7 ratio instead of *WMAP*9 because both our simulations and *WMAP*7 use the MASTER power spectrum estimator, while *WMAP*9 uses the C^{-1} estimator. The deviations from unity are due to differences between our simulations and the analysis process of the experiments. The simulated *WMAP-WMAP* and *Planck-Planck* covariances are not used in our final consistency test. See text and Section 3.4 for discussion of implications for the *WMAP-Planck* covariance.

to be consistent with our simulations. On the other hand, the *Planck* 2015 published variance is based on a fixed fiducial spectrum fit to $\ell \geq 30$ with $\tau = 0.07 \pm 0.02$ (Section 3.3 of Planck Collaboration, 2016b). We therefore used our simulations generated with the *Planck* $\ell \geq 30$ best-fit model with $\tau = 0.07$ as input when comparing to the published variance. As mentioned earlier, the exact choice of τ is not important for $30 \leq \ell \leq 1200$.

For *Planck* 2015, the variance used as reference is a binned matrix obtained from co-adding the covariance of different cross spectra provided by the *Planck* 2015 released likelihood code, following procedures similar to co-adding the spectra, as mentioned in Section 3.2.3. The simulated/experimental (S/E) ratio, shown in the top panel of Figure 3.4, is on average slightly below 1. We believe this is due the fact that our simulations do not exactly replicate the *Planck* 2015 analysis process. We investigate the potential effect of this underestimation on the *WMAP-Planck* covariance in Section 3.4.

For *WMAP*9 the situation is more complicated. In the analysis of the nine-year data, the *WMAP* team replaced the MASTER power spectrum estimator by an optimal C^{-1} estimator. This estimator uses all the two-point correlation information in the unmasked pixels in the map, or, equivalently, the full covariance structure in the harmonics of the masked map, $\tilde{a}_{\ell m}$. Pseudo-C_ℓ methods like MASTER provide an unbiased estimate for the underlying power spectrum but only utilize products of $\tilde{a}_{\ell m}$ for the same ℓ and m (see Section 3.6), causing some loss of information (e.g., Gruetjen and Shellard, 2014). The published *WMAP*9 likelihood package does not include results analyzed using the MASTER method, so we generate another set of 4000 simulations with *WMAP*

seven-year (*WMAP*7) data properties and compare their spectrum variance to the result from inverting the Fisher matrix in the *WMAP*7 likelihood code. The bottom panel of Figure 3.4 shows the S/E ratio for *WMAP*7. Numerical differences exist between our analytic calculation using the MASTER method and the approximation used for the *WMAP*7 Fisher matrix, causing deviations from unity in the S/E ratio. This difference is unlikely to have any significant effect on our final results, because it is smaller than the difference between using the MASTER method and using the C^{-1} method and even that does not change our conclusion, as discussed below.

Going from MASTER method to C^{-1} reduces the power spectrum variance by 7-17% as shown in Figure 31 of Bennett et al., 2013. This means our simulations with MASTER overestimate the experimental variance of *WMAP*9. Fortunately, this should not impact the *WMAP-Planck* covariance, which is what we are using the simulations to obtain, because the *Planck* analysis used MASTER. The additional information about the C_ℓs gained from applying the C^{-1} estimator to *WMAP* maps is therefore not present in the *Planck* 2015 power spectra and should not lead to a reduction of the *WMAP-Planck* covariance.

In Section 3.4 we test this argument by investigating the effect of different pixel weightings of the *WMAP*9 temperature maps on the *WMAP-Planck* covariance. The different weighting schemes represent more extreme changes in the *WMAP*9 TT uncertainties than changing from MASTER to C^{-1}, but do not lead to changes to our conclusion about the consistency of the experiments.

$C_\ell^{\rm fid}$	*WMAP*9 Pixel Weighting	$\chi^2_{\rm diff}$	PTE
*WMAP*9	Hybrid	141.8	0.35
Planck 2015	Hybrid	139.6	0.40
*WMAP*9	Uniform	150.7	0.18
*WMAP*9	Inv Noise	139.4	0.40

Table 3.2: $\chi^2_{\rm diff}$ and PTE results for power spectrum differences

$\chi^2_{\rm diff}$ and PTE results for the observed power spectrum difference, with different fiducial input power spectra for simulations, and different weighting schemes for *WMAP*9 maps are shown here. The degree of freedom is 136. Three different weighting schemes are applied to the simulated *WMAP*9 temperature maps. Uniform is when all the pixels share the same weight. Inverse noise weighting weights the pixels by their inverse noise variance. Hybrid is using uniform weighting for $\ell \leq 600$ and inverse noise for $\ell > 600$. We find no significant difference in the values of $\chi^2_{\rm diff}$ and PTE, using different fiducial spectra or different weighting schemes. We conclude that there is no significant difference between the observed *WMAP*9 and *Planck* 2015 TT spectra over their common multipole range.

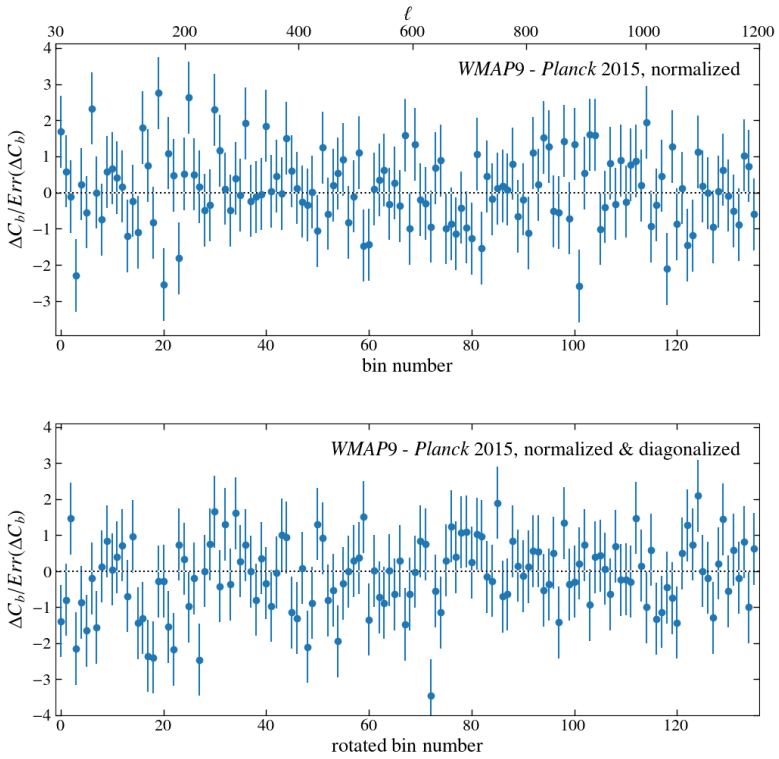

Figure 3.5: Power spectrum difference

Top: observed binned power spectrum difference between *WMAP*9 and *Planck* 2015, normalized by error bars estimated from simulations, which account for the correlated CMB cosmic variance between the two experiments. Most data points are within 2σ from zero. The first 13 bins are anti-correlated at $\sim$ 13% with their immediate neighbors, while the rest are at $\sim$ 5%. Bottom: the vector of differences is rotated so that its covariance is diagonalized and the bins are uncorrelated. The rotated difference shows no statistically significant deviation from zero, except for the 72nd bin. We do not consider it as a sign of inconsistency, because the probability of at least 1 out of 136 bins deviating more than 3σ from zero is 25%, for 136 independent Gaussian-distributed random variables. We note that similar “clumping" of adjacent points also appears in randomly generated sets of 136 Gaussian numbers.

3.4 Quantifying Consistency

To compare results from *WMAP*9 and *Planck* 2015, we need the power spectrum difference array ΔC_b and its associated covariance $\Delta\mathbf{\Sigma}$. The latter is given by

$$\Delta\mathbf{\Sigma} = \mathbf{\Sigma}_{WW} + \mathbf{\Sigma}_{PP} - \mathbf{\Sigma}_{WP} - \mathbf{\Sigma}_{PW} \tag{3.5}$$

and $\Delta C_b = C^{\rm OBS}_{W,b} - C^{\rm OBS}_{P,b}$ is the observed difference of binned power spectra in the common range of ℓ, provided by the two experiments. Then we calculate the χ^2 of the difference defined by

$$\chi^2_{\rm diff} = \sum_{b,b'=1}^{136} \Delta C_b^T \Delta\mathbf{\Sigma}^{-1}_{bb'} \Delta C_b \tag{3.6}$$

and its probability to exceed (PTE) for a χ^2 distribution with 136 degrees of freedom (the number of bins). Finally we convert the PTE values to an equivalent number of Gaussian standard deviations.

For $\mathbf{\Sigma}_{PP}$, we bin and co-add the covariance matrices for the 4 frequency combinations provided by the *Planck* 2015 likelihood code while $\mathbf{\Sigma}_{WW}$ is from inverting the Fisher matrix calculated from the *WMAP*9 likelihood code. For $\mathbf{\Sigma}_{WP}$ and $\mathbf{\Sigma}_{PW}$ we use the corrected analytic $W \times P$ and $P \times W$ covariance matrices described in Section 3.2.3.

The $\chi^2_{\rm diff}$ and PTE of the observed power spectrum difference are shown in Table 3.2. Using different input fiducial spectra or different pixel weighting schemes on simulated *WMAP*9 temperature maps does not change the values of $\chi^2_{\rm diff}$ or PTE significantly. The cases closest to the actual experiments are the ones using hybrid weighting for simulated *WMAP*9 maps. Using the

*WMAP*9 best-fit TT spectrum as the fiducial gives PTE 0.35, which means the *Planck* 2015 observed TT spectrum differs from *WMAP*9 at only 0.39σ, while using *Planck* 2015 best-fit spectrum as fiducial gives PTE 0.40, corresponding to a 0.26σ difference. This leads to the conclusion that there is no significant difference between the observed *WMAP*9 and *Planck* 2015 TT spectra over their common multipole range ($30 \leq \ell \leq 1200$), regardless of the choice of assumed models. Choosing a fiducial model with more drastically different cosmological parameters could have a larger impact on the *WMAP-Planck* consistency, however there is no motivation to consider such a model as it would provide a poor fit to the actual *WMAP* or *Planck* TT measurements.

Using different weightings on simulated *WMAP*9 maps does not change our conclusion. We test the extreme case of comparing results between using uniform weighting for all ℓ and using inverse noise weighting for all ℓ. The PTE value shifts from 0.18 to 0.40, corresponding to 0.91σ and 0.25σ respectively. The stability of our results against the change of map weighting schemes implies that our conclusion about the consistency between *WMAP*9 and *Planck* 2015 TT spectra would not change even if we were to generate simulations using the C^{-1} pipeline as the *WMAP* team did.

We test that the slight underestimation of experimental variances shown in Figure 3.4 would make no significant difference to our results, even if this also affects the *WMAP-Planck* covariance. Using the *WMAP*9 best-fit TT spectrum as the fiducial input and hybrid pixel weightings on simulated *WMAP* maps, rescaling the *WMAP-Planck* covariance by a factor of $(1.011 \times 1.024)^{0.5}$, which approximately compensates the underestimation, produces $\chi^2_{\rm diff} = 144.3$ and

PTE 0.30, corresponding to a 0.53σ difference.

The top of Figure 3.5 illustrates the observed power spectrum differences of binned power spectrum ΔC_b, with error bars given by $\Delta\mathbf{\Sigma}$ accounting for the correlated cosmic variance between *WMAP*9 and *Planck* 2015. To facilitate visual comparison, we divide the differences by their uncertainties, so that all the error bars are unity. As shown in this figure, the observed difference is roughly consistent with zero. Small correlations between adjacent bins ($\sim -13\%$ for the first 13 bins and $\sim -5\%$ for the rest) are accounted for when calculating $\chi^2_{\rm diff}$ but make visual assessment of ΔC_b more difficult. We therefore apply a rotation to the vector of differences so that its covariance is diagonalized and the bins are uncorrelated. The rotation matrix $\mathbf{U}$ is constructed from the eigenvectors of $\Delta\mathbf{\Sigma}$. The rotated vector of difference ΔC^R and its covariance $\Delta\mathbf{\Sigma}^R$ are given by the following:

$$\Delta C^R = \mathbf{U}^{-1}\Delta C \tag{3.7}$$

$$\Delta\mathbf{\Sigma}^R = \mathbf{U}^{-1}\Delta\mathbf{\Sigma}\mathbf{U} \tag{3.8}$$

The resulting normalized difference is shown in the bottom of Figure 3.5, showing no statistically significant deviation from zero, except for the 72nd bin. Assuming all the uncorrelated bins are Gaussian distributed, the probability of at least 1 out of 136 bins deviating more than 3σ from zero is 25%. Therefore we do not take this as a sign of inconsistency. Moreover, we do not think the apparent "clumping" of data points is anything more than statistical fluctuations. Human eyes are naturally drawn to patterns and thus tend to discover "features". An example test for the occurrence of clumping

is to ask whether the maximum number of consecutive points lying above or below zero (8 for the bottom panel of Figure 3.5, see the 16th to 23rd bins) is unusually high. We generated 10000 sets of 136 independent normally distributed values and found that 23.1% included 8 or more consecutive points lying above or below zero, indicating that the behavior in Figure 3.5 is consistent with statistical fluctuations.

In addition to the full $30 \leq \ell \leq 1200$ range we also calculated the χ^2 and PTE from different subsets of multipoles, including varying the maximum multipole. The PTE values from these tests were largely between 0.05 and 0.4, however we found that restricting the comparison to, for example, $30 \leq \ell \leq 200$ (up to bin 26), or $30 \leq \ell \leq 300$ (bin 37), produced lower PTE values of 0.005 and 0.012. Of our 4000 simulated *WMAP* and *Planck* spectra, 400 (10.0%) produce PTE values less than 0.01 as the maximum multipole was varied, and 491 (12.3%) produced values greater than 0.99. Restricting to the 373 realizations with PTE between 0.3 and 0.4 for $30 \leq \ell \leq 1200$, similar to the data value of 0.35, the corresponding numbers are 26 (7.0%) for PTE values less than 0.01 and 22 (5.9%) for greater than 0.99. The data therefore do not appear particularly anomalous in this respect.

3.5 Conclusions

We quantify the consistency between the observed TT power spectra from *WMAP*9 and *Planck* 2015 over their overlapping multipole range where power spectrum based likelihoods were used. We generated simulations to account for the cosmic variance common to both experiments. Their correlation is

estimated to be as high as $\sim 90\%$ in signal-dominated regions (roughly $\ell < 300$), and drops below 10% roughly at $\ell > 850$. Even taking into account their correlation, we find that the spectra are consistent within 1σ. We also note that with the common cosmic variance taken out of the covariance of the power spectrum difference between the two experiments, the consistency test presented in Section 3.4 is more sensitive to any unknown systematics or underestimated *WMAP* noise, than any test that can be done with each experiment alone.

We also tested our simulation fidelity in Section 3.2 and 3. We find that our simulated power spectra are consistently Gaussian distributed, with the mean being the input fiducial spectrum and the covariance properly estimated.

While we did not implement the optimal C^{-1} estimator on simulated *WMAP* maps as in the *WMAP*9 analysis, we tested the impact of pixel weighting on the *WMAP-Planck* covariance from adopting two extreme weighting schemes. We found that using either uniform weighting at all multipoles, or inverse-noise weighting at all multipoles, still resulted in agreement with *Planck* within 0.91σ. The different weightings mainly affect the *WMAP* noise contribution, which does not enter into the *WMAP-Planck* covariance. We also demonstrated the stability of our results against the choice of fiducial spectrum used in the simulations. Using the best-fit spectrum of the *Planck* 2015 TT data instead of that of *WMAP*9 only impacts the comparison at around 0.1σ.

The consistency shown in our analysis provides high confidence in both the *WMAP*9 temperature power spectrum and the overlapping multipole region

of the *Planck* 2015 power spectrum, virtually independent of any assumed cosmological model. The *Planck* 2018 TT spectrum is only minimally different from the 2015 version (Planck Collaboration, 2018b), and we therefore expect it to remain consistent with *WMAP*.

The difference between cosmological constraints from *WMAP* and *Planck* TT spectra is driven by higher multipoles in *Planck*, which also drive the tensions with some astrophysical data discussed earlier. An important check of these *Planck* measurements will come from similar tests to those performed in this work using temperature and polarization measurements from high-resolution experiments (e.g., Louis et al., 2014; Hou et al., 2018).

3.6 Appendix: Underestimation of Variance Due to Assumptions in Analytic Calculations

In this appendix, we discuss why the covariance obtained from analytic calculations based on the MASTER method underestimates the simulated one. This is also noted in Appendix C.1.4 of Planck Collaboration, 2016b. The upper panel of Figure 3.6 shows an example of the ratio of the analytic to the simulated variance, calculated from noise free simulations.

Limiting ourselves to the noiseless case, we look at a few key equations in the MASTER method and point out when the approximation is made and how it affects the result of the calculation. For a detailed description of the method, see Efstathiou, 2004.

The spherical harmonic transform of a temperature map ΔT_i with mask w_i

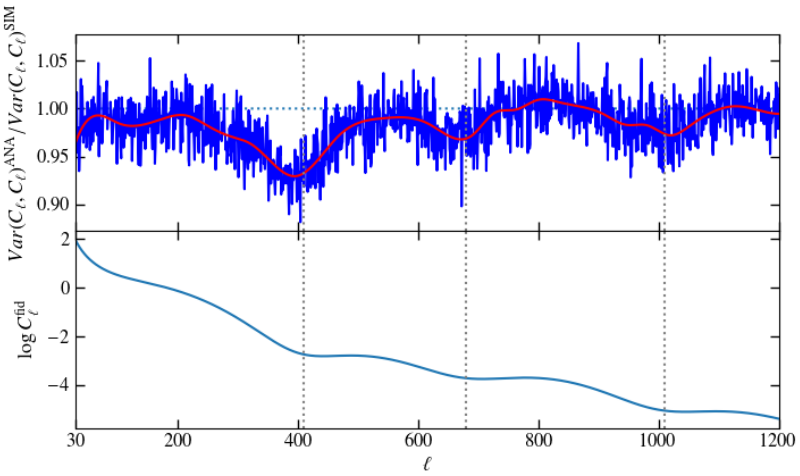

Figure 3.6: Ratio of the analytic power spectrum variance to the simulated

Top: ratio of the analytic variance to the simulated, from noise free simulations. The blue is the raw ratio and the red line is a smooth fit based on cubic splines. Bottom: the logarithm of the fiducial spectrum. The vertical dotted lines show that the minima in the ratio correspond to the multipoles where the drop of the power spectrum reaches a temporary plateau. These are the multipoles where the approximation that the spectrum does not vary over a small range of neighboring ℓs is most unrealistic.

is defined as

$$\tilde{a}_{\ell m} = \sum_i \Delta T_i w_i \Omega_i Y_{\ell m}(\grave{}_i)$$

where Ω_i is the area of pixel i. The pseudo-harmonic $\tilde{a}_{\ell m}$s are related to the true $a_{\ell m}$s on the unmasked sky via a coupling matrix K:

$$\tilde{a}_{\ell m} = \sum_{\ell' m'} a_{\ell' m'} K_{\ell m \ell' m'}.$$

The detailed expression of K is not important for this discussion, but we note that K is close to 1 when $\ell = \ell'$, then drops off as ℓ' shifts away from ℓ.

The pseudo-C_ℓ estimator is constructed from the sum

$$\tilde{C}_\ell^p = \frac{1}{(2\ell+1)} \sum_m |\tilde{a}_{\ell m}|^2$$

and its covariance is given by

$$\begin{aligned} \langle \Delta\tilde{C}_\ell^p \Delta\tilde{C}_{\ell'}^p \rangle &= \frac{2}{(2\ell+1)(2\ell'+1)} \sum_{mm'} \sum_{\ell_1 m_1} \sum_{\ell_2 m_2} C_{\ell_1} C_{\ell_2} \\ &\times K_{\ell m \ell_1 m_1} K^*_{\ell' m' \ell_1 m_1} K^*_{\ell m \ell_2 m_2} K_{\ell' m' \ell_2 m_2}. \end{aligned}$$

To make the calculation above computationally feasible, the power spectrum is approximated as unchanged over small range of multipoles where $\Delta\ell$ is small and K is not negligible. Then C_{ℓ_1} and C_{ℓ_2} can be taken out of the summation and replaced by C_ℓ and C'_ℓ. This will simplify the expression to the following:

$$\langle \Delta\tilde{C}_\ell^p \Delta\tilde{C}_{\ell'}^p \rangle = \tilde{V}_{\ell\ell'} \approx 2 C_\ell C_{\ell'} \Xi(\ell, \ell', \tilde{W}^{(2)})$$

where

$$\Xi(\ell_1, \ell_2, \tilde{W}^{(2)}) = \sum_{\ell_3} \frac{(2\ell_3+1)}{4\pi} \tilde{W}^{(2)}_{\ell_3} \begin{pmatrix} \ell_1 & \ell_2 & \ell_3 \\ 0 & 0 & 0 \end{pmatrix}^2$$

and $\tilde{W}^{(2)}_\ell$ is the power spectrum of the square of the mask w_i,

$$\tilde{W}^{(2)}_\ell = \frac{1}{(2\ell+1)} \sum_m |\tilde{w}^{(2)}_{\ell m}|^2, \qquad \tilde{w}^{(2)}_{\ell m} = \sum_i w_i^2 \Omega_i Y_{\ell m}(\theta_i).$$

The effect of this approximation on the covariance is minimal where the power spectrum, C_ℓ is declining or about to. Restricting to the simpler case where $\ell = \ell'$, the reasoning is as follows.

When the spectrum is declining around a certain ℓ, using C_ℓ to replace its neighboring multipoles means that the calculation is underestimating the contribution to the variance from $\ell_1, \ell_2 < \ell$ and overestimating from $\ell_1, \ell_2 > \ell$. So on average, the effect partly evens out.

At the high-ℓ end of plateaus, the central C_ℓ is about the same as the neighboring ones at smaller multipoles and larger than those at larger multipoles. The approximation means that we treat the neighboring C_{ℓ_1} and C_{ℓ_2} at $\ell_1, \ell_2 > \ell$ to be as large as C_ℓ. With the neighboring Ks being small, we are overestimating the contributions from terms that are relatively small compared to the “correct answer". The fractional difference is negligible.

However, when the spectrum is at the end of a slope and the start of a plateau, we use a central C_ℓ to approximate neighboring, larger C_{ℓ_1} and C_{ℓ_2} at $\ell_1, \ell_2 < \ell$. Unlike the case at the high-ℓ end of plateaus, we are now underestimating terms that are not so small compared to the “correct answer", even with the neighboring Ks being small. The fractional difference is more

significant.

Figure 3.6 demonstrates the correspondence between the troughs of the ratio of the analytic variance to the simulated and the locations in the $\log C_\ell$ where the drop of power spectrum reaches a temporary plateau, supporting our argument. We also note that at around $\ell = 400$ where the drop is sharpest, the disagreement between analytic and simulated variance is largest.

For a flat noise spectrum, the above approximation is exactly valid. Therefore the analytic covariance is more accurate for simulated maps with white noise, particularly at higher multipoles where the spectrum is noise-dominated.

This deviation of analytic covariance from the simulated covariance is why we make corrections on the former based on the latter.

References

Addison, G. E., Y. Huang, D. J. Watts, C. L. Bennett, M. Halpern, G. Hinshaw, and J. L. Weiland (2016). "Quantifying Discordance in the 2015 Planck CMB Spectrum". In: *APJ* 818.2, 132, p. 132. DOI: 10.3847/0004-637X/818/2/132. arXiv: 1511.00055 [astro-ph.CO].

Bennett, C. L., M. Halpern, G. Hinshaw, N. Jarosik, A. Kogut, M. Limon, S. S. Meyer, L. Page, D. N. Spergel, G. S. Tucker, E. Wollack, E. L. Wright, C. Barnes, M. R. Greason, R. S. Hill, E. Komatsu, M. R. Nolta, N. Odegard, H. V. Peiris, L. Verde, and J. L. Weiland (2003). "First-Year Wilkinson Microwave Anisotropy Probe (WMAP) Observations: Preliminary Maps and Basic Results". In: *APJS* 148.1, pp. 1–27. DOI: 10.1086/377253. arXiv: astro-ph/0302207 [astro-ph].

Bennett, C. L., D. Larson, J. L. Weiland, N. Jarosik, G. Hinshaw, N. Odegard, K. M. Smith, R. S. Hill, B. Gold, M. Halpern, E. Komatsu, M. R. Nolta, L. Page, D. N. Spergel, E. Wollack, J. Dunkley, A. Kogut, M. Limon, S. S. Meyer, G. S. Tucker, and E. L. Wright (2013). "Nine-year Wilkinson Microwave Anisotropy Probe (WMAP) Observations: Final Maps and Results". In: *APJS* 208.2, 20, p. 20. DOI: 10.1088/0067-0049/208/2/20. arXiv: 1212.5225 [astro-ph.CO].

Efstathiou, G. (2004). "Myths and truths concerning estimation of power spectra: the case for a hybrid estimator". In: *MNRAS* 349.2, pp. 603–626. DOI: 10.1111/j.1365-2966.2004.07530.x. arXiv: astro-ph/0307515 [astro-ph].

Fendt, William A. and Benjamin D. Wandelt (2007). "Pico: Parameters for the Impatient Cosmologist". In: *APJ* 654.1, pp. 2–11. DOI: 10.1086/508342. arXiv: astro-ph/0606709 [astro-ph].

Górski, K. M., E. Hivon, A. J. Banday, B. D. Wand elt, F. K. Hansen, M. Reinecke, and M. Bartelmann (2005). "HEALPix: A Framework for High-Resolution Discretization and Fast Analysis of Data Distributed on the Sphere". In:

APJ 622.2, pp. 759–771. DOI: 10.1086/427976. arXiv: astro-ph/0409513 [astro-ph].

Gruetjen, H. F. and E. P. S. Shellard (2014). "Towards efficient and optimal analysis of CMB anisotropies on a masked sky". In: *PRD* 89.6, 063008, p. 063008. DOI: 10.1103/PhysRevD.89.063008. arXiv: 1212.6945 [astro-ph.CO].

Hinshaw, G., M. R. Nolta, C. L. Bennett, R. Bean, O. Doré, M. R. Greason, M. Halpern, R. S. Hill, N. Jarosik, A. Kogut, E. Komatsu, M. Limon, N. Odegard, S. S. Meyer, L. Page, H. V. Peiris, D. N. Spergel, G. S. Tucker, L. Verde, J. L. Weiland, E. Wollack, and E. L. Wright (2007). "Three-Year Wilkinson Microwave Anisotropy Probe (WMAP) Observations: Temperature Analysis". In: *APJS* 170.2, pp. 288–334. DOI: 10.1086/513698. arXiv: astro-ph/0603451 [astro-ph].

Hinshaw, G., D. N. Spergel, L. Verde, R. S. Hill, S. S. Meyer, C. Barnes, C. L. Bennett, M. Halpern, N. Jarosik, A. Kogut, E. Komatsu, M. Limon, L. Page, G. S. Tucker, J. L. Weiland, E. Wollack, and E. L. Wright (2003). "First-Year Wilkinson Microwave Anisotropy Probe (WMAP) Observations: The Angular Power Spectrum". In: *APJS* 148.1, pp. 135–159. DOI: 10.1086/377225. arXiv: astro-ph/0302217 [astro-ph].

Hivon, Eric, Krzysztof M. Górski, C. Barth Netterfield, Brendan P. Crill, Simon Prunet, and Frode Hansen (2002). "MASTER of the Cosmic Microwave Background Anisotropy Power Spectrum: A Fast Method for Statistical Analysis of Large and Complex Cosmic Microwave Background Data Sets". In: *APJ* 567.1, pp. 2–17. DOI: 10.1086/338126. arXiv: astro-ph/0105302 [astro-ph].

Hojjati, Alireza, Ian G. McCarthy, Joachim Harnois-Deraps, Yin-Zhe Ma, Ludovic Van Waerbeke, Gary Hinshaw, and Amandine M. C. Le Brun (2015). "Dissecting the thermal Sunyaev-Zeldovich-gravitational lensing cross-correlation with hydrodynamical simulations". In: *JCAP* 2015.10, 047, p. 047. DOI: 10.1088/1475-7516/2015/10/047. arXiv: 1412.6051 [astro-ph.CO].

Hou, Z., K. Aylor, B. A. Benson, L. E. Bleem, J. E. Carlstrom, C. L. Chang, H. M. Cho, R. Chown, T. M. Crawford, A. T. Crites, T. de Haan, M. A. Dobbs, W. B. Everett, B. Follin, E. M. George, N. W. Halverson, N. L. Harrington, G. P. Holder, W. L. Holzapfel, J. D. Hrubes, R. Keisler, L. Knox, A. T. Lee, E. M. Leitch, D. Luong-Van, D. P. Marrone, J. J. McMahon, S. S. Meyer, M. Millea, L. M. Mocanu, J. J. Mohr, T. Natoli, Y. Omori, S. Padin, C. Pryke, C. L. Reichardt, J. E. Ruhl, J. T. Sayre, K. K. Schaffer, E. Shirokoff, Z. Staniszewski, A. A. Stark, K. T. Story, K. Vanderlinde, J. D. Vieira, and R.

Williamson (2018). "A Comparison of Maps and Power Spectra Determined from South Pole Telescope and Planck Data". In: *APJ* 853.1, 3, p. 3. DOI: 10.3847/1538-4357/aaa3ef. arXiv: 1704.00884 [astro-ph.CO].

Joudaki, Shahab, Chris Blake, Andrew Johnson, Alexandra Amon, Marika Asgari, Ami Choi, Thomas Erben, Karl Glazebrook, Joachim Harnois-Déraps, Catherine Heymans, Hendrik Hildebrand t, Henk Hoekstra, Dominik Klaes, Konrad Kuijken, Chris Lidman, Alexander Mead, Lance Miller, David Parkinson, Gregory B. Poole, Peter Schneider, Massimo Viola, and Christian Wolf (2018). "KiDS-450 + 2dFLenS: Cosmological parameter constraints from weak gravitational lensing tomography and overlapping redshift-space galaxy clustering". In: *MNRAS* 474.4, pp. 4894–4924. DOI: 10.1093/mnras/stx2820. arXiv: 1707.06627 [astro-ph.CO].

Köhlinger, F., M. Viola, B. Joachimi, H. Hoekstra, E. van Uitert, H. Hildebrandt, A. Choi, T. Erben, C. Heymans, S. Joudaki, D. Klaes, K. Kuijken, J. Merten, L. Miller, P. Schneider, and E. A. Valentijn (2017). "KiDS-450: the tomographic weak lensing power spectrum and constraints on cosmological parameters". In: *MNRAS* 471.4, pp. 4412–4435. DOI: 10.1093/mnras/stx1820. arXiv: 1706.02892 [astro-ph.CO].

Larson, D., J. Dunkley, G. Hinshaw, E. Komatsu, M. R. Nolta, C. L. Bennett, B. Gold, M. Halpern, R. S. Hill, N. Jarosik, A. Kogut, M. Limon, S. S. Meyer, N. Odegard, L. Page, K. M. Smith, D. N. Spergel, G. S. Tucker, J. L. Weiland, E. Wollack, and E. L. Wright (2011). "Seven-year Wilkinson Microwave Anisotropy Probe (WMAP) Observations: Power Spectra and WMAP-derived Parameters". In: *APJS* 192.2, 16, p. 16. DOI: 10.1088/0067-0049/192/2/16. arXiv: 1001.4635 [astro-ph.CO].

Larson, D., J. L. Weiland, G. Hinshaw, and C. L. Bennett (2015). "Comparing Planck and WMAP: Maps, Spectra, and Parameters". In: *APJ* 801.1, 9, p. 9. DOI: 10.1088/0004-637X/801/1/9. arXiv: 1409.7718 [astro-ph.CO].

Lewis, Antony and Sarah Bridle (2002). "Cosmological parameters from CMB and other data: A Monte Carlo approach". In: *PRD* 66.10, 103511, p. 103511. DOI: 10.1103/PhysRevD.66.103511. arXiv: astro-ph/0205436 [astro-ph].

Louis, Thibaut, Graeme E. Addison, Matthew Hasselfield, J. Richard Bond, Erminia Calabrese, Sudeep Das, Mark J. Devlin, Joanna Dunkley, Rolando Dünner, Megan Gralla, Amir Hajian, Adam D. Hincks, Renée Hlozek, Kevin Huffenberger, Leopoldo Infante, Arthur Kosowsky, Tobias A. Marriage, Kavilan Moodley, Sigurd Næss, Michael D. Niemack, Michael R.

Nolta, Lyman A. Page, Bruce Partridge, Neelima Sehgal, Jonathan L. Sievers, David N. Spergel, Suzanne T. Staggs, Benjamin Z. Walter, and Edward J. Wollack (2014). "The Atacama Cosmology Telescope: cross correlation with Planck maps". In: *JCAP* 2014.7, 016, p. 016. DOI: 10.1088/1475-7516/2014/07/016. arXiv: 1403.0608 [astro-ph.CO].

McCarthy, Ian G., Simeon Bird, Joop Schaye, Joachim Harnois-Deraps, Andreea S. Font, and Ludovic van Waerbeke (2018). "The BAHAMAS project: the CMB-large-scale structure tension and the roles of massive neutrinos and galaxy formation". In: *MNRAS* 476.3, pp. 2999–3030. DOI: 10.1093/mnras/sty377. arXiv: 1712.02411 [astro-ph.CO].

Planck Collaboration (2016). "Planck 2015 results. VIII. High Frequency Instrument data processing: Calibration and maps". In: *AAP* 594, A8, A8. DOI: 10.1051/0004-6361/201525820. arXiv: 1502.01587 [astro-ph.CO].

Planck Collaboration (2014a). "Planck 2013 results. I. Overview of products and scientific results". In: *AAP* 571, A1, A1. DOI: 10.1051/0004-6361/201321529. arXiv: 1303.5062 [astro-ph.CO].

Planck Collaboration (2014b). "Planck 2013 results. XVI. Cosmological parameters". In: *AAP* 571, A16, A16. DOI: 10.1051/0004-6361/201321591. arXiv: 1303.5076 [astro-ph.CO].

Planck Collaboration (2016a). "Planck 2015 results. I. Overview of products and scientific results". In: *AAP* 594, A1, A1. DOI: 10.1051/0004-6361/201527101. arXiv: 1502.01582 [astro-ph.CO].

Planck Collaboration (2016b). "Planck 2015 results. XI. CMB power spectra, likelihoods, and robustness of parameters". In: *AAP* 594, A11, A11. DOI: 10.1051/0004-6361/201526926. arXiv: 1507.02704 [astro-ph.CO].

Planck Collaboration (2016c). "Planck 2015 results. XIII. Cosmological parameters". In: *AAP* 594, A13, A13. DOI: 10.1051/0004-6361/201525830. arXiv: 1502.01589 [astro-ph.CO].

Planck Collaboration (2016d). "Planck 2015 results. XIV. Dark energy and modified gravity". In: *AAP* 594, A14, A14. DOI: 10.1051/0004-6361/201525814. arXiv: 1502.01590 [astro-ph.CO].

Planck Collaboration (2016e). "Planck intermediate results. XLVI. Reduction of large-scale systematic effects in HFI polarization maps and estimation of the reionization optical depth". In: *AAP* 596, A107, A107. DOI: 10.1051/0004-6361/201628890. arXiv: 1605.02985 [astro-ph.CO].

Planck Collaboration (2017). "Planck intermediate results. LI. Features in the cosmic microwave background temperature power spectrum and shifts

in cosmological parameters". In: *AAP* 607, A95, A95. DOI: 10.1051/0004-6361/201629504. arXiv: 1608.02487 [astro-ph.CO].

Planck Collaboration (2018a). "Planck 2018 results. I. Overview and the cosmological legacy of Planck". In: *arXiv e-prints*, arXiv:1807.06205, arXiv:1807.06205. arXiv: 1807.06205 [astro-ph.CO].

Planck Collaboration (2018b). "Planck 2018 results. VI. Cosmological parameters". In: *arXiv e-prints*, arXiv:1807.06209, arXiv:1807.06209. arXiv: 1807.06209 [astro-ph.CO].

Riess, Adam G., Stefano Casertano, Wenlong Yuan, Lucas Macri, Jay Anderson, John W. MacKenty, J. Bradley Bowers, Kelsey I. Clubb, Alexei V. Filippenko, David O. Jones, and Brad E. Tucker (2018). "New Parallaxes of Galactic Cepheids from Spatially Scanning the Hubble Space Telescope: Implications for the Hubble Constant". In: *APJ* 855.2, 136, p. 136. DOI: 10.3847/1538-4357/aaadb7. arXiv: 1801.01120 [astro-ph.SR].

Sellentin, Elena and Alan F. Heavens (2016). "Parameter inference with estimated covariance matrices". In: *MNRAS* 456.1, pp. L132–L136. DOI: 10.1093/mnrasl/slv190. arXiv: 1511.05969 [astro-ph.CO].

Sievers, Jonathan L., Renée A. Hlozek, Michael R. Nolta, Viviana Acquaviva, Graeme E. Addison, Peter A. R. Ade, Paula Aguirre, Mandana Amiri, John William Appel, L. Felipe Barrientos, Elia S. Battistelli, Nick Battaglia, J. Richard Bond, Ben Brown, Bryce Burger, Erminia Calabrese, Jay Chervenak, Devin Crichton, Sudeep Das, Mark J. Devlin, Simon R. Dicker, W. Bertrand Doriese, Joanna Dunkley, Rolando Dünner, Thomas Essinger-Hileman, David Faber, Ryan P. Fisher, Joseph W. Fowler, Patricio Gallardo, Michael S. Gordon, Megan B. Gralla, Amir Hajian, Mark Halpern, Matthew Hasselfield, Carlos Hernández-Monteagudo, J. Colin Hill, Gene C. Hilton, Matt Hilton, Adam D. Hincks, Dave Holtz, Kevin M. Huffenberger, David H. Hughes, John P. Hughes, Leopoldo Infante, Kent D. Irwin, David R. Jacobson, Brittany Johnstone, Jean Baptiste Juin, Madhuri Kaul, Jeff Klein, Arthur Kosowsky, Judy M. Lau, Michele Limon, Yen-Ting Lin, Thibaut Louis, Robert H. Lupton, Tobias A. Marriage, Danica Marsden, Krista Martocci, Phil Mauskopf, Michael McLaren, Felipe Menanteau, Kavilan Moodley, Harvey Moseley, Calvin B. Netterfield, Michael D. Niemack, Lyman A. Page, William A. Page, Lucas Parker, Bruce Partridge, Reed Plimpton, Hernan Quintana, Erik D. Reese, Beth Reid, Felipe Rojas, Neelima Sehgal, Blake D. Sherwin, Benjamin L. Schmitt, David N. Spergel, Suzanne T. Staggs, Omelan Stryzak, Daniel S. Swetz, Eric R. Switzer, Robert Thornton, Hy Trac, Carole Tucker, Masao Uehara, Katerina Visnjic, Ryan Warne, Grant

Wilson, Ed Wollack, Yue Zhao, and Caroline Zunckel (2013). "The Atacama Cosmology Telescope: cosmological parameters from three seasons of data". In: *JCAP* 2013.10, 060, p. 060. DOI: 10.1088/1475-7516/2013/10/060. arXiv: 1301.0824 [astro-ph.CO].

Story, K. T., C. L. Reichardt, Z. Hou, R. Keisler, K. A. Aird, B. A. Benson, L. E. Bleem, J. E. Carlstrom, C. L. Chang, H. M. Cho, T. M. Crawford, A. T. Crites, T. de Haan, M. A. Dobbs, J. Dudley, B. Follin, E. M. George, N. W. Halverson, G. P. Holder, W. L. Holzapfel, S. Hoover, J. D. Hrubes, M. Joy, L. Knox, A. T. Lee, E. M. Leitch, M. Lueker, D. Luong-Van, J. J. McMahon, J. Mehl, S. S. Meyer, M. Millea, J. J. Mohr, T. E. Montroy, S. Padin, T. Plagge, C. Pryke, J. E. Ruhl, J. T. Sayre, K. K. Schaffer, L. Shaw, E. Shirokoff, H. G. Spieler, Z. Staniszewski, A. A. Stark, A. van Engelen, K. Vand erlinde, J. D. Vieira, R. Williamson, and O. Zahn (2013). "A Measurement of the Cosmic Microwave Background Damping Tail from the 2500-Square-Degree SPT-SZ Survey". In: *APJ* 779.1, 86, p. 86. DOI: 10.1088/0004-637X/779/1/86. arXiv: 1210.7231 [astro-ph.CO].

Szapudi, István, Simon Prunet, Dmitry Pogosyan, Alexander S. Szalay, and J. Richard Bond (2001). "Fast Cosmic Microwave Background Analyses via Correlation Functions". In: *APJL* 548.2, pp. L115–L118. DOI: 10.1086/319105.

Weiland, J. L., K. Osumi, G. E. Addison, C. L. Bennett, D. J. Watts, M. Halpern, and G. Hinshaw (2018). "Effect of Template Uncertainties on the WMAP and Planck Measures of the Optical Depth Due to Reionization". In: *APJ* 863.2, 161, p. 161. DOI: 10.3847/1538-4357/aad18b. arXiv: 1801.01226 [astro-ph.CO].

Chapter 4

Accounting for Correlations When Fitting Extra Cosmological Parameters

This chapter is taken from Huang et al. 2019 (*APJ 882.2, 124, p. 124*), where we highlight the importance of examining the correlations between additional parameters when investigating extensions to the standard ΛCDM model. Additional model parameters are typically varied one or two at a time, in a series of separate tests. The correlations between additional parameters arise when their effects on model predictions are similar, even if the parameters are not varied simultaneously. We show how these correlations can be quantified with simulations and Markov Chain Monte Carlo (MCMC) methods. As an example, we assume that ΛCDM is the true underlying model, and calculate the correlations expected between the phenomenological lensing amplitude parameter, A_L, the running of the spectral index, $n_{\rm run}$, and the primordial helium mass fraction, Y_P, when these parameters are varied one at a time along with the ΛCDM parameters in fits to the *Planck* 2015 temperature power

spectrum.

4.1 Introduction

Over the last decade, much progress has been made on putting precise constraints on cosmological parameters within the Λ cold dark matter (ΛCDM) model, particularly from CMB experiments (e.g., Bennett et al., 2013; Planck Collaboration XIII, 2016; Sievers et al., 2013; Story et al., 2013). In the most recent release of *Planck* results (Planck Collaboration VI, 2018), determinations of the standard ΛCDM parameters such as baryon density, Hubble constant and matter density have reached the percent level or below.

Although currently there is no convincing evidence for deviations from the standard ΛCDM model from any single experiment, tensions exist between the values of some parameters inferred from different datasets. The most severe one is the 4.4σ disagreement between the Hubble constant measurements from the anchor-Cepheid-supernova distance ladder by the SH0ES collaboration (Riess et al., 2019) and from the *Planck* CMB data (Planck Collaboration VI, 2018). The measurement of H_0 via strong lensing time delays (Bonvin et al., 2017; Birrer et al., 2019) is consistent with the distance ladder and in 2.5σ tension with *Planck*. Addison et al., 2018 showed that the tension between early and late time universe measurements persists even without the inclusion of *Planck* data, using baryon acoustic oscillation (BAO) scale measurements.

Extensions or alternatives to the ΛCDM model have been explored in an attempt to resolve the Hubble tension. For example, the effects of varying the effective number of neutrino species (e.g., Riess et al., 2016) and the equation

of state parameter of dark energy (e.g., Joudaki et al., 2017) have been studied, though these extensions have not been able to effectively relieve the tension without including multiple turning points in the evolution of the dark energy equation of state (Zhao et al., 2017). Recently, new ideas have been proposed as more promising solutions, for example, with the introduction of early dark energy (Poulin et al., 2019) or self-interacting massive neutrinos (Kreisch, Cyr-Racine, and Doré, 2019).

If there is physics that is yet unaccounted for, consistency tests within the ΛCDM model will eventually fail with sufficiently sensitive new data.

An example of a parameter used to test consistency is the lensing amplitude A_L. It was first introduced by Calabrese et al., 2008 as a phenomenological way to quantify the effect of weak gravitational lensing in the CMB power spectrum. By definition, $A_L = 1$ is the physical value. However, the *Planck* temperature power spectrum (TT) data have shown a persistent preference for $A_L > 1$ at 1.8-2.7σ depending on which datasets are included (Planck Collaboration XVI, 2014; Planck Collaboration XIII, 2016; Planck Collaboration VI, 2018). For discussion of the A_L tension, see also Addison et al., 2016; Motloch and Hu, 2018; Motloch and Hu, 2019a. The cause of the deviation of A_L from its physical value is unclear, however, varying A_L is an example of the sort of test that might ultimately shed light on the origin of the distance ladder tension.

Typically results from fitting additional model parameters are presented one or two at a time, a series of separate tests (for recent examples, see Heavens et al., 2017; Joudaki et al., 2017; Planck Collaboration VI, 2018). In this chapter,

we emphasize that constraints on some of these extension parameters may be correlated. Information is lost when ignoring these correlations. For example, when different parameters have similar effects on a theory prediction they cannot be perfectly distinguished with some given set of data. Also, for example, if specific types of correlations between a pair of parameters are expected in a theory, that can be tested for and provide valuable additional information.

As an illustration, the red point in Figure 4.1 shows the maximum likelihood (ML) values for two parameters, A and B, obtained from separate ΛCDM+A and ΛCDM+B fits. The green contours show the expected distribution of A and B fitted separately (estimated from e.g. simulations) if ΛCDM, with $A = 0$ and $B = 0$, is the true model. For this example we do not fit A and B at the same time in a ΛCDM+$A + B$ model.

Only looking at the ML values one at a time, as is usually done, would lead to an incorrect conclusion of consistency, as the ML values of A and B are each only 1 standard deviation away from their fiducial ΛCDM values. In contrast, in the 2-D space the shift from the fiducial point is orthogonal to the expected degeneracy direction and the ML point is actually outside the 99.7% contour. This shows that there is a strong disagreement between the data and the assumed ΛCDM model that was not revealed by treating ΛCDM+A and ΛCDM+B as independent tests. We are not concerned here with the cause of the disagreement (e.g., systematic errors, an incorrect model, etc.), but only with the loss of information from sequential fits of one independent parameter at a time. The point is that accounting for the correlation between

the extension parameters can give additional information.

Therefore, to more carefully assess whether the standard ΛCDM model can consistently describe data, the covariance of the set of extension parameters should be quantified.

In this chapter, the goal is to answer the following questions:

1. How do we calculate the expected correlation between different extension parameters to the standard ΛCDM model when constrained by the same data?

2. How do we incorporate these correlations into a more stringent test of the ΛCDM model?

As an example, we use the *Planck* 2015 temperature power spectrum likelihood code (Planck Collaboration XI, 2016). The outline of this paper is as follows. In Section 4.2 we present the theoretical basis of our work and two different methods to achieve our goals. We show results in Section 4.3, followed by a discussion in Section 4.4 of general recipes for similar analysis in the future and conclusions in Section 4.5.

4.2 Methodology

4.2.1 Estimating Correlation between Extension Parameters Using Simulations

In general it is not straightforward to infer the correlation between parameters A and B directly from MCMC fits to the ΛCDM+A and ΛCDM+B models that have already been performed by experimental collaborations like *Planck*.

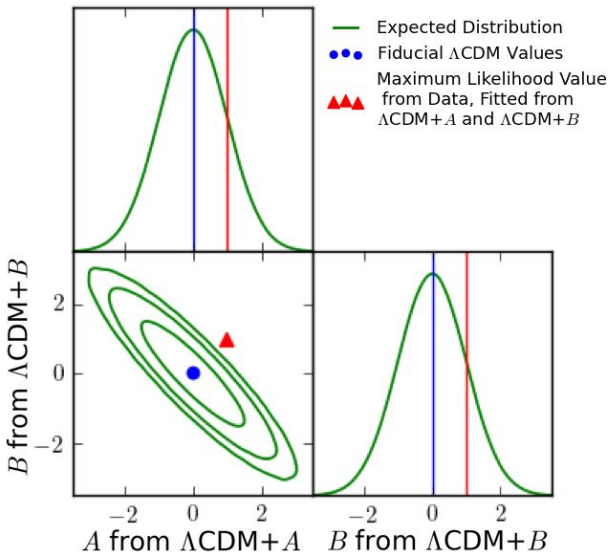

Figure 4.1: Illustration for correlations between additional model parameters
Accounting for correlations between additional model parameters can be important. In this example, A and B are additional parameters to the standard ΛCDM model. The maximum likelihood (ML) values of A and B from ΛCDM+A and ΛCDM+B fits to a particular dataset are shown in red. The green contours show the expected distribution of ML values, calculated assuming ΛCDM, with $A = 0$ and $B = 0$, is the true model. The ML values of A and B fitted from data appear consistent with their fiducial values in their 1-D marginalized distributions, but they are actually outside the 99.7% contour in their 2-D distribution.

To make progress, we assume that the data likelihood is Gaussian, with a covariance matrix $\boldsymbol{\mathcal{C}}$ that does not depend on the cosmological parameters, and that the posterior distribution for the cosmological parameters is also Gaussian.

The assumption of Gaussianity of the likelihood is made widely across different cosmological measurements, including CMB power spectra (e.g., Planck Collaboration XI, 2016; Louis et al., 2017; Henning et al., 2018), weak lensing shear (e.g., Krause et al., 2017; Hikage et al., 2019; Wright et al., 2018), galaxy clustering (e.g., Percival et al., 2014; Alam et al., 2017), supernovae distance moduli (e.g., Scolnic et al., 2018; Abbott et al., 2019), and others. The likelihood can almost always be made more Gaussian through compression of the data, often with negligible loss of cosmological information (e.g., combining CMB power spectra over a range of multipoles into bins). Neglecting the cosmological parameter dependence in the covariance (e.g., assuming a fixed fiducial model and set of parameters for computing the cosmic variance contribution to the errors) has also been demonstrated to be a suitable approximation for *Planck*, and other current experiments (e.g., Hamimeche and Lewis, 2008; Krause et al., 2017). The fiducial model as well as the covariance are often estimated from some iterative process of fitting the actual data.

For the *Planck* data, cosmological parameter posterior distributions can be well approximated as Gaussian for ΛCDM, as well as for many one- and two-parameter extensions, although there are also cases (e.g., involving curvature or varying the dark energy equation of state), where *Planck* alone does not provide Gaussian posteriors. Other experiments only constrain a portion of

the ΛCDM parameter space sufficiently well to produce Gaussian constraints in one or two parameters. Many parameters are also physically required to be positive, truncating the available parameter space and causing departure from Gaussianity when the data do not constrain the parameter to significantly differ from zero. This is the case for current cosmological constraints on the neutrino mass, for example (see Figure 30 of Planck Collaboration XIII, 2016). We return to the handling of non-Gaussian cases in Section 4.3.

In certain cases, the Bayesian posterior parameter distribution and the distribution of the ML parameter values from many realizations of the data are approximately equal. Specifically, $\mathbb{P}(\boldsymbol{\theta}|\boldsymbol{d})$, the Bayesian posterior distribution of parameters $\boldsymbol{\theta}$ sampled by MCMC given the experimental data, can well approximate $\mathbb{P}(\boldsymbol{\theta}^{\rm ML}(\boldsymbol{d}^{\rm sim})|\boldsymbol{\theta}^{\rm fid})$. The latter is the distribution of frequentist ML parameter estimation based on realizations of $\boldsymbol{d}^{\rm sim}$ from a fiducial model $\boldsymbol{\theta}^{\rm fid}$. The choice of $\boldsymbol{\theta}^{\rm fid}$ is usually physically motivated and is based on fits from actual data. For a detailed discussion, see e.g., Chapter 4 and Appendix B of Gelman et al., 2013.

We show in Section 4.6.2 that this correspondence is mathematically exact, if we: (1) assume the Gaussianity of both the data likelihood and the posterior distribution of parameters; (2) impose uninformative parameter priors that are far less constraining than the likelihood; (3) in the MCMC computation, replace the experimental data $\boldsymbol{d}$ with $\boldsymbol{\mu}(\boldsymbol{\theta}^{\rm fid})$, the theory prediction of the fiducial model. In other words, $\mathbb{P}(\boldsymbol{\theta}|\boldsymbol{d}=\boldsymbol{\mu}(\boldsymbol{\theta}^{\rm fid}))$ from MCMC and $\mathbb{P}(\boldsymbol{\theta}^{\rm ML}(\boldsymbol{d}^{\rm sim})|\boldsymbol{\theta}^{\rm fid})$ from simulations are the same mathematically. In this work, the fiducial model is from fitting the *Planck* TT data. We will show in Section 4.3.2 that the exact

choice of $\boldsymbol{\theta}^{\rm fid}$ is not very important.

This correspondence allows us to estimate the correlation between extension parameters A and B using simulated data (i.e., frequentist sampling of the likelihood) in the following steps:

1. Generate many simulated data sets (in our case simulated *Planck*-like CMB power spectra) drawn from the likelihood in the form of a Gaussian distribution $\mathcal{N}(\boldsymbol{\mu}(\boldsymbol{\theta}^{\rm fid}), \boldsymbol{\mathcal{C}})$ for some choice of fiducial ΛCDM model parameters, $\boldsymbol{\theta}^{\rm fid}$, and using the covariance matrix $\boldsymbol{\mathcal{C}}$ provided by the experiment collaboration.

2. Calculate the maximum-likelihood parameters $\boldsymbol{\theta}^{\rm ML}$ for the ΛCDM+A and ΛCDM+B models for each simulated data set, and

3. Estimate the covariance between A in the ΛCDM+A fit and B in the ΛCDM+B fit using the sample covariance from the simulations.

4.2.2 Estimating Correlation between Extension Parameters Using MCMC Chains

Alternatively, in the special case of Gaussian parameter posteriors, we can run MCMC chains to estimate the correlation between extension parameters directly. In Section 4.6.2 we show that all the information on the correlation between extension parameters A and B can be estimated from three sets of chains: ΛCDM+A, ΛCDM+B, and ΛCDM+$A+B$. Specifically, we found that the correlation between A and B when they are fitted separately is equal to minus one times the correlation between A and B when they are fitted together. We refer to this property as Correlation Equivalence.

A complication of estimating correlation between extension parameters by performing MCMC on the real data in this way is that we clearly do not have control over the 'underlying' cosmological model in the way we do when generating simulations. It is also possible that the real data have imperfections or systematic biases that are not correctly accounted for in the likelihood. We therefore instead performed MCMC computations replacing the real data vector with a theory prediction computed using the same $\boldsymbol{\theta}^{\rm fid}$ as for the simulations.

4.2.3 An Example With *Planck* CMB Spectra

Here we provide a worked example using *Planck* data for both the simulation and MCMC approaches discussed above. At the time of writing, the *Planck* 2018 likelihood code is not yet available. Therefore we perform a simple three-parameter test using the *Planck* $\ell \geq 30$ 2015 TT data from the `plik_lite` likelihood[1] (as described in Planck Collaboration XI, 2016). This simplified likelihood includes only CMB information, marginalizing over foreground template amplitudes and other nuisance parameters.

4.2.4 Fiducial Model and Extension Parameters

We assume the fiducial model to be the best-fit ΛCDM model of $\ell \geq 30$ *Planck* TT `plik_lite` data with the optical depth fixed at $\tau = 0.07$, the *Planck* calibration parameter `calPlanck` equal to 1 and other nuisance parameters marginalized. The $\ell < 30$ likelihood is pixel based rather than power spectrum

[1] Can be downloaded from http://pla.esac.esa.int/pla/#cosmology

based. For simplicity we only include the power spectrum based likelihood of the $\ell \geq 30$ data. Moreover, because the $\ell \geq 30$ TT spectrum only well constrains the parameter combination $A_s e^{-2\tau}$, τ is fixed to break the strong degeneracy with A_s. As for the calibration parameter `calPlanck`, a Gaussian prior with mean equal to 1 and standard deviation 0.0025 was originally imposed on it. Its variation has minimal impact on other parameters. For simplicity, `calPlanck` is fixed at 1.

For the standard ΛCDM parameters, we use

$$\{\Omega_b h^2, \Omega_c h^2, 100\theta_{MC}, \tau, \log A_s, n_s\}^{\text{fid}} =$$

$$\{0.02216, 0.1211, 1.0407, 0.07, 3.0777, 0.9601\}.$$

In addition, the three extension parameters of interest and their fiducial values for this example are $\{A_L, n_{\text{run}}, Y_P\}^{\text{fid}} = \{1, 0, 0.2453\}$. As mentioned in Section 4.1, A_L is a phenomenological parameter that artificially scales the lensing power spectrum. It is worth investigating as *Planck* has a curious preference for $A_L > 1$. Running of the spectral index, $n_{\text{run}} \equiv dn_s/d\ln k$, and the primordial Helium mass fraction Y_P are an interesting pair of extension parameters to test because of their high correlation (~ 0.9), that is, they produce similar changes in the power spectrum damping tail. Even a small deviation from their degeneracy direction in their expected 2-D distribution would be noticeable. In ΛCDM, Y_P is calculated from $\Omega_b h^2$ and the CMB temperature through big-bang nucleosynthesis (BBN) predictions (Planck Collaboration XIII, 2016). In ΛCDM+Y_P, Y_P is independent of BBN and decouples from $\Omega_b h^2$. We impose flat priors on all model parameters with the default `CosmoMC` (Lewis and Bridle,

2002) bounds.

The fiducial parameters from fitting the *Planck* data have uncertainties due to cosmic variance and experimental noise. A slightly different set of fiducial parameters, which are still consistent with the measured power spectrum, may produce different results in the covariance of the extension parameters as well as the significance of their deviations from the fiducial ΛCDM values. We found this effect to be small for the *Planck* 2015 data. See Section 4.3.2 for details.

4.2.5 Simulations

We run simulations to sample the distribution of the extension parameters. We draw 1000 binned power spectrum samples with mean equal to the binned power spectrum of the fiducial model and covariance equal to the `plik_lite` CMB band power covariance. We use the same binning scheme as *Planck* 2015 to convert power spectra computed by `CAMB`[2] to band powers. We replace the data spectrum in the `plik_lite` likelihood with our samples, thus forming the simulated likelihoods. Next, using the ML finding algorithm in `CosmoMC`, setting $\tau = 0.07$ and the *Planck* calibration parameter `calPlanck = 1`, we maximize the simulated likelihoods to obtain the best-fit parameters of a specific model for each realization. The models we explore are: the standard ΛCDM, ΛCDM+A_L, ΛCDM+$n_{\rm run}$ and ΛCDM+Y_P.

To quantify the overall shift between the values of the extension parameters estimated from the actual data and their fiducial ΛCDM values, we calculate

[2] https://camb.info/

the χ^2 and its probability to exceed (PTE) for a χ^2 distribution with degrees of freedom equal to the number of extension parameters:

$$\chi^2 = (\boldsymbol{\theta}^{\rm ML}_{\rm dat} - \boldsymbol{\theta}^{\rm fid})^T \boldsymbol{\Sigma}^{-1}_{\rm ex} (\boldsymbol{\theta}^{\rm ML}_{\rm dat} - \boldsymbol{\theta}^{\rm fid}) \tag{4.1}$$

where $\boldsymbol{\Sigma}_{\rm ex}$ is the covariance matrix for the extension parameters only, $\boldsymbol{\theta}^{\rm fid}$ is an array of 3 elements equal to $\{A_L, n_{\rm run}, Y_P\}^{\rm fid}$ and $\boldsymbol{\theta}^{\rm ML}_{\rm dat} = (1.1245, 0.00773, 0.2306)$ is an array whose values are obtained from fitting models ΛCDM+A_L, ΛCDM+$n_{\rm run}$ and ΛCDM+Y_P respectively on the actual *Planck* `plik_lite` TT data with τ fixed.

To verify that our priors on the parameters can be considered as uninformative and thus do not impact the degree of freedom for the χ^2, we compute the χ^2 values and their PTE assuming 3 degrees of freedom using the best-fit parameter values from all simulations. Then we compare the distribution of PTE values to the expected one with 3 degrees of freedom and find that they are consistent.

4.2.6 MCMC

As mentioned in Section 4.2.2, we can make use of Correlation Equivalence to estimate the expected covariance $\boldsymbol{\Sigma}_{\rm ex}$ between extension parameters fitted separately by running MCMC chains on the data likelihood, with the experimental power spectrum replaced by the fiducial one. Again we set $\tau = 0.07$ and the *Planck* calibration parameter `calPlanck`$= 1$.

The diagonal elements in $\boldsymbol{\Sigma}_{\rm ex}$ are estimated from the variances of the specific extension parameters from running the MCMC chains with the modified

Table 4.1: χ^2 of one-parameter extension models

	MCMC	simulation
χ^2	4.94	4.78
PTE	0.18	0.19
$\Delta\sigma$	0.9	0.9

The significance of the difference between the experimental ML values and the fiducial of A_L, $n_{\rm run}$ and Y_P, in terms of the χ^2 difference (with 3 degree of freedom) , its PTE and $\Delta\sigma$, the level of consistency in terms of the number of σ.
Note. Implementing the MCMC method and running simulations give consistent results, both implying that the shifts of the experimental extension parameters from their ΛCDM fiducial values are statistically insignificant.

Planck `plik_lite` TT likelihood, on the model ΛCDM+A_L, ΛCDM+$n_{\rm run}$ and ΛCDM+Y_P.

For the off-diagonal elements, first we obtain the correlation between two extension parameters (again, denoting them generically as A and B) from the MCMC runs that vary both of them in the ΛCDM+$A+B$ model with the same dataset. Then we calculate the covariance between A and B, given their variances as described in the last paragraph:

$$\begin{aligned} Cov(A,B)_{\text{fitted separately}} &= -corr(A,B)_{\Lambda\text{CDM}+A+B} \\ \times(Var(A)_{\Lambda\text{CDM}+A} &\times Var(B)_{\Lambda\text{CDM}+B})^{\frac{1}{2}}. \end{aligned} \tag{4.2}$$

This way, we are able to estimate all of the elements in $\mathbf{\Sigma}_{\rm ex}$ without running simulations at all, and calculate the χ^2 defined in Equation (4.1) and its PTE to quantify the shifts of the extension parameters from their fiducial values.

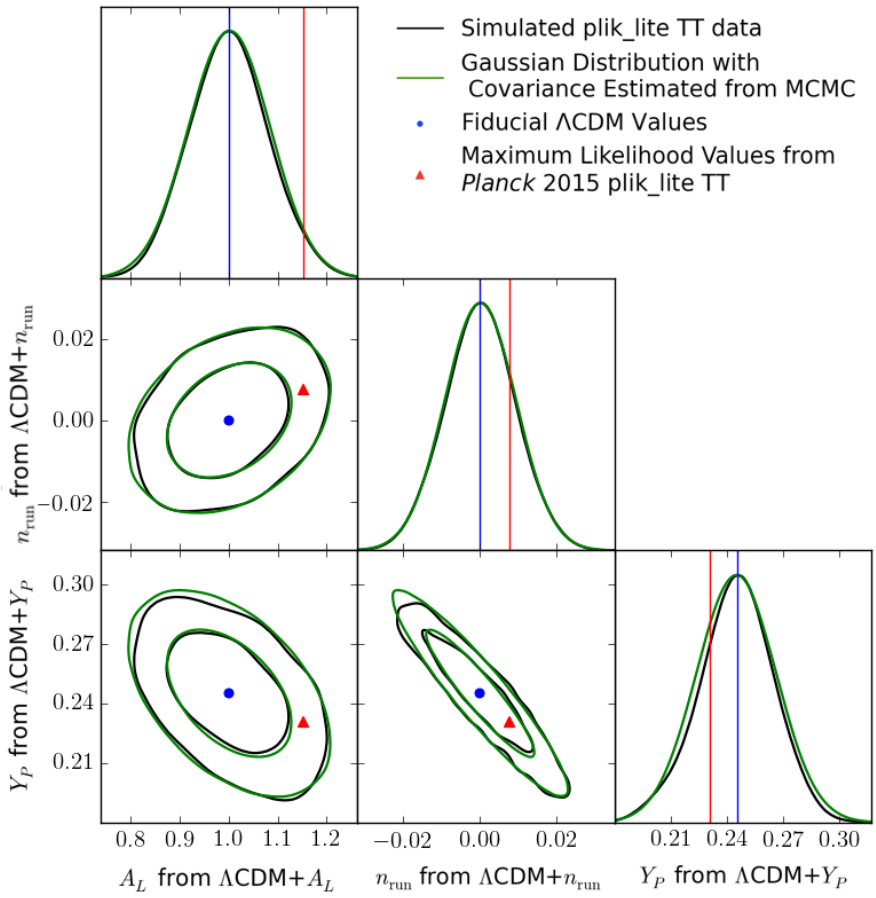

Figure 4.2: Triangle plot of A_L, $n_{\rm run}$ and Y_P, from separate fits

To illustrate the information in correlations between additional parameters fit beyond the standard ΛCDM, we examine the parameters A_L, $n_{\rm run}$ and Y_P. Shown in red are the ML values of A_L, $n_{\rm run}$ and Y_P in ΛCDM+A_L, ΛCDM+$n_{\rm run}$ and ΛCDM+Y_P fitted from the *Planck* 2015 `plik_lite` TT data. Note that all the base ΛCDM parameters have been marginalized over. The contours show the 68.3% and 95.5% confidence levels of the estimated multivariate distribution of the three parameters from simulations (black) and MCMC (green). In the black contours, there is numerical noise present due to the limited number of simulations. Notice that the ML points lie along the correlation directions, as expected from ΛCDM. Different extension parameters may have similar effects on the predicted power spectrum. Thus their constraints from data are correlated even if they are not fitted simultaneously. Taking their correlations into account, there is no significant deviation of all three parameters from their fiducial values, which is expected if the standard ΛCDM is the correct model.

Table 4.2: Parameter uncertainty of one-parameter extensions

Parameter	MCMC	Simulations
parameter uncertainty		
A_L	0.084	0.081
$n_{\rm run}$	0.0093	0.0093
Y_P	0.021	0.020
parameter correlation		
A_L v.s. $n_{\rm run}$	0.31	0.32
A_L v.s. Y_P	-0.46	-0.47
$n_{\rm run}$ v.s. Y_P	-0.93	-0.93

These are the parameter uncertainties and correlations for the extension parameters, estimated from the MCMC method and the simulations.Results from the two methods are consistent to a few percents. The largest discrepancy is in the uncertainty of Y_P, with 5% difference.

4.3 Results

4.3.1 Quantifying Significance of Deviations of Extension Parameters from Their Fiducial Values

In Table 4.1, we show the χ^2 of the difference, as defined in Equation (4.1), their corresponding PTE values and the level of consistency with the assumed model in terms of the number of σ. Our results imply no significant discrepancy (0.9σ) between the values of the three additional parameters estimated from the actual data in one-parameter extensions and their fiducial ΛCDM values. This is consistent with expectations if the standard ΛCDM is the correct model.

Taking a closer look at elements in the estimated covariance, we show in

Table 4.2 the estimated uncertainties of one-parameter extensions to the base ΛCDM model, along with the estimated parameter correlations from the two methods. These results are consistent up to at most 5%, in the Y_P uncertainty. The differences between using the two methods are likely due to numerical noise and have only a minimal impact on our main conclusion.

We also visualize the shifts of the ML extension parameters from their fiducial values compared to their expected distributions in Figure 4.2. Notice in the 2-D contour plots, how the ML points lie along the correlation/degeneracy direction of the estimated distributions, as expected if the base ΛCDM is the true model. Looking only at single extensions, the discrepancy between the ML value of A_L inferred by the `plik_lite` TT data and its fiducial value is only significant at 1.8σ (from the MCMC method) or 1.9σ (from simulations), while the deviations of $n_{\rm run}$ and Y_P from their fiducial values are only significant at 0.8σ and 0.7σ respectively, from both running MCMC and simulations.

We do not attempt to explain or de-emphasize the tension in A_L. Rather we note that there is no extra sign of discrepancy when we take into account its correlation with $n_{\rm run}$ or Y_P. The significance of the χ^2 of difference for the three parameters is not only reduced by the very small deviations of Y_P and $n_{\rm run}$, but is also reduced because the Planck `plik_lite` TT data prefers the shifts in the parameters along their expected degeneracy directions. Considering the A_L-$n_{\rm run}$ or the A_L-Y_P pair for example, their correlations are non-negligible: 0.31 and -0.46 respectively. This information is not contained in the single extension tests. Table 4.1 and Figure 4.2 together show that the correlation of A_L with $n_{\rm run}$ and Y_P are as expected if ΛCDM is the true model, even though

A_L deviates moderately with its fiducial value. Had we found inconsistency between the ML parameters from the data and the expected ΛCDM joint distribution, it could indicate the presence of systematic error or unknown physical effects producing spurious parameter correlations.

In addition, numerical differences between the simulated contours and those of MCMC are small in this figure, again providing confidence to both methods.

4.3.2 Testing Stability of Results Against Uncertainties in Fiducial Model

As mentioned in Section 4.2.4, the fiducial parameters are from fitting the actual `plik_lite` data and therefore have uncertainties. So the standard ΛCDM model we define is not just one point in the parameter space, but an ensemble of points whose shape is described by the parameter posterior distribution inferred from the data.

To assess the impact of different fiducial values on our results, we randomly draw 1000 sets of parameters from the MCMC chains fitted to the `plik_lite` data, with the base ΛCDM model, $\tau = 0.07$ and `calPlanck` = 1. For each set of parameters, we approximate the parameter covariance matrix by computing the C_ℓ derivatives and Fisher matrices (see Equation (4.14) in Section 4.6.2.1). Then we use Correlation Equivalence to calculate the extension parameter covariance $\mathbf{\Sigma}_{\rm ex}$. We find that varying parameters causes less than 3% scatter in the matrix elements.

We also plug $\mathbf{\Sigma}_{\rm ex}$ into Equation (4.1) and find that the resulting χ^2 ranges

from 4.2 to 5.1 and the PTE from 0.17 to 0.24, corresponding to consistency within 0.7-1σ. These results show that the uncertainties in the fiducial model have very minimal impact on results from our consistency test. The stability of the results reflects the constraining power of the *Planck* data on the model parameters in ΛCDM.

4.4 Discussion

In Sections 4.2 and 4.3 we have shown an example of quantifying the level of consistency between extension parameters and their fiducial values given a specific dataset. In this section, we outline and discuss steps to perform this approach more comprehensively for the *Planck* 2018 and other cosmology data sets.

4.4.1 MCMC Method

In the ideal case where all extension parameters of interest are Gaussian, we can estimate their expected distribution from MCMC chains. We denote the individual extension parameter as $\theta_{\mathrm{ex,i}}$ with i runs over 1 to n_{ex}, the total number of extension parameters. The suggested recipe is as follows:

1. Define a fiducial model (e.g. a fit from existing data) and calculate its theory prediction.

2. In the data likelihood of interest, substitute the experimental observables, e.g. power spectra in the CMB case, by the fiducial prediction.

3. Explore parameter space around the fiducial point by running MCMC

chains on the modified data likelihood(s), fitting models ΛCDM+$\theta_{\rm ex,i}$ and ΛCDM+$\theta_{\rm ex,i} + \theta_{\rm ex,j\neq i}$.

4. Calculate the variance of $\theta_{\rm ex,i}$ from the one-parameter extension, and the correlation between $\theta_{\rm ex,i}$ and $\theta_{\rm ex,j\neq i}$ from the two-parameter extension.

5. Using results from previous step, construct a covariance matrix $\mathbf{\Sigma}_{\rm ex}$ for $\boldsymbol{\theta}_{\rm ex}$, with the signs of all the correlations flipped.

6. Calculate χ^2 defined in Equation (4.1) and its PTE to quantify deviation of experimental values to fiducial ones. Additionally, one can plot confidence ellipses such as in Figure 4.2 to visualize the deviations.

7. Check validity of the input fiducial model, for example by using a Fisher Forecast (e.g. Heavens, 2009) to approximate parameter covariance and estimating the shifts in the χ^2 when varying fiducial parameter values.

As an example, on a computer cluster with 12-core 2.5 GHz processors[3], one MCMC run with 8 parallel chains usually take $\lesssim 24$ hours to converge for the 2015 `plik_lite` likelihood. The CPU time for running one MCMC job is at the order of 100 hours and the total computing time is $\sim 5 \times 10^4$ hours, for running all one-parameter and two-parameter extension fits for $n_{\rm ex} = 11$, which is the number of extra parameters fitted in the publicly available 2015 *Planck* chains.

[3]Our computation was conducted on the computer cluster of the Maryland Advanced Research Computing Center. See https://www.marcc.jhu.edu/cyberinfrastructure/hardware/ for descriptions of its system architecture.

4.4.2 Simulations

We can use simulations, as an alternative method to estimate the expected distribution of additional parameters around the fiducial point. As described in Section 4.2.1 and 4.2.5, one can perform the following procedure:

1. Generate simulated observables of the fiducial model using data covariance.

2. For each simulation, estimate the best-fit ΛCDM+$\boldsymbol{\theta}_i^{ex}$ model for each extension parameter.

3. Calculate the covariance of extension parameter $\boldsymbol{\Sigma}_{\rm ex}$, the χ^2 of difference defined in Equation (4.1) and its PTE to quantify the significance of difference. Confidence ellipses can also be plotted.

For a rough estimate of computing time for the simulation method, using `CosmoMC` and the same computer cluster with 12 cores per CPU, we find that the running time of the best-fit-finding algorithm is approximately 1 hour. For $n_{\rm ex} = 11$, $n_{\rm sim} = 2000$ and running 4 parallel best-fit-finding jobs for each simulation (to reduce numerical noise and avoid obtaining results from local minima), the total computing time is 9×10^4 hours.

4.4.3 In the Case of Non-Gaussianity

To discuss the case of non-Gaussianity, first we need to clarify what exactly non-Gaussianity arises from. Recall that throughout this paper, we assume a Gaussian data likelihood and priors that are uninformative. If the data

constrains the parameters well enough, changes in the model predictions can be treated as only linearly dependent on the parameters. This means the Taylor expansion of the log likelihood around the maximum point is significant up to quadratic terms of the parameters and therefore the parameters are Gaussian (see Section 4.6.1).

In short, non-Gaussianity of parameters is a result of the data not being constraining enough for fitting parameters. When this is the case, there may not be a mathematical correspondence between the ML parameter distribution from the simulations and the posterior distribution of the MCMC chains, since our argument in Section 4.6.1 depends on the assumption of Gaussianity. Besides, since our proof of Correlation Equivalence in Section 4.6.2 also rests upon approximations of the log likelihood to only the second order derivatives, the property now becomes questionable. This means that we cannot simply estimate the correlation between parameters fit separately from the MCMC chains where they are fitted together. What is worse is that the means and the covariance matrix no longer carry all information of the parameter distributions and one might need to evaluate high order tensors (Sellentin, Quartin, and Amendola, 2014). Additionally, the χ^2 test is inappropriate for non-Gaussian parameters and we need new ways (such as one proposed in Appendix C of Motloch and Hu, 2019b) to quantify the significance of the overall difference between the experimental parameters and their fiducial values.

An example of non-Gaussian parameters are those with priors that are more informative than the data, e.g. the neutrino mass $\sum m_\nu$ and the tensor to

scalar ratio r, physically defined as non-negative. Current CMB data are not sufficiently constraining to pull these parameters away from lower bounds (BICEP2 Collaboration et al., 2018; Planck Collaboration VI, 2018). Another non-Gaussian parameter given just the TT data, is the curvature density Ω_k. Curvature can only be weakly constrained as allowing it to be free worsens the existing degeneracy between the physical matter density Ω_m and the Hubble constant H_0 (Zaldarriaga, Spergel, and Seljak, 1997; Percival et al., 2002; Kable, Addison, and Bennett, 2019). In the MCMC method, a two-parameter extension model with both A_L and Ω_k results in very wide and non-Gaussian distributions, since they are highly correlated — a positive curvature has similar effect as an increased lensing signal (Planck Collaboration XIII, 2016).

To reduce non-Gaussianity, one can always include more datasets if available to have greater constraining power on the parameter, e.g. include the BAO data (Alam et al., 2017) in parameter fitting along with *Planck*. However, when extensions are used as a means to test the internal consistency of one dataset, adding extra data is not an option. Fortunately, there are existing methods of transforming non-Gaussian parameters into Gaussian ones. One such method is the Box-Cox transformation (Box and Cox, 1964). Joachimi and Taylor, 2011 and Schuhmann, Joachimi, and Peiris, 2016 applied this bijective transformation to non-Gaussian cosmological parameters. Theoretically, Correlation Equivalence still holds for the transformed Gaussian parameters. Thus we may still apply the procedure outlined in Section 4.4.1 for transformed parameters, obtain the expected distribution for transformed ones,

and then transform them back to the model parameters. One thing to note is that the Box-Cox transformation does not guarantee Gaussianity. So one should check for the Gaussianity of transformed parameters, e.g. calculate the skewness and kurtosis of the resulting distribution, and if needed, apply a second transformation. For consistency, it is also a good idea to compare the resulting distribution of model parameters to simulations, or compare the covariance of the transformed parameters with predictions from Fisher Forecast, keeping in mind that Fisher Forecast assumes Gaussianity.

Further understanding of non-Gaussian scenarios is left for future efforts.

4.5 Conclusions

In this paper, we have presented a method to help identify potential new physics and/or systematic errors by calculating the correlations between additional parameters and performing a ΛCDM consistency test accounting for them.

Usually extension parameters are added to the model separately, one at a time. However, different parameters may affect the theory prediction in a similar way, which means their values from a given data set can be correlated, even when they are fit separately. Examining the consistency of extension parameters with ΛCDM expectations, accounting for these correlations, provides an additional test of the model beyond looking at the results from individual one-parameter extensions.

Under the assumption of Gaussianity of both the likelihood and the posterior distribution of the parameters, one can fit a series of one-parameter

extension models to simulated data and obtain the multivariate distribution of the extension parameters. With the base parameters marginalized over, the χ^2 of difference and its PTE can be calculated to quantify the significance of deviations from ΛCDM.

A more computationally economic alternative is to run MCMC, fitting the same series of one-parameter extension models and additionally two-parameter extensions across all the possible pairs in the set of parameters of interest. Using Correlation Equivalence as proven in Section 4.6.2, the covariance matrix of the extension parameters fitted separately can be estimated from the results of these MCMC runs and so the expected multivariate Gaussian distribution can be obtained.

In an attempt to narrow down causes of the A_L anomaly in the *Planck* data and possibly shed light on tensions between cosmological measurements, we looked at the example parameter combination $\{A_L, n_{\rm run}, Y_P\}$, fitted with the *Planck* 2015 `plik_lite` $\ell \geq 30$ TT data, as we do not yet have access to the *Planck* 2018 likelihood. Results from MCMC and simulations show that the deviations of the three additional parameters from their fiducial ΛCDM values are consistent with statistical fluctuations within 0.9σ when correlations are accounted for.

Although the cause of the reported 1.8-2.7σ preference (depending on the the specific combination of datasets) for $A_L > 1$ by the *Planck* CMB data is yet to be understood, we find no further evidence for discrepancy when considering the correlations between A_L, $n_{\rm run}$ and Y_P. This is not a trivial test, as the correlations are significant: approximately 0.31 for A_L-$n_{\rm run}$, -0.46 for

A_L-Y_P, and -0.93 for $n_{\rm run}$-Y_P. If the unphysical $A_L > 1$ is a symptom of an underlying systematic error or some real but unknown physical effect that also produced spurious correlations with $n_{\rm run}$ or Y_P our test could have revealed this.

We also tested the stability of results against the uncertainties in the parameters of the experimentally fitted fiducial model, and find that the change of the fiducial model has no impact on our conclusions, only shifting the PTE values from 0.17 to 0.24.

Furthermore, we discussed how our procedures depend on the assumption of Gaussianity of parameters. If the assumption is not valid, MCMC runs cannot simply be used to estimate correlations between parameter fitted separately, nor may there be a mathematical correspondence between parameter distributions from the simulations and the MCMC runs. Therefore, efforts might attempt to include Gaussianization of non-Gaussian parameters, such as using the Box-Cox transformation (Box and Cox, 1964).

The procedures developed in this paper can and should be applied to more extensive lists of extension parameters, with existing and future cosmological data, in order to provide a more stringent test and complete view of ΛCDM consistency.

4.6 Appendix

4.6.1 Mathematical Correspondence Between Frequentist Maximum likelihood Parameters and Bayesian Parameter Posterior

In this section, we will show that there is a mathematical correspondence between frequentist maximum likelihood (ML) parameters and Bayesian parameter posterior, under conditions described below. In other words, $\mathbb{P}(\boldsymbol{\theta}^{\rm ML}(\boldsymbol{d}^{\rm sim})|\boldsymbol{\theta}^{\rm fid})$, the distribution of ML parameters estimated from realizations of a fiducial model is mathematically the same as $\mathbb{P}(\boldsymbol{\theta}|\boldsymbol{d} = \boldsymbol{\mu}(\boldsymbol{\theta}^{\rm fid}))$, the Bayesian posterior distribution of parameters given a set of data that matches the theory prediction of the same fiducial model.

Given a set of fiducial parameters $\boldsymbol{\theta}^{\rm fid}$, we can calculate its theory prediction $\boldsymbol{\mu}(\boldsymbol{\theta}^{\rm fid})$. With $\boldsymbol{\mathcal{C}}$ as the data covariance estimated experimentally, we can then draw realizations of the data vector $\boldsymbol{d}$ from a multivariate Gaussian distribution $\mathcal{N}(\boldsymbol{\mu}(\boldsymbol{\theta}^{\rm fid}), \boldsymbol{\mathcal{C}})$

Up to some constants, the log probability density function of $\boldsymbol{d}$ is given by

$$\log \mathbb{P}(\boldsymbol{d}^{\rm sim}|\boldsymbol{\theta}^{\rm fid}) = -\frac{1}{2}(\boldsymbol{d}^{\rm sim} - \boldsymbol{\mu}(\boldsymbol{\theta}^{\rm fid}))^T \boldsymbol{\mathcal{C}}^{-1}(\boldsymbol{d}^{\rm sim} - \boldsymbol{\mu}(\boldsymbol{\theta}^{\rm fid})). \tag{4.3}$$

For a given set of simulated data $\boldsymbol{d}^{\rm sim}$, we can estimate the set of parameters that best describe it by maximizing the log-likelihood

$$\log L(\boldsymbol{\theta}) \equiv \log \mathbb{P}(\boldsymbol{d}^{\rm sim}|\boldsymbol{\theta}). \tag{4.4}$$

The ML parameter estimates, $\boldsymbol{\theta}^{\rm ML}$, are defined as the solutions to the

simultaneous equations

$$\left.\frac{\partial \log \mathbb{P}(\boldsymbol{d}^{\rm sim}|\boldsymbol{\theta})}{\partial \theta_i}\right|_{\boldsymbol{\theta}=\boldsymbol{\theta}^{\rm ML}} = 0 \tag{4.5}$$

where the index i runs over all parameters. Taylor expanding around $\boldsymbol{\theta}^{\rm ML}$ gives

$$\begin{aligned}\log\mathbb{P}(\boldsymbol{d}^{\rm sim}|\boldsymbol{\theta}) &= \log \mathbb{P}(\boldsymbol{d}^{\rm sim}|\boldsymbol{\theta})\big|_{\boldsymbol{\theta}=\boldsymbol{\theta}^{\rm ML}} \\ &+ \frac{1}{2}\sum_{ij}(\theta_i - \theta_i^{\rm ML})\left[\frac{\partial^2 \log \mathbb{P}(\boldsymbol{d}^{\rm sim}|\boldsymbol{\theta})}{\partial\theta_i\partial\theta_j}\right]_{\boldsymbol{\theta}=\boldsymbol{\theta}^{\rm ML}}(\theta_j - \theta_j^{\rm ML}) \\ &+ \mathcal{O}(\boldsymbol{\theta} - \boldsymbol{\theta}^{\rm ML})^3.\end{aligned} \tag{4.6}$$

If higher-order terms can be neglected, Equation (4.6) shows that given a set of $\boldsymbol{d}$, parameters around the ML point can be approximated by a Gaussian distribution, with the covariance $\boldsymbol{\Sigma}$ given by

$$\boldsymbol{\Sigma}(\boldsymbol{\theta}^{\rm ML}(\boldsymbol{d}^{\rm sim}))_{ij} \;=\; \left[-\frac{\partial^2 \log \mathbb{P}(\boldsymbol{d}^{\rm sim}|\boldsymbol{\theta})}{\partial\theta_i\partial\theta_j}\right]^{-1}_{\boldsymbol{\theta}=\boldsymbol{\theta}^{\rm ML}} \tag{4.7}$$

where the term inside the brackets is the Fisher matrix and $\boldsymbol{\theta}^{\rm ML}$ is written as $\boldsymbol{\theta}^{\rm ML}(\boldsymbol{d}^{\rm sim})$ to emphasize its dependence on $\boldsymbol{d}^{\rm sim}$.

Note that the negligibility of higher order terms in (A4) means that $\boldsymbol{\Sigma}$ is approximately constant for different values of $\boldsymbol{\theta}^{\rm ML}$. For simplicity we can set it to be $\boldsymbol{\Sigma}(\boldsymbol{\theta}^{\rm fid})$.

Furthermore, assuming that the zeroth order term $\log \mathbb{P}(\boldsymbol{d}^{\rm sim}|\boldsymbol{\theta})\big|_{\boldsymbol{\theta}=\boldsymbol{\theta}^{\rm ML}}$ is also approximately a constant for all $\boldsymbol{\theta}^{\rm ML}$, we can interchange the positions of $\boldsymbol{\theta}$ and $\boldsymbol{\theta}^{\rm ML}$ in (A4) and set $\boldsymbol{\theta} = \boldsymbol{\theta}^{\rm fid}$, which gives $\mathbb{P}(\boldsymbol{\theta}^{\rm ML}(\boldsymbol{d}^{\rm sim})|\boldsymbol{\theta}^{\rm fid})$, the distribution of $\boldsymbol{\theta}^{\rm ML}$ from all simulated data $\boldsymbol{d}$. Up to some constants, the log

of $\mathbb{P}(\boldsymbol{\theta}^{\rm ML}(\boldsymbol{d}^{\rm sim})|\boldsymbol{\theta}^{\rm fid})$ is:

$$\log \mathbb{P}(\boldsymbol{\theta}^{\rm ML}(\boldsymbol{d}^{\rm sim})|\boldsymbol{\theta}^{\rm fid}) =$$

$$-\frac{1}{2}(\boldsymbol{\theta}^{\rm ML}(\boldsymbol{d}^{\rm sim}) - \boldsymbol{\theta}^{\rm fid})^T \boldsymbol{\Sigma}^{-1} (\boldsymbol{\theta}^{\rm ML}(\boldsymbol{d}^{\rm sim}) - \boldsymbol{\theta}^{\rm fid}) \tag{4.8}$$

From the Bayesian viewpoint, given a single set of data $\boldsymbol{d}$, the posterior parameter distribution is given by Bayes' theorem,

$$\mathbb{P}(\boldsymbol{\theta}|\boldsymbol{d}) = \frac{\mathbb{P}(\boldsymbol{d}|\boldsymbol{\theta})\mathbb{P}(\boldsymbol{\theta})}{\mathbb{P}(\boldsymbol{d})} \propto \mathbb{P}(\boldsymbol{d}|\boldsymbol{\theta})\mathbb{P}(\boldsymbol{\theta}), \tag{4.9}$$

where $\mathbb{P}(\boldsymbol{\theta})$ is the prior probability and $\mathbb{P}(\boldsymbol{d})$ is the evidence. If the posterior is Gaussian we can write, again up to some constants,

$$\log \mathbb{P}(\boldsymbol{\theta}|\boldsymbol{d}) = -\frac{1}{2}(\boldsymbol{\theta} - \bar{\boldsymbol{\theta}})^T \boldsymbol{\Sigma}^{-1} (\boldsymbol{\theta} - \bar{\boldsymbol{\theta}}), \tag{4.10}$$

where $\boldsymbol{\Sigma}$ is the parameter covariance matrix given by (A5). For flat priors $\bar{\boldsymbol{\theta}} = \boldsymbol{\theta}^{\rm ML}(\boldsymbol{d})$. If $\boldsymbol{\theta}^{\rm fid}$ mentioned above is close to $\boldsymbol{\theta}^{\rm ML}(\boldsymbol{d})$, then (A6) and (A8) is only different by a small offset. To make them exactly equal, we can choose to replace $\boldsymbol{d}$ with a theory prediction computed using $\boldsymbol{\theta}^{\rm fid}$ so that $\boldsymbol{\theta}^{\rm ML}$ becomes equal to $\boldsymbol{\theta}^{\rm fid}$ and the Bayesian posterior now describes the distribution of parameters around the fiducial value:

$$\begin{aligned} \mathbb{P}(\boldsymbol{\theta}|\boldsymbol{d} = \boldsymbol{\mu}(\boldsymbol{\theta}^{\rm fid})) &= \log \mathbb{P}(\boldsymbol{\theta}|\boldsymbol{\theta}^{\rm fid}) \\ &= -\frac{1}{2}(\boldsymbol{\theta} - \boldsymbol{\theta}^{\rm fid})^T \boldsymbol{\Sigma}^{-1} (\boldsymbol{\theta} - \boldsymbol{\theta}^{\rm fid}), \end{aligned} \tag{4.11}$$

which matches exactly the distribution of the frequentist ML parameter estimates given in (A6). This is asymptotically true even for non-flat priors when

the data are sufficiently constraining, and we do not discuss the exact choice of priors further here. For more information we again direct the reader to, for example, Chapter 4 of Gelman et al., 2013. We note that if the priors are informative this equivalence is broken and the method described in Section 4.2.2 would not be valid.

4.6.2 Correlation Equivalence

In this section, using the mathematical correspondence from Section 4.6.1, we show that when using ML estimation, the correlation between two parameters varied separately (e.g. the correlation between parameters A and B in model ΛCDM+A and ΛCDM+B) is the same but with an opposite sign as the correlation between the same two parameters varying together (e.g. ΛCDM+$A + B$).

4.6.2.1 Maximum Likelihood Estimation and Parameter Covariance

With $\mathfrak{L} \equiv \log L(\boldsymbol{\theta})$, the log likelihood of parameters given a specific sample of $\boldsymbol{d}$ can be written as

$$\mathfrak{L} = -\frac{1}{2}(\boldsymbol{d} - \boldsymbol{\mu}(\boldsymbol{\theta}))^T \boldsymbol{\mathcal{C}}^{-1} (\boldsymbol{d} - \boldsymbol{\mu}(\boldsymbol{\theta})) \tag{4.12}$$

up to some constants. $\boldsymbol{\mu}(\boldsymbol{\theta})$ is the theory prediction of the data given some set of parameters $\boldsymbol{\theta}$. For any $\boldsymbol{d}$, the goal is to find the $\boldsymbol{\theta}$ that maximize $\mathfrak{L}$.

As in Section 4.6.1, at maximum likelihood, the partial derivative of the log likelihood with respect to (w.r.t.) θ_i is zero (i runs over n, the number of

parameters). That is

$$\begin{aligned} \left.\frac{\partial \mathfrak{L}}{\partial \theta_i}\right|_{\mathrm{ML}} &= \left.\frac{\partial \mathfrak{L}}{\partial \boldsymbol{\mu}^T}\right|_{\mathrm{ML}} \left.\frac{\partial \boldsymbol{\mu}}{\partial \theta_i}\right|_{\mathrm{ML}} \\ &= -\left.\frac{\partial \boldsymbol{\mu}^T}{\partial \theta_i}\right|_{\mathrm{ML}} \boldsymbol{\mathcal{C}}^{-1}(\boldsymbol{d} - \boldsymbol{\mu}(\boldsymbol{\theta})) = 0. \end{aligned} \tag{4.13}$$

Close to the ML point in parameter space, we can Taylor expand the log likelihood to the second order in $\Delta\theta_i \equiv \theta_i - \theta_i^{\mathrm{ML}}$ as shown in Equation (4.6), where θ_i is well described by a multivariate Gaussian distribution. The parameter means are the values that maximize the likelihood.

The parameter covariance $\boldsymbol{\Sigma}$ can be calculated as the inverse of the Fisher matrix $\mathcal{F}^{-1}$, with the Fisher matrix, estimated from MCMC chains or calculated analytically, defined as:

$$\begin{aligned} \mathcal{F}_{ij} &= -\left.\frac{\partial^2 \mathfrak{L}}{\partial \theta_i \partial \theta_j}\right|_{\mathrm{ML}} \\ &= \boldsymbol{\mu}_{,i}^{\mathrm{ML,T}} \boldsymbol{\mathcal{C}}^{-1} \boldsymbol{\mu}_{,j}^{\mathrm{ML}}. \end{aligned} \tag{4.14}$$

From now on we use the comma notation to denote partial derivatives w.r.t. $\boldsymbol{\theta}$, that is, $\boldsymbol{\mu}_{,i} \equiv \frac{\partial \boldsymbol{\mu}}{\partial \theta_i}$.

In the following proof, we continue to work under the assumption of Gaussianity for $\boldsymbol{\theta}$ and expand $\boldsymbol{\mu}$ only to the first order of $\boldsymbol{\theta}$, that is, assuming the Gaussian linear model (Raveri and Hu, 2019), around a chosen fiducial model $\boldsymbol{\theta}^{\mathrm{fid}}$:

$$\boldsymbol{\mu}(\boldsymbol{\theta}) \approx \boldsymbol{\mu}^{\mathrm{fid}} + \sum_{i=1}^{n} \boldsymbol{\mu}_{,i}^{\mathrm{fid}} (\theta_i - \theta_i^{\mathrm{fid}}), \tag{4.15}$$

where we define $\boldsymbol{\mu}^{\mathrm{fid}} = \boldsymbol{\mu}(\boldsymbol{\theta}^{\mathrm{fid}})$. In the Gaussian linear model, the Jacobian $\boldsymbol{\mu}_{,i}$

may be taken as constant over changes in $\boldsymbol{\theta}$ and so $\boldsymbol{\mu}_{,i}^{\rm fid}$ is approximately equal to $\boldsymbol{\mu}_{,i}^{\rm ML}$. For simplicity, from here on, we just drop all the superscripts for $\boldsymbol{\mu}_{,i}$. In practice, the fiducial model is usually based on to the ML model given by the data and updated iteratively if necessary.

Next, we move on to calculate the elements in parameter covariance $\mathbf{\Sigma}$:

$$\mathbf{\Sigma}_{ij} = (\mathcal{F}^{-1})_{ij}. \tag{4.16}$$

Remember that for any invertible square matrix $\mathcal{M}$, its inverse can be calculated as

$$(\mathcal{M}^{-1})_{ij} = (-1)^{i+j} \frac{|\mathcal{M}_{\backslash j \backslash i}|}{|\mathcal{M}|} \tag{4.17}$$

where $|\mathcal{M}|$ is the determinant of $\mathcal{M}$. We use the notation "$\mathcal{M}_{\backslash j \backslash i}$", to denote a smaller matrix, corresponding to $\mathcal{M}$ with the $j^{\rm th}$ row and the $i^{\rm th}$ column removed (the backslash symbol is borrowed from the notation for set difference in set theory). Then $|\mathcal{M}_{\backslash j \backslash i}|$ is a minor of $\mathcal{M}$. And the determinant for an $n \times n$ matrix $\mathcal{M}$ can be written as

$$|\mathcal{M}| = \sum_{i=1}^{n} (-1)^{i+j} \mathcal{M}_{ij} |\mathcal{M}_{\backslash i \backslash j}| \tag{4.18}$$

for any $1 \leq j \leq n$.

Therefore

$$\mathbf{\Sigma}_{ij} = (-1)^{i+j} |\mathcal{F}_{\backslash j \backslash i}| / |\mathcal{F}|. \tag{4.19}$$

If we choose to fix the $i^{\rm th}$ parameter, we can simply remove the $i^{\rm th}$ row and column from the Fisher matrix, and calculate a new parameter covariance matrix from the revised Fisher matrix.

4.6.2.2 Correlation Between Parameter A and B, Varying Together

When two parameters A and B are both variables, we can calculate their covariance from the Fisher matrix that includes them along with the base ΛCDM parameters. So their correlation is just

$$corr(A, B) = \frac{\mathbf{\Sigma}_{AB}}{(\mathbf{\Sigma}_{AA}\mathbf{\Sigma}_{BB})^{\frac{1}{2}}}. \tag{4.20}$$

From here on, for clarity, we use A and B as subscripts for the rows and columns in the matrix for the two parameters of interest.

Following from equation (B9), (B10) becomes

$$corr(A, B) = \frac{-|\mathcal{F}_{\backslash A \backslash B}|}{(|\mathcal{F}_{\backslash A \backslash A}||\mathcal{F}_{\backslash B \backslash B}|)^{\frac{1}{2}}}. \tag{4.21}$$

The minus sign is from setting the index of B equal to that of A plus one.

4.6.2.3 Correlation Between Parameter A and B, Varying Separately

For a generic set of parameters, given the data array $\boldsymbol{d}$ (experimental or simulated) and the Fisher matrix $\mathcal{F}$, we can substitute (B5) into (B2) to obtain a relationship between the ML parameters $\boldsymbol{\theta}^{\rm ML}$ and the fiducial ones:

$$\boldsymbol{\theta}^{\rm ML}(\boldsymbol{d}) - \boldsymbol{\theta}^{\rm fid} = \mathcal{F}^{-1}\boldsymbol{\mu}_{,i}^{T}\boldsymbol{\mathcal{C}}^{-1}(\boldsymbol{d} - \boldsymbol{\mu}). \tag{4.22}$$

So we can express $\boldsymbol{\theta}^{\rm ML}$ as:

$$\boldsymbol{\theta}^{\rm ML}(\boldsymbol{d}) = \mathcal{F}^{-1}\boldsymbol{\mu}_{,i}^{T}\boldsymbol{\mathcal{C}}^{-1}\boldsymbol{d} + \hat{\boldsymbol{\theta}}, \tag{4.23}$$

where we use the vector $\hat{\boldsymbol{\theta}}$ to represent all the terms in (B11) that are independent of data $\boldsymbol{d}$:

$$\hat{\boldsymbol{\theta}} \equiv -\mathcal{F}^{-1}\boldsymbol{\mu}_{,i}^{T}\boldsymbol{\mathcal{C}}^{-1}\boldsymbol{\mu}^{\rm fid} + \boldsymbol{\theta}^{\rm fid}.$$

As we will show below, $\hat{\boldsymbol{\theta}}$ does not contribute to the correlation between A and B.

Again for clarity, we use A and B to index the rows and columns for parameter A and B, respectively, while using the generic i and j to index n base ΛCDM parameters. So A is the $(n+1)^{\rm th}$ parameter and B $(n+2)^{\rm th}$.

When fixing B to its fiducial ΛCDM value $B^{\rm fid}$, the expression for the best estimate for other parameters is almost the same as equation (B12), except that $\mathcal{F} \to \mathcal{F}_{\backslash B\backslash B}$ and the elements associated with B in $\boldsymbol{\mu}_{,i}^{T}$, $\boldsymbol{\theta}^{\rm ML}$ and $\hat{\boldsymbol{\theta}}$ are deleted. The expression for the rest of elements in $\boldsymbol{\theta}^{\rm ML}$ is:

$$\begin{pmatrix} \boldsymbol{\theta}_1^{\rm ML} \\ \boldsymbol{\theta}_2^{\rm ML} \\ \vdots \\ \boldsymbol{\theta}_n^{\rm ML} \\ A^{\rm ML} \end{pmatrix} = (\mathcal{F}_{\backslash B\backslash B})^{-1} \begin{pmatrix} \boldsymbol{\mu}_{,1}^{T}\boldsymbol{\mathcal{C}}^{-1}\boldsymbol{d} \\ \boldsymbol{\mu}_{,2}^{T}\boldsymbol{\mathcal{C}}^{-1}\boldsymbol{d} \\ \vdots \\ \boldsymbol{\mu}_{,n}^{T}\boldsymbol{\mathcal{C}}^{-1}\boldsymbol{d} \\ \boldsymbol{\mu}_{,A}^{T}\boldsymbol{\mathcal{C}}^{-1}\boldsymbol{d} \end{pmatrix} + \hat{\boldsymbol{\theta}}. \tag{4.24}$$

The last row of (B14) gives

$$A^{\rm ML}(\boldsymbol{d}) = \tag{4.25}$$

$$\left[\sum_{i=1}^{n} (\mathcal{F}_{\backslash B\backslash B})_{Ai}^{-1}\boldsymbol{\mu}_{,i}^{T}\boldsymbol{\mathcal{C}}^{-1} + (\mathcal{F}_{\backslash B\backslash B})_{AA}^{-1}\boldsymbol{\mu}_{,A}^{T}\boldsymbol{\mathcal{C}}^{-1}\right]\boldsymbol{d} + \hat{\theta}_A.$$

Similarly, fixing A and letting B vary leads to

$$B^{\mathrm{ML}}(\boldsymbol{d}) = \tag{4.26}$$

$$\left[\sum_{i=1}^{n}(\mathcal{F}_{\backslash A\backslash A})^{-1}_{Bi}\boldsymbol{\mu}^{T}_{,i}\boldsymbol{\mathcal{C}}^{-1} + (\mathcal{F}_{\backslash A\backslash A})^{-1}_{BB}\boldsymbol{\mu}^{T}_{,B}\boldsymbol{\mathcal{C}}^{-1}\right]\boldsymbol{d} + \hat{\theta}_B.$$

The variance of A and B can be obtained from the Fisher matrix (B3) and its minors (B7), as follows:

$$Var(A^{\mathrm{ML}}) = (\mathcal{F}_{\backslash B\backslash B})^{-1}_{AA} = \frac{\left|\mathcal{F}_{\backslash B\backslash B}\right|_{\backslash A\backslash A}}{|\mathcal{F}_{\backslash B\backslash B}|} \tag{4.27}$$

$$Var(B^{\mathrm{ML}}) = (\mathcal{F}_{\backslash A\backslash A})^{-1}_{BB} = \frac{\left|\mathcal{F}_{\backslash A\backslash A}\right|_{\backslash B\backslash B}}{|\mathcal{F}_{\backslash A\backslash A}|}. \tag{4.28}$$

And the covariance between A^{ML} and B^{ML} is:

$$Cov(A^{\mathrm{ML}}, B^{\mathrm{ML}}) = \langle (A^{\mathrm{ML}} - \langle A^{\mathrm{ML}}\rangle)(B^{\mathrm{ML}} - \langle B^{\mathrm{ML}}\rangle)\rangle, \tag{4.29}$$

with the brackets here representing the averaging over all realizations of the data $\boldsymbol{d}$.

Recall that the data covariance $\boldsymbol{\mathcal{C}}$ is assumed to be fixed and with our assumption of a Gaussian Linear Model, all partial derivatives w.r.t. the parameters are also constant. Then in (B15) and (B16), only $\boldsymbol{d}$ is a variable. Inserting (B15) and (B16) into (B19), we find that terms involving $\hat{\theta}_A$ and $\hat{\theta}_B$ cancel. In addition, all constant terms can be taken out of the brackets, leaving

only $\langle(\boldsymbol{d}-\langle\boldsymbol{d}\rangle)^T(\boldsymbol{d}-\langle\boldsymbol{d}\rangle)\rangle$, which is just $\boldsymbol{\mathcal{C}}$. This simplifies to

$$
\begin{aligned}
&Cov(A^{\mathrm{ML}}, B^{\mathrm{ML}}) = \\
&\sum_{i,j=1}^{n} (\mathcal{F}_{\setminus B\setminus B})^{-1}_{Ai} \boldsymbol{\mu}_{,i}^T \boldsymbol{\mathcal{C}}^{-1} \boldsymbol{\mu}_{,j} (\mathcal{F}_{\setminus A\setminus A})^{-1}_{Bj} \\
&+ \sum_{i=1}^{n} (\mathcal{F}_{\setminus B\setminus B})^{-1}_{Ai} \boldsymbol{\mu}_{,i}^T \boldsymbol{\mathcal{C}}^{-1} \boldsymbol{\mu}_{,B} (\mathcal{F}_{\setminus A\setminus A})^{-1}_{BB} \\
&+ \sum_{i=1}^{n} (\mathcal{F}_{\setminus B\setminus B})^{-1}_{AA} \boldsymbol{\mu}_{,A}^T \boldsymbol{\mathcal{C}}^{-1} \boldsymbol{\mu}_{,i} (\mathcal{F}_{\setminus A\setminus A})^{-1}_{Bi} \\
&+ (\mathcal{F}_{\setminus B\setminus B})^{-1}_{AA} \boldsymbol{\mu}_{,A}^T \boldsymbol{\mathcal{C}}^{-1} \boldsymbol{\mu}_{,B} (\mathcal{F}_{\setminus A\setminus A})^{-1}_{BB}. \qquad (4.30)
\end{aligned}
$$

Notice that terms like $\boldsymbol{\mu}_{,i}^T \boldsymbol{\mathcal{C}}^{-1} \boldsymbol{\mu}_{,j}$ are just elements of the Fisher matrix and we can also use equation (B7) to express terms like $(\mathcal{F}_{\setminus B\setminus B})^{-1}_{Ai}$ in terms of

determinants of minors of the Fisher matrix. Thus,

$$Cov(A^{\mathrm{ML}}, B^{\mathrm{ML}}) = \frac{1}{|\mathcal{F}_{\setminus B\setminus B}||\mathcal{F}_{\setminus A\setminus A}|} \times$$

$$\Bigg[\underbrace{\sum_{i,j=1}^{n} (-1)^{i+n+1} \left|\mathcal{F}_{\substack{\setminus B\setminus B \\ \setminus i\setminus A}}\right| \mathcal{F}_{ij} (-1)^{j+n+1} \left|\mathcal{F}_{\substack{\setminus A\setminus A \\ \setminus j\setminus B}}\right|}_{[1]}$$

$$+ \underbrace{\sum_{i=1}^{n} (-1)^{i+n+1} \left|\mathcal{F}_{\substack{\setminus B\setminus B \\ \setminus i\setminus A}}\right| \mathcal{F}_{iB} \left|\mathcal{F}_{\substack{\setminus A\setminus A \\ \setminus B\setminus B}}\right|}_{[2]}$$

$$+ \underbrace{\sum_{i=1}^{n} \left|\mathcal{F}_{\substack{\setminus A\setminus A \\ \setminus B\setminus B}}\right| \mathcal{F}_{Ai} (-1)^{i+n+1} \left|\mathcal{F}_{\substack{\setminus A\setminus A \\ \setminus i\setminus B}}\right|}_{[3]}$$

$$+ \underbrace{\left|\mathcal{F}_{\substack{\setminus B\setminus B \\ \setminus A\setminus A}}\right| \mathcal{F}_{AB} \left|\mathcal{F}_{\substack{\setminus A\setminus A \\ \setminus B\setminus B}}\right|}_{[4]} \Bigg]. \tag{4.31}$$

To simplify (B21), first we combine term [1] and [2]:

$$
\begin{aligned}
& [1] + [2] \\
= & \sum_{i=1}^{n} (-1)^{i+n+1} \left| \mathcal{F}_{\substack{\setminus B \setminus B \\ \setminus i \setminus A}} \right| \times \\
& \left[\sum_{j=1}^{n} \mathcal{F}_{ij} (-1)^{j+n+1} \left| \mathcal{F}_{\substack{\setminus A \setminus A \\ \setminus j \setminus B}} \right| + \mathcal{F}_{iB} \left| \mathcal{F}_{\substack{\setminus A \setminus A \\ \setminus B \setminus B}} \right| \right] \\
= & \sum_{i=1}^{n} (-1)^{i+n+1} \left| \mathcal{F}_{\substack{\setminus B \setminus B \\ \setminus i \setminus A}} \right| \times \\
& \left[\sum_{j=1}^{n} \mathcal{F}_{ji} (-1)^{(n+1)+j} \left| \mathcal{F}_{\substack{\setminus A \setminus A \\ \setminus j \setminus B}} \right| + \mathcal{F}_{Bi} (-1)^{2\times(n+1)} \left| \mathcal{F}_{\substack{\setminus A \setminus A \\ \setminus B \setminus B}} \right| \right]
\end{aligned}
$$

where we have used the property that the Fisher matrix is symmetric.

Compared to equation (B8), note that the terms inside the last bracket above sum up to the determinant of an $(n+1) \times (n+1)$ matrix, which is the same as $\mathcal{F}_{\setminus A \setminus A}$, except that its $(n+1)^{\text{th}}$ column is replaced by its i^{th}. So not all of the columns for this matrix are linearly independent, resulting in its determinant being zero. Thus $[1] + [2] = 0$.

To simplify term [3] and [4], we have

$$\begin{aligned}
& [3] + [4] \\
= & \left|\mathcal{F}_{\substack{\setminus A\setminus A \\ \setminus B\setminus B}}\right| \left[\sum_{i=1}^{n} \mathcal{F}_{Ai}(-1)^{i+n+1} \left|\mathcal{F}_{\substack{\setminus A\setminus A \\ \setminus i\setminus B}}\right| + \mathcal{F}_{AB} \left|\mathcal{F}_{\substack{\setminus A\setminus A \\ \setminus B\setminus B}}\right| \right] \\
= & \left|\mathcal{F}_{\substack{\setminus A\setminus A \\ \setminus B\setminus B}}\right| \left[\sum_{i=1}^{n} \mathcal{F}_{iA}(-1)^{i+n+1} \left|\mathcal{F}_{\substack{\setminus A\setminus B \\ \setminus i\setminus A}}\right| + \mathcal{F}_{BA} \left|\mathcal{F}_{\substack{\setminus A\setminus B \\ \setminus B\setminus A}}\right| \right] \\
= & \left|\mathcal{F}_{\substack{\setminus A\setminus A \\ \setminus B\setminus B}}\right| \left|\mathcal{F}_{\setminus A\setminus B}\right| \qquad (4.32)
\end{aligned}$$

Insertng (4.32) into (4.31), we have

$$Cov(A^{\mathrm{ML}}, B^{\mathrm{ML}}) = \frac{\left|\mathcal{F}_{\substack{\setminus A\setminus A \\ \setminus B\setminus B}}\right| \left|\mathcal{F}_{\setminus A\setminus B}\right|}{|\mathcal{F}_{\setminus B\setminus B}||\mathcal{F}_{\setminus A\setminus A}|}. \qquad (4.33)$$

Using Equation (4.27) and (4.28), the correlation between the best-fit values of parameter A and B estimated separately can be written as

$$\begin{aligned}
corr(A^{\mathrm{ML}}, B^{\mathrm{ML}}) &= \frac{Cov(A^{\mathrm{ML}}, B^{\mathrm{ML}})}{(Var(A^{\mathrm{ML}}) \times Var(B^{\mathrm{ML}}))^{\frac{1}{2}}} \\
&= \frac{\left|\mathcal{F}_{\substack{\setminus A\setminus A \\ \setminus B\setminus B}}\right| \left|\mathcal{F}_{\setminus A\setminus B}\right|}{|\mathcal{F}_{\setminus B\setminus B}||\mathcal{F}_{\setminus A\setminus A}|} \frac{(|\mathcal{F}_{\setminus B\setminus B}||\mathcal{F}_{\setminus A\setminus A}|)^{\frac{1}{2}}}{\left|\mathcal{F}_{\substack{\setminus A\setminus A \\ \setminus B\setminus B}}\right|} \\
&= \frac{|\mathcal{F}_{\setminus A\setminus B}|}{(|\mathcal{F}_{\setminus A\setminus A}||\mathcal{F}_{\setminus B\setminus B}|)^{\frac{1}{2}}}, \qquad (4.34)
\end{aligned}$$

which is the same as equation (4.21) up to a minus sign, thus completing our

proof.

References

Abbott, T. M. C. et al. (2019). "First Cosmology Results using Type Ia Supernovae from the Dark Energy Survey: Constraints on Cosmological Parameters". In: *APJL* 872.2, L30, p. L30. DOI: 10.3847/2041-8213/ab04fa. arXiv: 1811.02374 [astro-ph.CO].

Addison, G. E., Y. Huang, D. J. Watts, C. L. Bennett, M. Halpern, G. Hinshaw, and J. L. Weiland (2016). "Quantifying Discordance in the 2015 Planck CMB Spectrum". In: *APJ* 818, 132, p. 132. DOI: 10.3847/0004-637X/818/2/132. arXiv: 1511.00055.

Addison, G. E., D. J. Watts, C. L. Bennett, M. Halpern, G. Hinshaw, and J. L. Weiland (2018). "Elucidating ΛCDM: Impact of Baryon Acoustic Oscillation Measurements on the Hubble Constant Discrepancy". In: *APJ* 853, 119, p. 119. DOI: 10.3847/1538-4357/aaa1ed. arXiv: 1707.06547 [astro-ph.CO].

Alam, Shadab, Metin Ata, Stephen Bailey, Florian Beutler, Dmitry Bizyaev, Jonathan A. Blazek, Adam S. Bolton, Joel R. Brownstein, Angela Burden, Chia-Hsun Chuang, Johan Comparat, Antonio J. Cuesta, Kyle S. Dawson, Daniel J. Eisenstein, Stephanie Escoffier, Héctor Gil-Marín, Jan Niklas Grieb, Nick Hand, Shirley Ho, Karen Kinemuchi, David Kirkby, Francisco Kitaura, Elena Malanushenko, Viktor Malanushenko, Claudia Maraston, Cameron K. McBride, Robert C. Nichol, Matthew D. Olmstead, Daniel Oravetz, Nikhil Padmanabhan, Nathalie Palanque-Delabrouille, Kaike Pan, Marcos Pellejero-Ibanez, Will J. Percival, Patrick Petitjean, Francisco Prada, Adrian M. Price-Whelan, Beth A. Reid, Sergio A. Rodríguez-Torres, Natalie A. Roe, Ashley J. Ross, Nicholas P. Ross, Graziano Rossi, Jose Alberto Rubiño-Martín, Shun Saito, Salvador Salazar-Albornoz, Lado Samushia, Ariel G. Sánchez, Siddharth Satpathy, David J. Schlegel, Donald P. Schneider, Claudia G. Scóccola, Hee-Jong Seo, Erin S. Sheldon, Audrey Simmons, Anže Slosar, Michael A. Strauss, Molly E. C. Swanson, Daniel Thomas, Jeremy L. Tinker, Rita Tojeiro, Mariana Vargas Magaña, Jose

Alberto Vazquez, Licia Verde, David A. Wake, Yuting Wang, David H. Weinberg, Martin White, W. Michael Wood-Vasey, Christophe Yèche, Idit Zehavi, Zhongxu Zhai, and Gong-Bo Zhao (2017). "The clustering of galaxies in the completed SDSS-III Baryon Oscillation Spectroscopic Survey: cosmological analysis of the DR12 galaxy sample". In: *MNRAS* 470, pp. 2617–2652. DOI: 10.1093/mnras/stx721. arXiv: 1607.03155 [astro-ph.CO].

Bennett, C. L., D. Larson, J. L. Weiland, N. Jarosik, G. Hinshaw, N. Odegard, K. M. Smith, R. S. Hill, B. Gold, M. Halpern, E. Komatsu, M. R. Nolta, L. Page, D. N. Spergel, E. Wollack, J. Dunkley, A. Kogut, M. Limon, S. S. Meyer, G. S. Tucker, and E. L. Wright (2013). "Nine-year Wilkinson Microwave Anisotropy Probe (WMAP) Observations: Final Maps and Results". In: *APJS* 208, 20, p. 20. DOI: 10.1088/0067-0049/208/2/20. arXiv: 1212.5225.

BICEP2 Collaboration, Keck Array Collaboration, P. A. R. Ade, Z. Ahmed, R. W. Aikin, K. D. Alexander, D. Barkats, S. J. Benton, C. A. Bischoff, J. J. Bock, R. Bowens-Rubin, J. A. Brevik, I. Buder, E. Bullock, V. Buza, J. Connors, J. Cornelison, B. P. Crill, M. Crumrine, M. Dierickx, L. Duband, C. Dvorkin, J. P. Filippini, S. Fliescher, J. Grayson, G. Hall, M. Halpern, S. Harrison, S. R. Hildebrandt, G. C. Hilton, H. Hui, K. D. Irwin, J. Kang, K. S. Karkare, E. Karpel, J. P. Kaufman, B. G. Keating, S. Kefeli, S. A. Kernasovskiy, J. M. Kovac, C. L. Kuo, N. A. Larsen, K. Lau, E. M. Leitch, M. Lueker, K. G. Megerian, L. Moncelsi, T. Namikawa, C. B. Netterfield, H. T. Nguyen, R. O'Brient, R. W. Ogburn, S. Palladino, C. Pryke, B. Racine, S. Richter, A. Schillaci, R. Schwarz, C. D. Sheehy, A. Soliman, T. St. Germaine, Z. K. Staniszewski, B. Steinbach, R. V. Sudiwala, G. P. Teply, K. L. Thompson, J. E. Tolan, C. Tucker, A. D. Turner, C. Umiltà, A. G. Vieregg, A. Wandui, A. C. Weber, D. V. Wiebe, J. Willmert, C. L. Wong, W. L. K. Wu, H. Yang, K. W. Yoon, and C. Zhang (2018). "Constraints on Primordial Gravitational Waves Using Planck, WMAP, and New BICEP2/Keck Observations through the 2015 Season". In: *Physical Review Letters* 121.22, 221301, p. 221301. DOI: 10.1103/PhysRevLett.121.221301. arXiv: 1810.05216.

Birrer, S., T. Treu, C. E. Rusu, V. Bonvin, C. D. Fassnacht, J. H. H. Chan, A. Agnello, A. J. Shajib, G. C. F. Chen, M. Auger, F. Courbin, S. Hilbert, D. Sluse, S. H. Suyu, K. C. Wong, P. Marshall, B. C. Lemaux, and G. Meylan (2019). "H0LiCOW - IX. Cosmographic analysis of the doubly imaged quasar SDSS 1206+4332 and a new measurement of the Hubble constant". In: *MNRAS* 484, pp. 4726–4753. DOI: 10.1093/mnras/stz200. arXiv: 1809.01274 [astro-ph.CO].

Bonvin, V., F. Courbin, S. H. Suyu, P. J. Marshall, C. E. Rusu, D. Sluse, M. Tewes, K. C. Wong, T. Collett, C. D. Fassnacht, T. Treu, M. W. Auger, S. Hilbert, L. V. E. Koopmans, G. Meylan, N. Rumbaugh, A. Sonnenfeld, and C. Spiniello (2017). "H0LiCOW - V. New COSMOGRAIL time delays of HE 0435-1223: H_0 to 3.8 per cent precision from strong lensing in a flat ΛCDM model". In: *MNRAS* 465, pp. 4914–4930. DOI: 10.1093/mnras/stw3006. arXiv: 1607.01790 [astro-ph.CO].

Box, G. E. P. and D. R. Cox (1964). "An analysis of transformations". In: *Journal of the Royal Statistical Society. Series B (Methodological*, pp. 211–252.

Calabrese, Erminia, An že Slosar, Alessandro Melchiorri, George F. Smoot, and Oliver Zahn (2008). "Cosmic microwave weak lensing data as a test for the dark universe". In: *Phys. Rev. D* 77 (12), p. 123531. DOI: 10.1103/PhysRevD.77.123531. URL: https://link.aps.org/doi/10.1103/PhysRevD.77.123531.

Gelman, A., J.B. Carlin, H.S. Stern, D.B. Dunson, A. Vehtari, and D.B. Rubin (2013). *Bayesian Data Analysis, Third Edition*. Chapman & Hall/CRC Texts in Statistical Science. Taylor & Francis. ISBN: 9781439840955. URL: https://books.google.com/books?id=ZXL6AQAAQBAJ.

Hamimeche, Samira and Antony Lewis (2008). "Likelihood analysis of CMB temperature and polarization power spectra". In: *Phys. Rev. D* 77 (10), p. 103013. DOI: 10.1103/PhysRevD.77.103013. URL: https://link.aps.org/doi/10.1103/PhysRevD.77.103013.

Heavens, Alan (2009). "Statistical techniques in cosmology". In: *arXiv e-prints*, arXiv:0906.0664, arXiv:0906.0664. arXiv: 0906.0664 [astro-ph.CO].

Heavens, Alan, Yabebal Fantaye, Elena Sellentin, Hans Eggers, Zafiirah Hosenie, Steve Kroon, and Arrykrishna Mootoovaloo (2017). "No Evidence for Extensions to the Standard Cosmological Model". In: *PRL* 119, 101301, p. 101301. DOI: 10.1103/PhysRevLett.119.101301. arXiv: 1704.03467 [astro-ph.CO].

Henning, J. W., J. T. Sayre, C. L. Reichardt, P. A. R. Ade, A. J. Anderson, J. E. Austermann, J. A. Beall, A. N. Bender, B. A. Benson, L. E. Bleem, J. E. Carlstrom, C. L. Chang, H. C. Chiang, H. M. Cho, R. Citron, C. Corbett Moran, T. M. Crawford, A. T. Crites, T. de Haan, M. A. Dobbs, W. Everett, J. Gallicchio, E. M. George, A. Gilbert, N. W. Halverson, N. Harrington, G. C. Hilton, G. P. Holder, W. L. Holzapfel, S. Hoover, Z. Hou, J. D. Hrubes, N. Huang, J. Hubmayr, K. D. Irwin, R. Keisler, L. Knox, A. T. Lee, E. M. Leitch, D. Li, A. Lowitz, A. Manzotti, J. J. McMahon, S. S. Meyer, L. Mocanu, J. Montgomery, A. Nadolski, T. Natoli, J. P. Nibarger, V. Novosad,

S. Padin, C. Pryke, J. E. Ruhl, B. R. Saliwanchik, K. K. Schaffer, C. Sievers, G. Smecher, A. A. Stark, K. T. Story, C. Tucker, K. Vanderlinde, T. Veach, J. D. Vieira, G. Wang, N. Whitehorn, W. L. K. Wu, and V. Yefremenko (2018). "Measurements of the Temperature and E-mode Polarization of the CMB from 500 Square Degrees of SPTpol Data". In: *APJ* 852, 97, p. 97. DOI: 10.3847/1538-4357/aa9ff4. arXiv: 1707.09353 [astro-ph.CO].

Hikage, Chiaki, Masamune Oguri, Takashi Hamana, Surhud More, Rachel Mandelbaum, Masahiro Takada, Fabian Köhlinger, Hironao Miyatake, Atsushi J. Nishizawa, Hiroaki Aihara, Robert Armstrong, James Bosch, Jean Coupon, Anne Ducout, Paul Ho, Bau-Ching Hsieh, Yutaka Komiyama, François Lanusse, Alexie Leauthaud, Robert H. Lupton, Elinor Medezinski, Sogo Mineo, Shoken Miyama, Satoshi Miyazaki, Ryoma Murata, Hitoshi Murayama, Masato Shirasaki, Cristóbal Sifón, Melanie Simet, Joshua Speagle, David N. Spergel, Michael A. Strauss, Naoshi Sugiyama, Masayuki Tanaka, Yousuke Utsumi, Shiang-Yu Wang, and Yoshihiko Yamada (2019). "Cosmology from cosmic shear power spectra with Subaru Hyper Suprime-Cam first-year data". In: *Publications of the Astronomical Society of Japan*, p. 22. DOI: 10.1093/pasj/psz010. arXiv: 1809.09148 [astro-ph.CO].

Joachimi, B. and A. N. Taylor (2011). "Forecasts of non-Gaussian parameter spaces using Box-Cox transformations". In: *MNRAS* 416, pp. 1010–1022. DOI: 10.1111/j.1365-2966.2011.19107.x. arXiv: 1103.3370 [astro-ph.CO].

Joudaki, Shahab, Alexander Mead, Chris Blake, Ami Choi, Jelte de Jong, Thomas Erben, Ian Fenech Conti, Ricardo Herbonnet, Catherine Heymans, Hendrik Hildebrandt, Henk Hoekstra, Benjamin Joachimi, Dominik Klaes, Fabian Köhlinger, Konrad Kuijken, John McFarland, Lance Miller, Peter Schneider, and Massimo Viola (2017). "KiDS-450: testing extensions to the standard cosmological model". In: *MNRAS* 471, pp. 1259–1279. DOI: 10.1093/mnras/stx998. arXiv: 1610.04606 [astro-ph.CO].

Kable, Joshua A., Graeme E. Addison, and Charles L. Bennett (2019). "Quantifying the CMB Degeneracy between the Matter Density and Hubble Constant in Current Experiments". In: *APJ* 871.1, 77, p. 77. DOI: 10.3847/1538-4357/aaf56d. arXiv: 1809.03983 [astro-ph.CO].

Krause, E., T. F. Eifler, J. Zuntz, O. Friedrich, M. A. Troxel, S. Dodelson, J. Blazek, L. F. Secco, N. MacCrann, E. Baxter, C. Chang, N. Chen, M. Crocce, J. DeRose, A. Ferte, N. Kokron, F. Lacasa, V. Miranda, Y. Omori, A. Porredon, R. Rosenfeld, S. Samuroff, M. Wang, R. H. Wechsler, T. M. C. Abbott, F. B. Abdalla, S. Allam, J. Annis, K. Bechtol, A. Benoit-Levy, G. M. Bernstein,

D. Brooks, D. L. Burke, D. Capozzi, M. Carrasco Kind, J. Carretero, C. B. D'Andrea, L. N. da Costa, C. Davis, D. L. DePoy, S. Desai, H. T. Diehl, J. P. Dietrich, A. E. Evrard, B. Flaugher, P. Fosalba, J. Frieman, J. Garcia-Bellido, E. Gaztanaga, T. Giannantonio, D. Gruen, R. A. Gruendl, J. Gschwend, G. Gutierrez, K. Honscheid, D. J. James, T. Jeltema, K. Kuehn, S. Kuhlmann, O. Lahav, M. Lima, M. A. G. Maia, M. March, J. L. Marshall, P. Martini, F. Menanteau, R. Miquel, R. C. Nichol, A. A. Plazas, A. K. Romer, E. S. Rykoff, E. Sanchez, V. Scarpine, R. Schindler, M. Schubnell, I. Sevilla-Noarbe, M. Smith, M. Soares-Santos, F. Sobreira, E. Suchyta, M. E. C. Swanson, G. Tarle, D. L. Tucker, V. Vikram, A. R. Walker, and J. Weller (2017). "Dark Energy Survey Year 1 Results: Multi-Probe Methodology and Simulated Likelihood Analyses". In: *ArXiv e-prints*. arXiv: 1706.09359.

Kreisch, Christina D., Francis-Yan Cyr-Racine, and Olivier Doré (2019). "The Neutrino Puzzle: Anomalies, Interactions, and Cosmological Tensions". In: *arXiv e-prints*, arXiv:1902.00534, arXiv:1902.00534. arXiv: 1902.00534 [astro-ph.CO].

Lewis, A. and S. Bridle (2002). "Cosmological parameters from CMB and other data: A Monte Carlo approach". In: *PRD* 66.10, 103511, p. 103511. DOI: 10.1103/PhysRevD.66.103511. eprint: astro-ph/0205436.

Louis, Thibaut, Emily Grace, Matthew Hasselfield, Marius Lungu, Loïc Maurin, Graeme E. Addison, Peter A. R. Ade, Simone Aiola, Rupert Allison, Mandana Amiri, Elio Angile, Nicholas Battaglia, James A. Beall, Francesco de Bernardis, J. Richard Bond, Joe Britton, Erminia Calabrese, Hsiao-mei Cho, Steve K. Choi, Kevin Coughlin, Devin Crichton, Kevin Crowley, Rahul Datta, Mark J. Devlin, Simon R. Dicker, Joanna Dunkley, Rolando Dünner, Simone Ferraro, Anna E. Fox, Patricio Gallardo, Megan Gralla, Mark Halpern, Shawn Henderson, J. Colin Hill, Gene C. Hilton, Matt Hilton, Adam D. Hincks, Renée Hlozek, S. P. Patty Ho, Zhiqi Huang, Johannes Hubmayr, Kevin M. Huffenberger, John P. Hughes, Leopoldo Infante, Kent Irwin, Simon Muya Kasanda, Jeff Klein, Brian Koopman, Arthur Kosowsky, Dale Li, Mathew Madhavacheril, Tobias A. Marriage, Jeff McMahon, Felipe Menanteau, Kavilan Moodley, Charles Munson, Sigurd Naess, Federico Nati, Laura Newburgh, John Nibarger, Michael D. Niemack, Michael R. Nolta, Carolina Nuñez, Lyman A. Page, Christine Pappas, Bruce Partridge, Felipe Rojas, Emmanuel Schaan, Benjamin L. Schmitt, Neelima Sehgal, Blake D. Sherwin, Jon Sievers, Sara Simon, David N. Spergel, Suzanne T. Staggs, Eric R. Switzer, Robert Thornton, Hy Trac, Jesse Treu, Carole Tucker, Alexander Van Engelen, Jonathan T. Ward, and Edward J. Wollack

(2017). "The Atacama Cosmology Telescope: two-season ACTPol spectra and parameters". In: *JCAP* 2017.6, 031, p. 031. DOI: 10.1088/1475-7516/2017/06/031. arXiv: 1610.02360 [astro-ph.CO].

Motloch, Pavel and Wayne Hu (2018). "Tensions between direct measurements of the lens power spectrum from Planck data". In: *PRD* 97, 103536, p. 103536. DOI: 10.1103/PhysRevD.97.103536. arXiv: 1803.11526 [astro-ph.CO].

Motloch, Pavel and Wayne Hu (2019a). "Lensing covariance on cut sky and SPT -P l a n c k lensing tensions". In: *PRD* 99, 023506, p. 023506. DOI: 10.1103/PhysRevD.99.023506. arXiv: 1810.09347 [astro-ph.CO].

Motloch, Pavel and Wayne Hu (2019b). "Lensing covariance on cut sky and SPT -P l a n c k lensing tensions". In: *PRD* 99, 023506, p. 023506. DOI: 10.1103/PhysRevD.99.023506. arXiv: 1810.09347 [astro-ph.CO].

Percival, Will J., Ashley J. Ross, Ariel G. Sánchez, Lado Samushia, Angela Burden, Robert Crittenden, Antonio J. Cuesta, Mariana Vargas Magana, Marc Manera, Florian Beutler, Chia-Hsun Chuang, Daniel J. Eisenstein, Shirley Ho, Cameron K. McBride, Francesco Montesano, Nikhil Padmanabhan, Beth Reid, Shun Saito, Donald P. Schneider, Hee-Jong Seo, Rita Tojeiro, and Benjamin A. Weaver (2014). "The clustering of Galaxies in the SDSS-III Baryon Oscillation Spectroscopic Survey: including covariance matrix errors". In: *MNRAS* 439.3, pp. 2531–2541. DOI: 10.1093/mnras/stu112. arXiv: 1312.4841 [astro-ph.CO].

Percival, Will J., Will Sutherland, John A. Peacock, Carlton M. Baugh, Joss Bland-Hawthorn, Terry Bridges, Russell Cannon, Shaun Cole, Matthew Colless, Chris Collins, Warrick Couch, Gavin Dalton, Roberto De Propris, Simon P. Driver, George Efstathiou, Richard S. Ellis, Carlos S. Frenk, Karl Glazebrook, Carole Jackson, Ofer Lahav, Ian Lewis, Stuart Lumsden, Steve Maddox, Stephen Moody, Peder Norberg, Bruce A. Peterson, and Keith Taylor (2002). "Parameter constraints for flat cosmologies from cosmic microwave background and 2dFGRS power spectra". In: *MNRAS* 337, pp. 1068–1080. DOI: 10.1046/j.1365-8711.2002.06001.x. arXiv: astro-ph/0206256 [astro-ph].

Planck Collaboration VI (2018). "Planck 2018 results. VI. Cosmological parameters". In: *ArXiv e-prints*. arXiv: 1807.06209.

Planck Collaboration XI (2016). "Planck 2015 results. XI. CMB power spectra, likelihoods, and robustness of parameters". In: *AAP* 594, A11, A11. DOI: 10.1051/0004-6361/201526926. arXiv: 1507.02704.

Planck Collaboration XIII (2016). "Planck 2015 results. XIII. Cosmological parameters". In: *AAP* 594, A13, A13. DOI: 10.1051/0004-6361/201525830. arXiv: 1502.01589.

Planck Collaboration XVI (2014). "Planck 2013 results. XVI. Cosmological parameters". In: *AAP* 571, A16, A16. DOI: 10.1051/0004-6361/201321591. arXiv: 1303.5076.

Poulin, Vivian, Tristan L. Smith, Tanvi Karwal, and Marc Kamionkowski (2019). "Early Dark Energy can Resolve the Hubble Tension". In: *PRL* 122.22, 221301, p. 221301. DOI: 10.1103/PhysRevLett.122.221301. arXiv: 1811.04083 [astro-ph.CO].

Raveri, Marco and Wayne Hu (2019). "Concordance and discordance in cosmology". In: *PRD* 99.4, 043506, p. 043506. DOI: 10.1103/PhysRevD.99.043506. arXiv: 1806.04649 [astro-ph.CO].

Riess, Adam G., Stefano Casertano, Wenlong Yuan, Lucas M. Macri, and Dan Scolnic (2019). "Large Magellanic Cloud Cepheid Standards Provide a 1% Foundation for the Determination of the Hubble Constant and Stronger Evidence for Physics beyond ΛCDM". In: *APJ* 876.1, 85, p. 85. DOI: 10.3847/1538-4357/ab1422. arXiv: 1903.07603 [astro-ph.CO].

Riess, Adam G., Lucas M. Macri, Samantha L. Hoffmann, Dan Scolnic, Stefano Casertano, Alexei V. Filippenko, Brad E. Tucker, Mark J. Reid, David O. Jones, Jeffrey M. Silverman, Ryan Chornock, Peter Challis, Wenlong Yuan, Peter J. Brown, and Ryan J. Foley (2016). "A 2.4% Determination of the Local Value of the Hubble Constant". In: *APJ* 826, 56, p. 56. DOI: 10.3847/0004-637X/826/1/56. arXiv: 1604.01424 [astro-ph.CO].

Schuhmann, Robert L., Benjamin Joachimi, and Hiranya V. Peiris (2016). "Gaussianization for fast and accurate inference from cosmological data". In: *MNRAS* 459, pp. 1916–1928. DOI: 10.1093/mnras/stw738. arXiv: 1510.00019 [astro-ph.CO].

Scolnic, D. M., D. O. Jones, A. Rest, Y. C. Pan, R. Chornock, R. J. Foley, M. E. Huber, R. Kessler, G. Narayan, A. G. Riess, S. Rodney, E. Berger, D. J. Brout, P. J. Challis, M. Drout, D. Finkbeiner, R. Lunnan, R. P. Kirshner, N. E. Sanders, E. Schlafly, S. Smartt, C. W. Stubbs, J. Tonry, W. M. Wood-Vasey, M. Foley, J. Hand, E. Johnson, W. S. Burgett, K. C. Chambers, P. W. Draper, K. W. Hodapp, N. Kaiser, R. P. Kudritzki, E. A. Magnier, N. Metcalfe, F. Bresolin, E. Gall, R. Kotak, M. McCrum, and K. W. Smith (2018). "The Complete Light-curve Sample of Spectroscopically Confirmed SNe Ia from Pan-STARRS1 and Cosmological Constraints from the Combined Pantheon

Sample". In: *APJ* 859, 101, p. 101. DOI: 10.3847/1538-4357/aab9bb. arXiv: 1710.00845 [astro-ph.CO].

Sellentin, E., M. Quartin, and L. Amendola (2014). "Breaking the spell of Gaussianity: forecasting with higher order Fisher matrices". In: *MNRAS* 441, pp. 1831–1840. DOI: 10.1093/mnras/stu689. arXiv: 1401.6892.

Sievers, Jonathan L., Renée A. Hlozek, Michael R. Nolta, Viviana Acquaviva, Graeme E. Addison, Peter A. R. Ade, Paula Aguirre, Mandana Amiri, John William Appel, L. Felipe Barrientos, Elia S. Battistelli, Nick Battaglia, J. Richard Bond, Ben Brown, Bryce Burger, Erminia Calabrese, Jay Chervenak, Devin Crichton, Sudeep Das, Mark J. Devlin, Simon R. Dicker, W. Bertrand Doriese, Joanna Dunkley, Rolando Dünner, Thomas Essinger-Hileman, David Faber, Ryan P. Fisher, Joseph W. Fowler, Patricio Gallardo, Michael S. Gordon, Megan B. Gralla, Amir Hajian, Mark Halpern, Matthew Hasselfield, Carlos Hernández-Monteagudo, J. Colin Hill, Gene C. Hilton, Matt Hilton, Adam D. Hincks, Dave Holtz, Kevin M. Huffenberger, David H. Hughes, John P. Hughes, Leopoldo Infante, Kent D. Irwin, David R. Jacobson, Brittany Johnstone, Jean Baptiste Juin, Madhuri Kaul, Jeff Klein, Arthur Kosowsky, Judy M. Lau, Michele Limon, Yen-Ting Lin, Thibaut Louis, Robert H. Lupton, Tobias A. Marriage, Danica Marsden, Krista Martocci, Phil Mauskopf, Michael McLaren, Felipe Menanteau, Kavilan Moodley, Harvey Moseley, Calvin B. Netterfield, Michael D. Niemack, Lyman A. Page, William A. Page, Lucas Parker, Bruce Partridge, Reed Plimpton, Hernan Quintana, Erik D. Reese, Beth Reid, Felipe Rojas, Neelima Sehgal, Blake D. Sherwin, Benjamin L. Schmitt, David N. Spergel, Suzanne T. Staggs, Omelan Stryzak, Daniel S. Swetz, Eric R. Switzer, Robert Thornton, Hy Trac, Carole Tucker, Masao Uehara, Katerina Visnjic, Ryan Warne, Grant Wilson, Ed Wollack, Yue Zhao, and Caroline Zunckel (2013). "The Atacama Cosmology Telescope: cosmological parameters from three seasons of data". In: *JCAP* 2013.10, 060, p. 060. DOI: 10.1088/1475-7516/2013/10/060. arXiv: 1301.0824 [astro-ph.CO].

Story, K. T., C. L. Reichardt, Z. Hou, R. Keisler, K. A. Aird, B. A. Benson, L. E. Bleem, J. E. Carlstrom, C. L. Chang, H. M. Cho, T. M. Crawford, A. T. Crites, T. de Haan, M. A. Dobbs, J. Dudley, B. Follin, E. M. George, N. W. Halverson, G. P. Holder, W. L. Holzapfel, S. Hoover, J. D. Hrubes, M. Joy, L. Knox, A. T. Lee, E. M. Leitch, M. Lueker, D. Luong-Van, J. J. McMahon, J. Mehl, S. S. Meyer, M. Millea, J. J. Mohr, T. E. Montroy, S. Padin, T. Plagge, C. Pryke, J. E. Ruhl, J. T. Sayre, K. K. Schaffer, L. Shaw, E. Shirokoff, H. G. Spieler, Z. Staniszewski, A. A. Stark, A. van Engelen, K. Vand erlinde, J. D.

Vieira, R. Williamson, and O. Zahn (2013). "A Measurement of the Cosmic Microwave Background Damping Tail from the 2500-Square-Degree SPT-SZ Survey". In: *APJ* 779.1, 86, p. 86. DOI: 10.1088/0004-637X/779/1/86. arXiv: 1210.7231 [astro-ph.CO].

Wright, Angus H., Hendrik Hildebrandt, Konrad Kuijken, Thomas Erben, Robert Blake, Hugo Buddelmeijer, Ami Choi, Nicholas Cross, Jelte T. A. de Jong, Alastair Edge, Carlos Gonzalez-Fernandez, Eduardo González Solares, Aniello Grado, Catherine Heymans, Mike Irwin, Aybuke Kupcu Yoldas, James R. Lewis, Robert G. Mann, Nicola Napolitano, Mario Radovich, Peter Schneider, Cristóbal Sifón, William Sutherland, Eckhard Sutorius, and Gijs A. Verdoes Kleijn (2018). "KiDS+VIKING-450: A new combined optical & near-IR dataset for cosmology and astrophysics". In: *arXiv e-prints*, arXiv:1812.06077, arXiv:1812.06077. arXiv: 1812.06077 [astro-ph.CO].

Zaldarriaga, Matias, David N. Spergel, and Uroš Seljak (1997). "Microwave Background Constraints on Cosmological Parameters". In: *APJ* 488, pp. 1–13. DOI: 10.1086/304692. arXiv: astro-ph/9702157 [astro-ph].

Zhao, Gong-Bo, Marco Raveri, Levon Pogosian, Yuting Wang, Robert G. Crittenden, Will J. Handley, Will J. Percival, Florian Beutler, Jonathan Brinkmann, Chia-Hsun Chuang, Antonio J. Cuesta, Daniel J. Eisenstein, Francisco-Shu Kitaura, Kazuya Koyama, Benjamin L'Huillier, Robert C. Nichol, Matthew M. Pieri, Sergio Rodriguez-Torres, Ashley J. Ross, Graziano Rossi, Ariel G. Sánchez, Arman Shafieloo, Jeremy L. Tinker, Rita Tojeiro, Jose A. Vazquez, and Hanyu Zhang (2017). "Dynamical dark energy in light of the latest observations". In: *Nature Astronomy* 1, pp. 627–632. DOI: 10.1038/s41550-017-0216-z. arXiv: 1701.08165 [astro-ph.CO].

Chapter 5

Discussion and Conclusion

In the last two decades, advances in instruments and computations allow cosmologists to place increasingly precise measurements on cosmological parameters. Small differences between results from different data sets become more and more pronounced. The most notable discrepancy in cosmology is the 'Hubble tension', the disagreement between the Hubble constant from late universe measurements using distance ladder or strong lensing time delays and early universe CMB or BAO based measurements.

It is important to investigate the source of inconsistency between measurements. It may be an artifact of systematic errors, or it may signal a failure in the Standard Model of Cosmology. But before looking for sources, we need to first assess whether the differences we see are statistically significant, which is what my research has focused on.

This thesis summarized my work on applying statistical tools to analyze and quantify consistency between different data sets as well as extensions to the ΛCDM model. In Chapter 2, we have found tensions between cosmological parameters obtained from the *Planck* 2015 high-multipole TT spectrum

($\ell \geq 1000$, roughly the scales inaccessible to *WMAP*) and its low-multiple counterpart, as well as other cosmological measurements, including *Planck* 2015 $\phi\phi$ lensing power spectrum and the local distance ladder measurement. In Chapter 3, we took a closer look at the *Planck* 2015 TT spectrum by comparing it to *WMAP*'s over their overlapping multipole range where power spectrum based likelihoods were used. We quantified the significance of their difference while accounting for the cosmic variance common to both experiments. We found that the spectra are consistent within 1σ. The consistency shown in our analysis provides high confidence in both the *WMAP*9 TT power spectrum and the overlapping multipole region of the *Planck* 2015 power spectrum, virtually independent of any assumed cosmological model. The *Planck* 2018 TT spectrum is only minimally different from the 2015 version (Planck Collaboration et al., 2018), and we therefore expect the $\ell \lessapprox 1000$ portion to remain consistent with *WMAP*. As for the *Planck* high multipole TT spectrum, Planck Collaboration, 2017 found that when accounting for the multi-dimensional parameter space including correlations between parameters, the discrepancy within *Planck* are at the 10 % level and hence not especially unusual. In addition, the recent release of DR4 maps and cosmological parameter constraints from the Atacama Cosmology Telescope collaboration are in excellent agreement with the results from Planck (Naess et al., 2020; Aiola et al., 2020), suggesting the *Planck* results are unlikely to be affected by systematic errors.

Since 2014 when the Hubble tension first became apparent (Planck Collaboration, 2014), cosmologists have exerted great effort to improve precision and accuracy in the measurement of the Hubble constant and have been ruling

out systematic errors in both the late and the early universe observations. Yet with lower uncertainties on both ends, the discrepancy has not shrunk and its significance has only grown. See Riess, 2019; Efstathiou, 2020 for summary and discussion of recent developments on the subject. It becomes more and more clear that the Hubble tension is an indication of new physics beyond the standard ΛCDM model. In this regard, my work in Chapter 4 was to aid hypothesis testing for alternative theories. I developed a procedure to quantify correlations between additional parameters in ΛCDM extensions that are not fitted simultaneously, which can and should be applied to more extensive lists of extension parameters, with existing and future cosmological data, in the search for an alternative model as a resolution to the Hubble tension.

References

Aiola, Simone et al. (2020). "The Atacama Cosmology Telescope: DR4 Maps and Cosmological Parameters". In: *arXiv e-prints*, arXiv:2007.07288, arXiv:2007.07288. arXiv: 2007.07288 [astro-ph.CO].

Efstathiou, G. (2020). "A Lockdown Perspective on the Hubble Tension (with comments from the SH0ES team)". In: *arXiv e-prints*, arXiv:2007.10716, arXiv:2007.10716. arXiv: 2007.10716 [astro-ph.CO].

Naess, Sigurd, Simone Aiola, Jason E. Austermann, Nick Battaglia, James A. Beall, Daniel T. Becker, Richard J. Bond, Erminia Calabrese, Steve K. Choi, Nicholas F. Cothard, Kevin T. Crowley, Omar Darwish, Rahul Datta, Edward V. Denison, Mark Devlin, Cody J. Duell, Shannon M. Duff, Adriaan J. Duivenvoorden, Jo Dunkley, Roland o Dünner, Anna E. Fox, Patricio A. Gallardo, Mark Halpern, Dongwon Han, Matthew Hasselfield, J. Colin Hill, Gene C. Hilton, Matt Hilton, Adam D. Hincks, Renée Hložek, Shuay-Pwu Patty Ho, Johannes Hubmayr, Kevin Huffenberger, John P. Hughes, Arthur B. Kosowsky, Thibaut Louis, Mathew S. Madhavacheril, Jeff McMahon, Kavilan Moodley, Federico Nati, John P. Nibarger, Michael D. Niemack, Lyman Page, Bruce Partridge, Maria Salatino, Emmanuel Schaan, Alessandro Schillaci, Benjamin Schmitt, Blake D. Sherwin, Neelima Sehgal, Cristóbal Sifón, David Spergel, Suzanne Staggs, Jason Stevens, Emilie Storer, Joel N. Ullom, Leila R. Vale, Alexander Van Engelen, Jeff Van Lanen, Eve M. Vavagiakis, Edward J. Wollack, and Zhilei Xu (2020). "The Atacama Cosmology Telescope: arcminute-resolution maps of 18,000 square degrees of the microwave sky from ACT 2008-2018 data combined with Planck". In: *arXiv e-prints*, arXiv:2007.07290, arXiv:2007.07290. arXiv: 2007.07290 [astro-ph.IM].

Planck Collaboration (2014). "Planck 2013 results. XVI. Cosmological parameters". In: *AAP* 571, A16, A16. DOI: 10.1051/0004-6361/201321591. arXiv: 1303.5076 [astro-ph.CO].

Planck Collaboration (2017). “Planck intermediate results. LI. Features in the cosmic microwave background temperature power spectrum and shifts in cosmological parameters”. In: *AAP* 607, A95, A95. DOI: 10.1051/0004-6361/201629504. arXiv: 1608.02487 [astro-ph.CO].

Planck Collaboration et al. (2018). “Planck 2018 results. VI. Cosmological parameters”. In: *arXiv e-prints*, arXiv:1807.06209, arXiv:1807.06209. arXiv: 1807.06209 [astro-ph.CO].

Riess, Adam G. (2019). “The expansion of the Universe is faster than expected”. In: *Nature Reviews Physics* 2.1, pp. 10–12. DOI: 10.1038/s42254-019-0137-0. arXiv: 2001.03624 [astro-ph.CO].

Vita

Yajing Huang received her Sc. B. degree in physics from Shandong University in China and enrolled in the Physics Ph.D. program at Johns Hopkins University in 2014. She conducted her research under the supervision of Prof. Bennett and focused her research on cosmology.